

## ABSTRACT

Zhang, Yun. Oxide and Metallic Precursor Powders for Superconducting  $\text{Bi}_2\text{Sr}_2\text{CaCu}_2\text{O}_x/\text{Ag}$  Round Wires. (Under the direction of Prof. Justin Schwartz).

Many future magnet applications for high energy physics and nuclear magnetic resonance require a superconducting conductor capable of generating magnetic fields above 30 T. Low temperature superconductors, such as NbTi and  $\text{Nb}_3\text{Sn}$ , can only generate magnetic fields up to 10.5 T and 20 T. High temperature superconductor  $\text{Bi}_2\text{Sr}_2\text{CaCu}_2\text{O}_x$  (Bi2212), with upper critical field greater than 100 T, is a promising candidate. As the only high field superconductor available as an isotropic round wire, Bi2212 Ag/Ag-alloy sheathed wires are of particular interest. Wire transport properties depends not only on wire heat treatment conditions, but also largely on precursor powder properties. Thus, a thorough study on precursor powder synthesis and the understanding of the key process-microstructure-properties relationships between precursor powder and wire performance is essential for further improvements in conductor performance.

In this research, a new method combining NanoSpray Combustion<sup>TM</sup> processing and solid-state calcination is developed to synthesize Bi2212 oxide precursor. Precursor powders with precisely controlled stoichiometry and chemical homogeneity containing over 99 vol% of Bi2212 single crystals are synthesized. Alkaline-earth cuprate (AEC) are found to be the only impurity phase in the precursor powders. Phase transformation, carbon release and grain growth during calcination are studied extensively through a series of quench studies. Effects of particle size, surface area, stoichiometry, chemical homogeneity and microstructures of the starting materials on Bi2212 formation and wire transport properties are discussed. With improved precursor powder properties, critical current density  $J_c$  is enhanced to 2520 A/mm<sup>2</sup> (4.2 K, 5 T).

The oxide-powder-in-tube (OPIT) route, however, has important shortcomings that limit the final Bi2212 wire performance, such as low tap-density, bubbling and poor electromechanical properties. In this research, an alternative method using metallic precursor with the potential to address these issues is developed and studied. A homogeneous metallic precursor with controlled stoichiometry containing Bi, Sr, Ca, Cu, Ag, and its alloys is produced by mechanical alloying. Both bulk samples and Ag-sheathed multifilamentary metallic wires are fabricated to study the correlations between metallic precursor synthesis, heat treatment conditions, phase transformations, microstructure development and the final wire transport properties.

Three pathways of metallic precursor oxidation and the cause of Bi flow are identified in Ag-sheathed wires. A thorough study on oxidation mechanism, phase transformation and microstructural development during heat treatment is performed. Advantages of metallic-powder-in-tube (MPIT) method include the formation of highly dense filaments containing micrometer Bi2212 grains before partial-melt processing (PMP) and the uni-axially textured Bi2212 grains within one filament after PMP. It is found that the formation of highly dense filament containing Bi2212 fine grains and Ag particles before PMP helps formation of large, c-axis textured Bi2212 filament during PMP. Furthermore, current-limiting factors including filament discontinuity, cation depletion and oxygen deficiency during oxidation stage are discussed. These results indicate that MPIT route has the potential to address the low tap-density and bubbling issues that are intrinsic with OPIT route. Further improvements in Bi2212/Ag multifilament wires requires improved wire architecture, enhanced oxidation kinetics and increased filament density before PMP.

© Copyright 2015 Yun Zhang

All Rights Reserved

Oxide and Metallic Precursor Powders for  $\text{Bi}_2\text{Sr}_2\text{CaCu}_2\text{O}_x/\text{Ag}$  Round Wires

by  
Yun Zhang

A dissertation submitted to the Graduate Faculty of  
North Carolina State University  
In partial fulfillment of the  
Requirements for the degree of  
Doctor of Philosophy

Materials Science and Engineering

Raleigh, North Carolina

2015

APPROVED BY:

---

Prof. Justin Schwartz  
Committee Chair

---

Prof. Carl Koch

---

Prof. Frank Hunte

---

Prof. Ron Scattergood

## **DEDICATION**

This thesis is dedicated to

my father Guobin Zhang and my mom Rong Li,

for their endless support and encouragement.

## **BIOGRAPHY**

Yun Zhang was born in Shanghai, China on February 3<sup>rd</sup>, 1988. After finishing her high school in No.2 High School of East China Normal University, she was admitted to the Department of Materials Science and Engineering at Shanghai Jiao Tong University in 2006. After undergraduate study, she was admitted to Ph.D. program in Department of Materials Science and Engineering at North Carolina State University in August 2010. She joined Dr. Justin Schwartz's group in 2011 and took her Ph.D. in Materials Science and Engineering in July 2015.

## **ACKNOWLEDGEMENTS**

I would like to express my sincere gratitude to my advisor Professor Justin Schwartz for his guidance, encouragement, and support throughout the course of my research. I would like to acknowledge the valuable feedback provided by my research advisory committee members: Professor Koch, Professor Hunte and Professor Scattergood. I would also like to thank every single member of Schwartz group who gave me numerous help during my study.

## TABLE OF CONTENTS

LIST OF TABLES.....	vi
LIST OF FIGURES.....	vii
Chapter 1: INTRODUCTION AND OVERVIEW.....	1
REFERENCES.....	34
Chapter 2: $\text{Bi}_2\text{Sr}_2\text{CaCu}_2\text{O}_x$ OXIDE PRECURSOR SYNTHESIS FROM NANO- OXIDES AND ITS EFFECTS ON MULTIFILAMENTARY WIRE TRANSPORT PROPERTIES.....	46
REFERENCES.....	80
Chapter 3: SYNTHESIS OF $\text{Bi}_2\text{Sr}_2\text{CaCu}_2\text{O}_x$ SUPERCONDUCTORS VIA DIRECT OXIDATION OF METALLIC PRECURSORS.....	86
REFERENCES.....	116
Chapter 4: STUDIES ON MULTIFILAMENTARY $\text{Bi}_2\text{Sr}_2\text{CaCu}_2\text{O}_x/\text{Ag}$ WIRE VIA METALLIC-POWDER-IN-TUBE ROUTE.....	121
REFERENCES.....	156
Chapter 5: CONCLUSIONS AND SUGGESTED FUTURE WORK.....	162

## LIST OF TABLES

Table 2-1 Characteristics of as-made powders.....	55
Table 2-2 Characteristics of precursor powders.....	65
Table 3-1 Chemical analysis of metallic precursors after milling.....	92
Table 3-2 Detailed heat treatment parameters for each sample.....	94
Table 3-3 Intensity ratio $\gamma$ and fraction $f$ of Bi2201 intergrowth in Bi2212 grains.....	108
Table 4-1 $J_c$ (4.2 K, self-field) of MPIT round wires and rolled tapes after PMP.....	145

## LIST OF FIGURES

Figure 1-1 (a) Change of electrical resistivity with temperature for a superconductor and normal material. (b) Diagram of the Meissner effect. Magnetic field lines, represented as arrows, are expelled from a superconductor below  $T_c$  [6].....2

Figure 1-2 Phase diagrams of (a) type I and (b) type II superconductors [6].....4

Figure 1-3 Crystal structure of  $\text{Bi}_2\text{Sr}_2\text{CuO}_6$  (Bi2201),  $\text{Bi}_2\text{Sr}_2\text{CaCu}_2\text{O}_8$  (Bi2212) and  $\text{Bi}_2\text{Sr}_2\text{Ca}_2\text{Cu}_3$  (Bi2223) [12].....6

Figure 1-4 Engineering critical current density ( $J_e$ ) of available superconductors used for magnets [15].....9

Figure 1-5 Schematic diagram of powder-in-tube (PIT) method to fabricate Bi2212/Ag wires and tapes [19].....10

Figure 1-6 Schematic diagram of “sausaging” phenomenon that occurs during wire drawing.....11

Figure 1-7 Schematic diagram of a typical partial-melt processing (PMP) profile.....12

Figure 1-8 (a) cross-section and (b) longitudinal images of a multifilamentary OPIT wire before PMP.....13

Figure 1-9 (a) cross-section and (b) longitudinal images of a multifilamentary OPIT wire after PMP. A: AEC, B: pores, C: interfilamentary bridging.....14

Figure 1-10 quaternary phase diagram of the  $\text{Bi}_2\text{O}_3$ -SrO-CaO-CuO system [106].....22

Figure 1-11 Schematic diagram of mechanical alloying of a single ball-powder-ball collision [124].....23

Figure 1-12 Schematic diagram of a two-step heat treatment profile to convert metallic precursor pellets into Bi2212 phase.....25

Figure 1-13 (a) cross-sectional and (b) longitudinal images of a multifilamentary MPIT round wire before heat treatment.....	27
Figure 1-14 Cross-sectional image of a multifilamentary MPIT rolled tapes before heat treatment.....	28
Figure 2-1 Optical microscope images of green wire cross-sections (a) Batch II and (b) Batch III.....	51
Figure 2-2 Heat treatment profiles for (a) internal oxidation and (b) PMP.....	52
Figure 2-3 Bright field TEM image of Batch II as-made powder.....	56
Figure 2-4 XRD pattern of Batch II as-made powder.....	57
Figure 2-5 (a) HAADF-STEM image of Batch II as-made powder (b) and (c) show corresponding EDS maps of the selected area.....	58
Figure 2-6 XRD patterns of Batch II powders quenched from 860 °C.....	61
Figure 2-7 SEM images of quenched Batch II powders after (a) 10 min (b) 1 hr (c) 12 hr and (d) 72 hr calcination at 860 °C.....	63
Figure 2-8 (a) Magnetization and (b) normalized magnetization versus temperature for quenched Batch II powders.....	64
Figure 2-9 CO <sub>2</sub> release versus time and temperature during the calcination of Batch II precursor powder.....	65
Figure 2-10 XRD results for the three precursor powders with the major peaks indexed.....	67
Figure 2-11 SEM images of Batch II precursor powder showing (a) soft agglomerates of Bi <sub>2</sub> 212 grains and (b) morphology of individual Bi <sub>2</sub> 212 grains.....	67
Figure 2-12 SEM image of Batch III precursor powder pellet with AEC particles indicated by circles.....	68

Figure 2-13 (a) TEM image of Batch II precursor powder and (b) a [001]-zone axis diffraction pattern.....69

Figure 2-14 (a) Magnetization and (b) normalized magnetization versus temperature for precursor powders.....70

Figure 2-15 DTA curves of the green wires in pure, flowing oxygen after dispersion strengthening heat treatment.....71

Figure 2-16 Transport  $J_c$  (4.2 K, 5 T) vs PMP peak temperature.....72

Figure 3-1 Schematic drawing of the two-step heat treatment temperature-time profile.....93

Figure 3-2 SEM micrograph and EDS maps of batch I after milling but before heat treatment.....96

Figure 3-3 XRD results for Batch I and II after milling but before heat treatment.....97

Figure 3-4 Magnetization versus temperature of heat treated samples and a reference Nexans granule sample. Samples from (a) batch I and the Nexans granule sample, (b) batch II to compare the effects of  $T_p$  and  $t_p$ , and (c) batch II to compare the effect of  $R_1$ . Note that (a) has a much smaller range of moment than (b) and (c).....98

Figure 3-5 Normalized magnetization versus temperature. Samples from (a) batch I and the Nexans granule sample, (b) batch II to compare the effects of  $T_p$  and  $t_p$ , and (c) batch II to compare the effect of  $R_1$ .....99

Figure 3-6 XRD results of heat treated samples I-3, II-1 and II-4.....100

Figure 3-7 XRD results, focusing on the Bi2201 006 and Bi2212 008 peaks, to compare (a) the effects of  $T_p$  and  $t_p$ , (b) the effect of  $R_1$ .....101

Figure 3-8 DTA curves showing melting peaks to compare (a) effects of  $T_p$  and  $t_p$ ; (b) effect of  $R_1$ .....102

Figure 3-9 SEM images of the top surfaces of heat treated samples. (a) II-1 (b) II-2 (c) II-3 (d) II-4.....103

Figure 3-10 Cross-sectional SEM images of polished samples (a) II-3 and (b) II-4.....104

Figure 3-11 SEM images of the pellet/Ag interface of samples (a) II-1 and (b) II-2.....104

Figure 3-12 (a), (b) STEM images of Bi2212 grains from sample II-4 with Bi2201 intergrowths and (c) EDS maps showing the Bi2201 halfcell intergrowths.....106

Figure 4- 1 Images of green multifilamentary wire before heat treatment (a) round wire cross-sectional image, (b) round wire longitudinal image and (c) rolled tape cross-sectional image .....126

Figure 4-2 Heat treatment profile for (a) stage 1: oxidation (b) stage 1 + 2: oxidation + conversion (c) complete heat treatment: oxidation, conversion & partial-melt processing.....130

Figure 4-3 Schematic drawing of critical current measurements setup on 50 mm-long wires.....134

Figure 4-4 SEM image and EDS maps showing the MP elemental distribution after deformation and before heat treatment.....135

Figure 4-5 SEM images of round wire surface after oxidation. Note that a crack along the wire axis was found on the surface, along with a layer of Bi.....136

Figure 4-6 SEM images of a 20 mm long longitudinally polished wire after oxidation.....137

Figure 4-7 SEM images and corresponding EDS maps of the Bi distribution (a,b) 1 mm from the left end, (c,d) 5 mm from the end and (e,f) 9 mm from the left end, after 500 °C – 5 hr oxidation.....138

Figure 4-8 SEM images of the outer Ag surface at wire sections (a) 1 mm from the left end (b) 9 mm from the left end, below crack 1.....	139
Figure 4-9 SEM images and corresponding EDS maps showing Bi concentration in Ag grain boundaries.....	140
Figure 4-10 SEM images of longitudinally polished rolled tapes after oxidation: (a) 5 mm from the left end and (b) 12 mm from the left end.....	141
Figure 4-11 SEM images of a longitudinally polished round wire after oxidation and conversion heat treatment (a,b) near the left end, (c,d) in the middle section.....	142
Figure 4-12 SEM images of a longitudinally polished round wire after PMP (a) near the wire end and (b) in the middle section of the wire.....	143
Figure 4-13 SEM images of filament microstructures near the end of the round wire after PMP.....	144

## Chapter 1

### INTRODUCTION AND OVERVIEW

#### **Superconductivity: basic principles**

In 1911, Kamerlingh Onnes observed a sudden loss of electrical resistance to the flow of DC current in mercury near 4 K, which marked the discovery of superconductivity [1]. Two properties are fundamental to superconductors, zero-resistivity and perfect diamagnetism [2] which are qualitatively illustrated in Figure 1-1. Below a critical temperature  $T_c$ , current can flow within the material without noticeable energy dissipation. A very important parameter of a superconductor is the critical current density  $J_c$ , which determines the maximum electric current that can flow in the material without energy dissipation. Another characteristic of a superconductor is the perfect diamagnetism below  $T_c$  and critical magnetic field  $H_c$ , or Meissner effect [3]. The Meissner state is a thermodynamic state of a superconductor where spontaneous currents arise in the surface, expelling the external magnetic field, which maintains zero magnetic field induction inside the material. A close examination pointed out that when a superconductor is exposed in a magnetic field, the field tends to zero within the superconductor with a penetration depth of  $\lambda_L$ . This length describes the distance required for magnetic fields to decay in going from a region of normal material into the perfectly diamagnetic superconductor.

In the superconducting phase, the conduction electron fluid is in a more strongly ordered state than it is in the normal state, and the diamagnetism in the Meissner state is an equilibrium property of this ordered state. The nature of this ordering process became clear when BCS theory was developed by Bardeen, Cooper and Schrieffer [4, 5]. BCS theory indicated that an attractive interaction between electrons, due to local distortion of lattice

(phonon exchange), results in the formation of electron pairs-Cooper pairs. Cooper pairs undergo a form of Bose condensation, which is associated with superfluidity. The formation of the electron-pair condensate gives rise to the rigidity of the superconducting wavefunction. As the temperature increases above absolute zero, excitations with an energy of  $(\Delta^2 + \epsilon_k^2)^{1/2}$  (where  $\epsilon_k$  is the energy of the corresponding excitation in the normal state) are produced that break the electron-pairs. In addition, the energy gap  $\Delta$  falls as temperature increases. Eventually, at  $T_c$ ,  $\Delta$  vanishes and the superconductor becomes a normal material. Only the condensed electrons with a number of  $n_s$  contribute to Meissner effects.

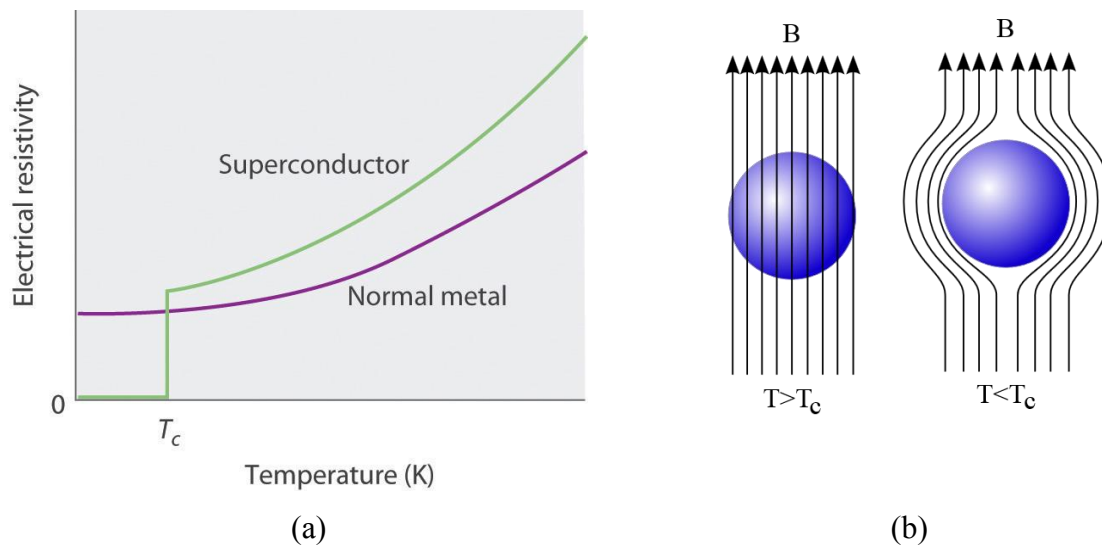


Figure 1-1 (a) Change of electrical resistivity with temperature for a superconductor and normal material. (b) Diagram of the Meissner effect. Magnetic field lines, represented as arrows, are expelled from a superconductor below  $T_c$  [6].

Ginsburg-Landau (GL) explained the superconductivity by using condensate wavefunction  $\Psi$ , which is a measure of the extent of superconducting ordering [7, 8].  $\Psi$  is a complex function

in a form of  $\Psi_0 \exp[iS(\mathbf{r})]$ , where  $\Psi_0$  is the unperturbed wavefunction and the phase  $S$  varies with the position. Its phase is the phase of the wavefunction of Cooper pairs and its amplitude is proportional to the local concentration of Cooper pairs. It was found that  $\Psi$  cannot change abruptly with position, but only gradually over a characteristic distance called GL coherence length  $\xi_{GL}$ .  $\lambda_L$  and  $\xi_{GL}$  are temperature dependent and are related by GL parameter  $\kappa$ , which is the ratio between  $\lambda_L$  and  $\xi_{GL}$ . On one hand, by solving GL equations in the case of  $\xi_{GL} \gg \lambda_L$  (with  $\kappa \ll 1$ ), it was found that as long as the relation  $\kappa < 1/\sqrt{2}$ , the surface energy at the interface separating superconductor and normal materials remain positive. These superconductors are called type I superconductors. On the other hand, GL equations predicted the existence of type II superconductors with  $\kappa > 1/\sqrt{2}$ , which was later introduced and investigated by Alexei Abrikosov [9, 10]. With  $\kappa > 1/\sqrt{2}$ , the surface energy at the interface separating superconductor and normal materials becomes negative, which energetically favors the formation of normal material-superconductor interface. Total displacement of external field from superconductor (as in type I superconductor) does not lead to a state with the minimum energy, but a configuration where superconductor is divided into alternating superconducting and normal regions. Thus in type II superconductors, the transition stage from Meissner state to normal state is broadened, where superconducting and normal phase can coexist and the magnetic field can partially penetrate the superconductor. This transition stage is called mixed state and the lower and upper critical field limits are called  $H_{c1}$  and  $H_{c2}$ . Phase diagrams of type I and type II superconductors are illustrated in Figure 1-2 [6]. Type I superconductor switches abruptly from Meissner state to the normal state of full penetration of magnetic flux as in Figure 1-2(a). This behavior is normally observed in elemental superconducting materials, such as Hg, Al and Sn. Type II

superconductor switches from the Meissner state to a mixed state of partial penetration of magnetic flux at a lower critical field  $H_{c1}$ , then crosses over continuously to full flux penetration at a upper critical field  $H_{c2}$  as in Figure 1-2(b). Typical examples of type II superconductors are  $Nb_3Sn$ ,  $NbTi$  and all high temperature superconductors.

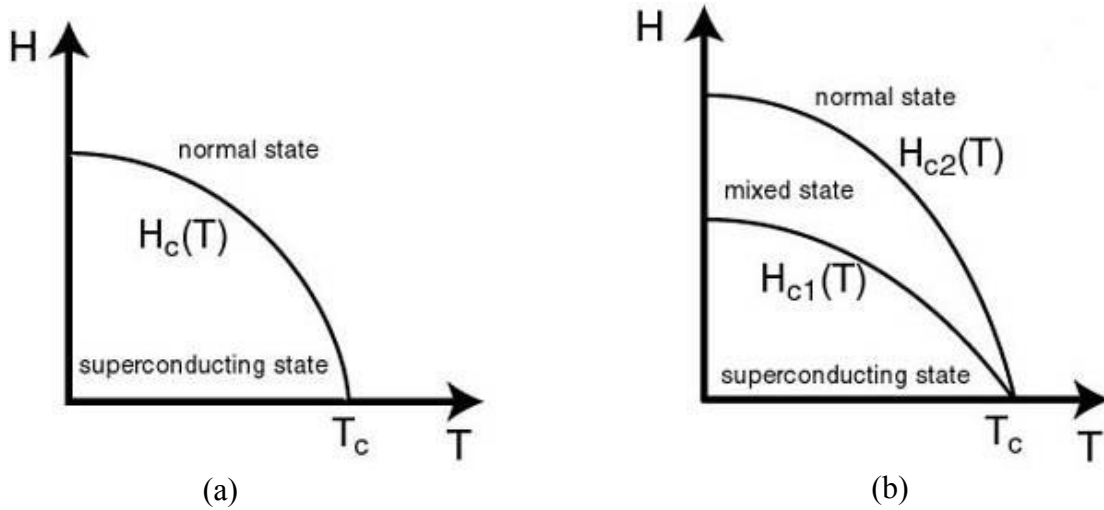


Figure 1-2 Phase diagrams of (a) type I and (b) type II superconductors [6].

For type II superconductor, the penetration depth  $\lambda_L$  is larger than coherence length  $\xi_{GL}$ . In a mixed state with external magnetic field, the magnetic domains within the superconductor are reduced to individual magnetic flux quanta  $\Phi_0 = h/2e = 2 \times 10^{-15} \text{ Tm}^2$ . Vortices are invaded and superconductivity is lost in the  $\xi_{GL}$  radius area and the magnetic field energy is reduced in the  $\lambda$  radius of a flux line. Flux line lattices are formed in the bulk and the mixed state. Qualitatively speaking, the cores of flux lines represent tubes of normal phase with radius  $\xi_{GL}$  imbedded in the superconducting phase. As the field exceeds  $H_{c1}$  and further increases, the density of flux lines increases until their cores with radius  $\sim \xi_{GL}$  start overlap, which results in suppression and loss of superconductivity at  $H_{c2}$ .

## High temperature superconductor

$\text{YBa}_2\text{Cu}_3\text{O}_{7-x}$  (YBCO) and Bi-Sr-Ca-Cu-oxide (BSCCO) are the two typical high temperature superconductors (HTS) with  $T_c$  above liquid nitrogen temperature, 77K. Both YBCO and BSCCO are cuprate superconductors, which have a perovskite like crystal structure. In cuprate superconductors,  $\text{CuO}_2$  planes represent the basic structural element and are separated by charge reservoirs layers containing large ions, such as Bi or Y. Charge reservoir layers retrieve electronic charge from the  $\text{CuO}_2$  planes and leave mobile holes in the planes, which is often called “chemical doping”. Thus, the holes generated by chemical doping in  $\text{CuO}_2$  planes give rise to superconductivity in the cuprates at low temperatures.

In particular, BSCCO superconductors were the first cuprate family that displays a  $T_c$  up to 110 K at ambient and ~135 K at ~35 GPa, which was discovered by Hirosh Maeda et al. in January 1988 [11]. Three members of BSCCO family share the common stoichiometry in the form of  $\text{Bi}_2\text{Sr}_2\text{Ca}_{n-1}\text{Cu}_n\text{O}_{2n+4}$ , where  $n=1, 2$  and  $3$ , respectively. Crystal structures of  $\text{Bi}_2\text{Sr}_2\text{CuO}_6$  (Bi2201),  $\text{Bi}_2\text{Sr}_2\text{CaCu}_2\text{O}_8$  (Bi2212) and  $\text{Bi}_2\text{Sr}_2\text{Ca}_2\text{Cu}_3\text{O}_{10}$  (Bi2223) are shown in Figure 1-3 [12]. The unit cell of Bi2201 phase is a stack of atomic planes in the sequence  $(\text{BiO})_2/\text{SrO}/\text{CuO}_2/\text{SrO}/(\text{BiO})_2/\text{SrO}/\text{CuO}_2/\text{SrO}/(\text{BiO})_2$ . The unit cell of Bi2212 phase is a stack of atomic planes in the sequence  $(\text{BiO})_2/\text{SrO}/\text{CuO}_2/\text{Ca}/\text{CuO}_2/\text{SrO}/(\text{BiO})_2/\text{SrO}/\text{CuO}_2/\text{Ca}/\text{CuO}_2/\text{SrO}$ . The unit cell of Bi2223 phase is a stack of atomic planes in the sequence of  $(\text{BiO})_2/\text{SrO}/\text{CuO}_2/\text{Ca}/\text{CuO}_2/\text{Ca}/\text{CuO}_2/\text{SrO}/(\text{BiO})_2/\text{SrO}/\text{CuO}_2/\text{Ca}/\text{CuO}_2/\text{SrO}$ . The  $T_c$  in BSCCO superconductor is not only a function of doped carrier density (holes) in every  $\text{CuO}_2$  plane but also depends on the number of  $\text{CuO}_2$  layers in a unit cell.  $T_c$  of Bi2201 is ~10 K. Addition of Ca to this Bi2201 resulted in a  $T_c$  between 80 K and 110K (Bi2212 and Bi2223 phases).

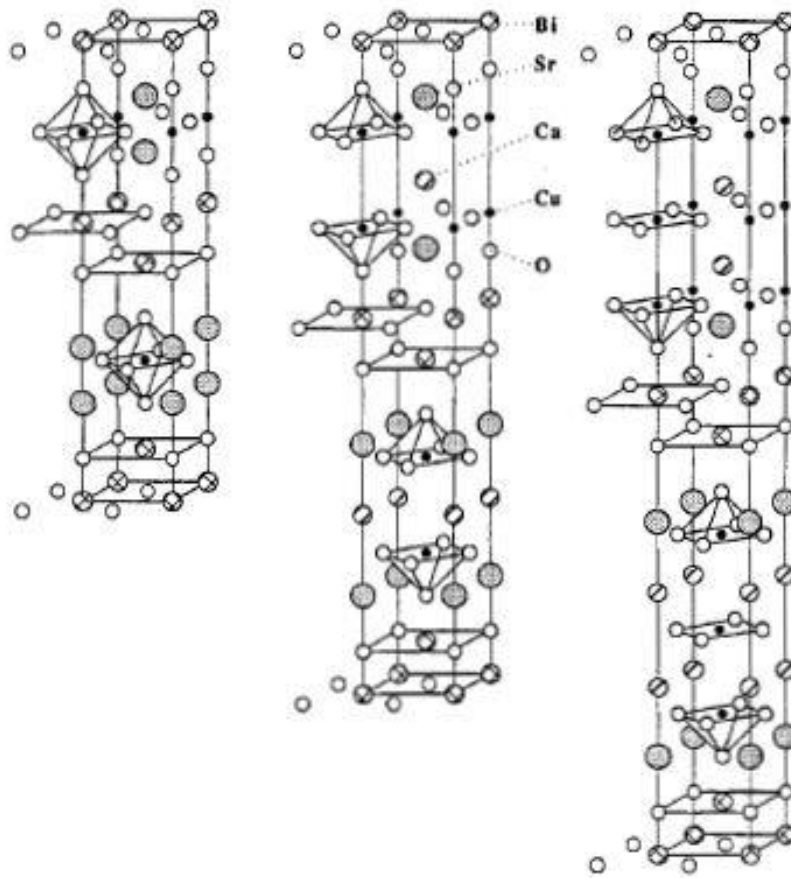


Figure 1-3 Crystal structure of Bi<sub>2</sub>Sr<sub>2</sub>CuO<sub>6</sub> (Bi2201), Bi<sub>2</sub>Sr<sub>2</sub>CaCu<sub>2</sub>O<sub>8</sub> (Bi2212) and Bi<sub>2</sub>Sr<sub>2</sub>Ca<sub>2</sub>Cu<sub>3</sub> (Bi2223) [12].

Large anisotropy in cuprate superconductors is caused by the layered crystalline perovskite structure. For example, in Bi2212, the basic block is CuO<sub>2</sub>/Ca/CuO<sub>2</sub>, which is separated by four oxide layers namely two SrO and two BiO planes. Due to two-dimensional structure of Bi2212, the coherence length depends on the crystallographic direction.  $\xi_c$  along c-axis is  $\sim 1$  Å while  $\xi_{ab}$  in a-b plane is  $\sim 15$  Å. Therefore, upper critical fields  $H_{c2}$  directed parallel and

perpendicular to the basic a-b plane are different. Based on GL equations,  $H_{c2\perp} = \frac{\Phi_0}{2\pi\xi_{ab}^2}$  and  $H_{c2\parallel} = \frac{\Phi_0}{2\pi\xi_{ab}\xi_c}$  and the anisotropy ratio is  $\frac{H_{c2\parallel}}{H_{c2\perp}} = \frac{\xi_{ab}}{\xi_c}$ . Superconductivity in Bi2212 is confined to the CuO<sub>2</sub> planes, which are separated by insulating layers and are coupled to each other by Josephson junctions. If magnetic field is oriented along the c-axis, the flux lines reduce to stacks of two-dimensional point vortices or pancake vortices. Compared to a continuous flux line, as it exists in the conventional superconductors, a stack of the pancake vortices in cuprate superconductors is energetically favorable and has additional degrees of freedom for thermal excitations [13]. If the magnetic field is oriented parallel to a-b plane, the vortex core preferably runs between CuO<sub>2</sub> layers. When the coupling between layers is weak, vortex lines along the a-b plane are referred to as Josephson vortices or strings.

### **Bi2212 round wires for high field magnets**

High-field magnets have been applied to research in medicine, biology, high energy physics, chemistry, etc. In general, magnetic fields are produced by the flow of electrical current (Oersted effect). Conventional electromagnets have water-cooled copper windings running at a current density of about  $10^3 \text{ Acm}^{-2}$ . Iron saturates at a field of about 2 T, thereby imposing an upper limit on field. The well-known Bitter solenoids can carry higher current densities and generate higher fields, but at the cost of enormous power consumption and the enormous need for cooling apparatus. Superconducting wires, however, allow enormous current densities to flow without electrical resistance. They are able to produce large volumes of high magnetic field for a small consumption of electrical power. In the late 1950s and early 1960s, researchers discovered type II superconducting alloys that were able to remain superconducting up to very high fields and were also able to carry extremely high current densities. Superconducting magnets were built since then.

Many future magnet applications for high energy physics and nuclear magnetic resonance require a superconducting conductor capable of generating magnetic fields above 30 T [14]. Figure 1-4 compares the engineering critical current densities ( $J_e$ ) as a function of applied magnetic field for several state-of-the-art long length high temperature superconductors and low temperature superconductors used for magnets at their standard operation temperatures [15]. Low temperature superconductors, such as NbTi and Nb<sub>3</sub>Sn, can only generate magnetic fields up to 10.5 T and 20 T [14] due to their upper critical fields less than 25 T at 4.2 K. Thus, high temperature superconductors, such as YBa<sub>2</sub>Cu<sub>3</sub>O<sub>7-x</sub> (YBCO) and Bi<sub>2</sub>Sr<sub>2</sub>CaCu<sub>2</sub>O<sub>x</sub> (Bi2212), with upper critical field greater than 100 T, are promising candidates [16-18]. As the only high field superconductor available as an isotropic round wire, Bi2212 Ag/Ag-alloy sheathed wires are of particular interest.

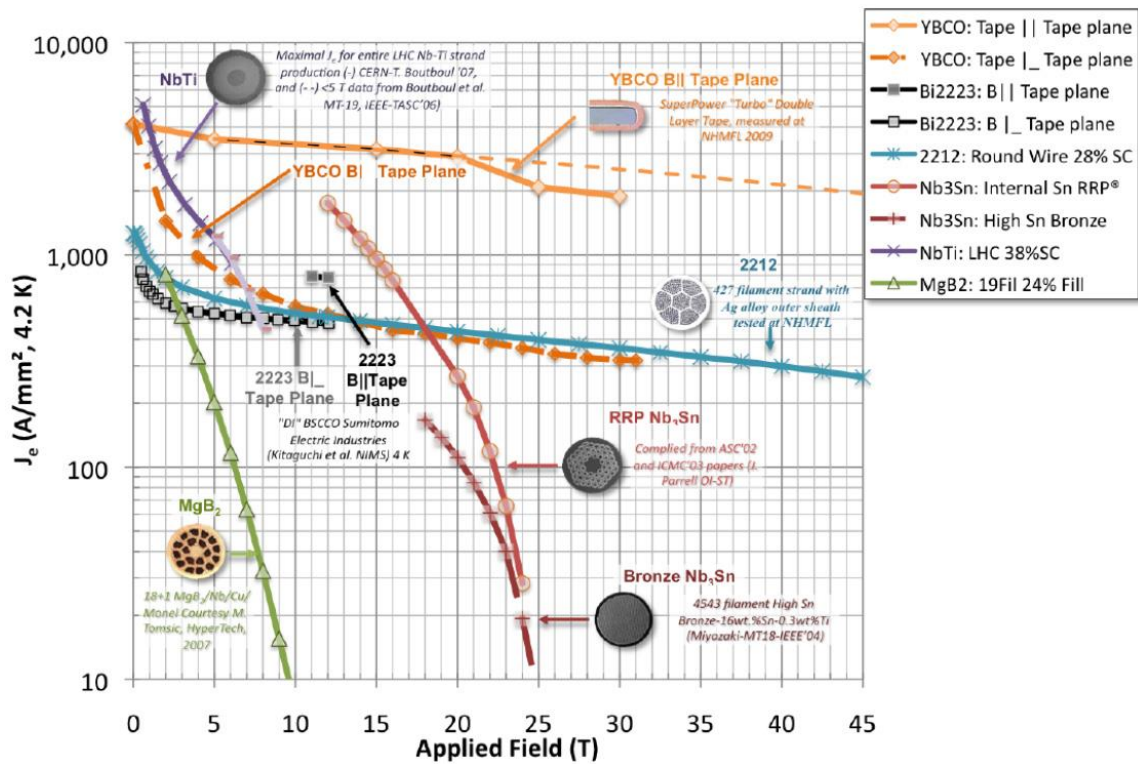


Figure 1-4 Engineering critical current density ( $J_e$ ) of available superconductors used for magnets [15].

### Bi2212/Ag wire fabrication

Powder-in-tube (PIT) method is the most common approach for manufacturing Bi2212/Ag multifilamentary wires and tapes, as illustrated in Figure 1-5 [19]. Typical PIT method includes synthesis of precursor powders, packing into Ag or Ag-alloy tubes, deforming into wire, restacking and partial-melt processing (PMP) [20]. Rolling is used to fabricate Ag-sheathed tapes after wire deformation.

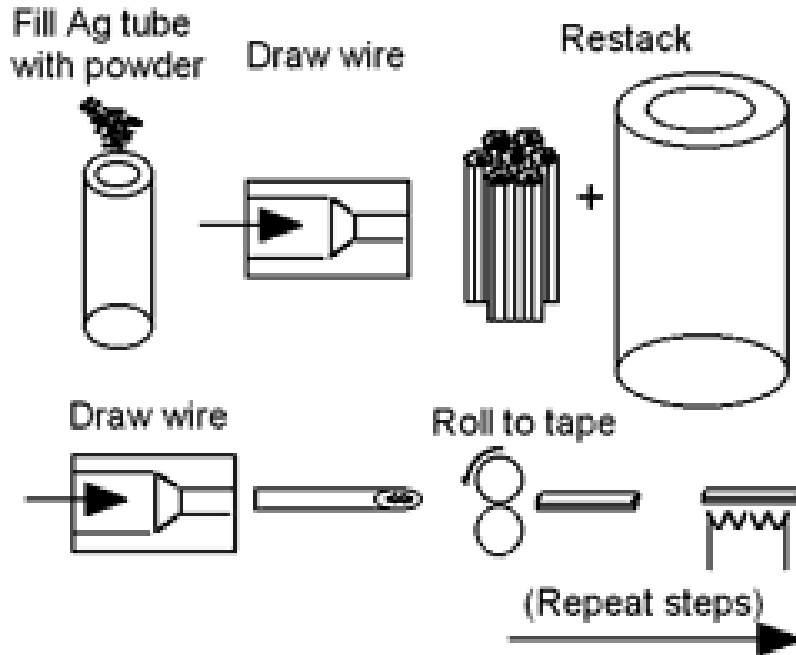


Figure 1-5 Schematic diagram of powder-in-tube (PIT) method to fabricate Bi<sub>2212</sub>/Ag wires and tapes [19].

The reason to use Ag as wire sheath is that Ag is a noble and ductile metal permeable to oxygen at elevated temperatures [21-23]. In addition, the melting point of Ag is higher than Bi<sub>2212</sub> partial-melt temperature, which enables Ag sheath to act as substrates for Bi<sub>2212</sub> grain alignment during wire heat treatment [24, 25].

The mechanical deformation of the Ag/precursor powder composite is an important step in fabricating Ag-sheathed BSCCO conductors. It greatly affects the filament shapes, 2212/Ag ratio, filament size distribution, the smoothness of the Ag/precursor powder interface, the macroscopic filament connectivity and the final microstructure and transport properties of the conductor [26-28]. One of the common phenomena in wire fabrication is the filament thickness variation along the wire length, so called “sausaging”, as illustrated in Figure 1-6

due to strain non-uniformity of precursor core and Ag sheath during wire drawing [28]. Sausaging will cause significant Bi2212 grain misorientation and the current “bottlenecks”, which lead to reduced  $J_c$  [29, 30]. The generation of the sausaging in the multifilamentary wires is very sensitive to the drawing conditions, additional efforts to address this issue include low-temperature annealing, small approach angle and small reduction per pass during wire drawing [26]. A recent study on Bi2212 multifilamentary wires by groove-rolling process shows that large critical current density improvement [31]. Instead of a drawing process, groove-rolling does not present the risk of filament sausaging and results in higher powder compaction in the green wire.

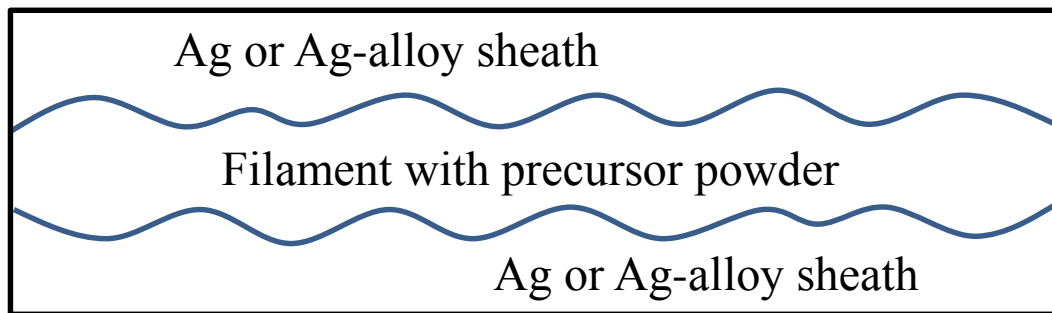


Figure 1-6 Schematic diagram of “sausaging” phenomenon that occurs during wire drawing.

### **Oxide-powder-in-tube method**

In oxide-powder-in-tube (OPIT) method, high purity Bi2212 powder is used to fill the Ag or Ag-alloy tube. Figure 1-7 shows a typical PMP profile. PMP starts with a pre-annealing step, then a heating segment to the maximum processing temperature ( $T_{peak}$ ), above the Bi2212 peritectic temperature, and a hold for a 0.1-1 hr ( $t_{peak}$ ).  $T_{peak}$  is usually in the range of 880 – 900 °C. During the partial-melt, Bi2212 powder melts incongruently, forming several non-

superconducting crystalline phases and a liquid phase, which cannot convert completely to Bi2212 during subsequent cooling. Non-superconducting impurities remain after solidification, including  $\text{Bi}_2\text{Sr}_2\text{CuO}_x$  (Bi2201), a copper-free (CF) phase and alkaline earth cuprates (AEC) [32-34]. Furthermore, bubbles and voids form and evolve during PMP because of the low tap density of the green wire and carbon residue in the Bi2212 oxide precursor [35, 36].

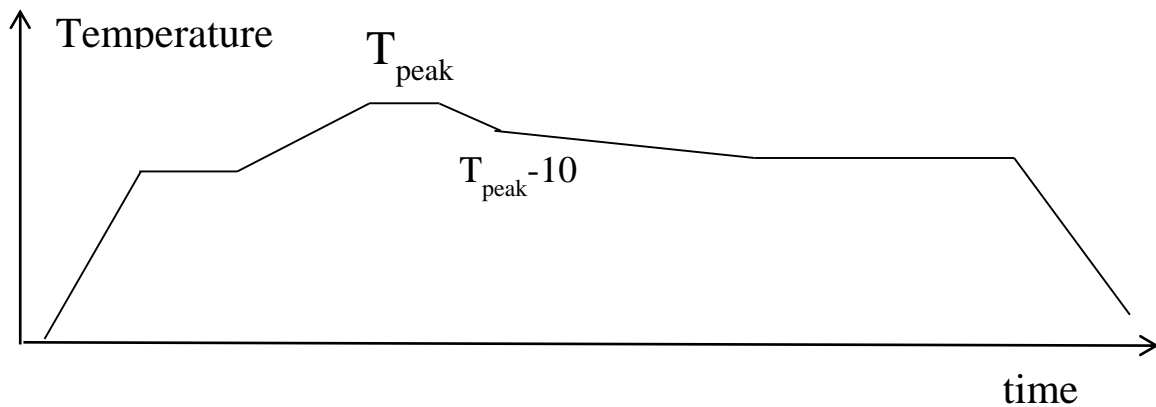
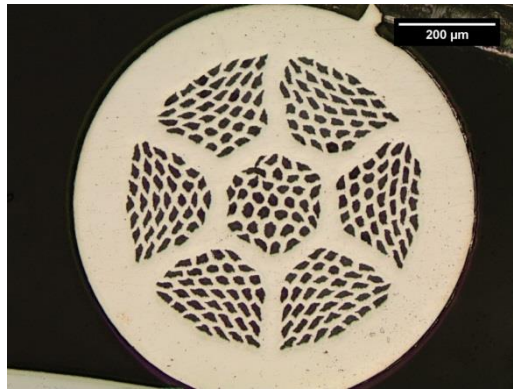
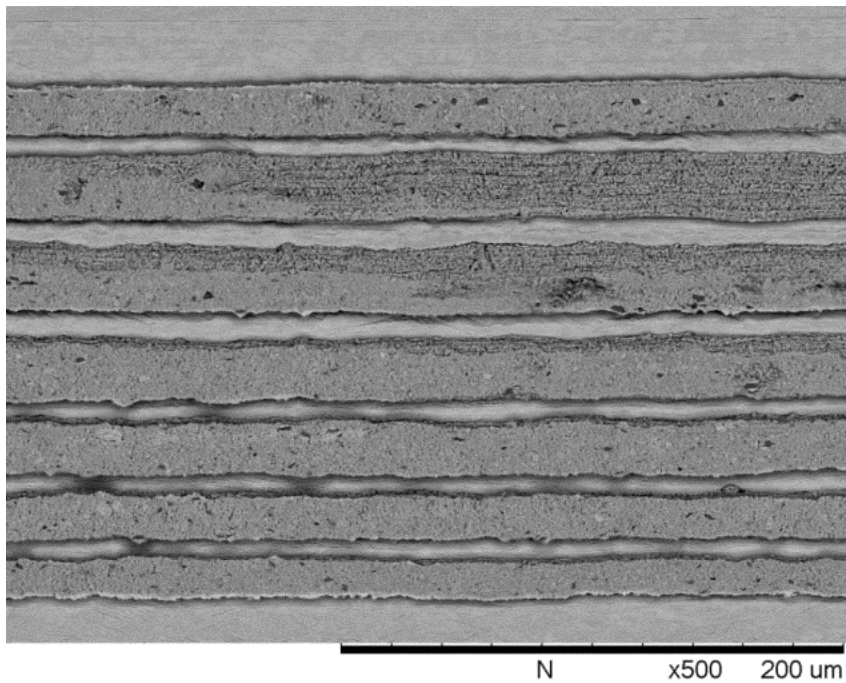


Figure 1-7 Schematic diagram of a typical partial-melt processing (PMP) profile.

Figure 1-8 shows the cross-section and longitudinal images of a multifilamentary OPIT wire before PMP, which is called “green wire”. It has a 0.81 mm outer diameter and consists of 259 filaments in a  $37 \times 7$  configuration with a fill factor of 15.0%. The filaments are in a pure Ag matrix contained within a Ag–0.1 wt% Al alloy outer sheath. The average filament size is 30  $\mu\text{m}$ . Figure 1-9 shows microstructure of the same wire but after PMP. In addition to dense and textured Bi2212 colonies, secondary phases, porosity and interfilamentary bridges are also observed.



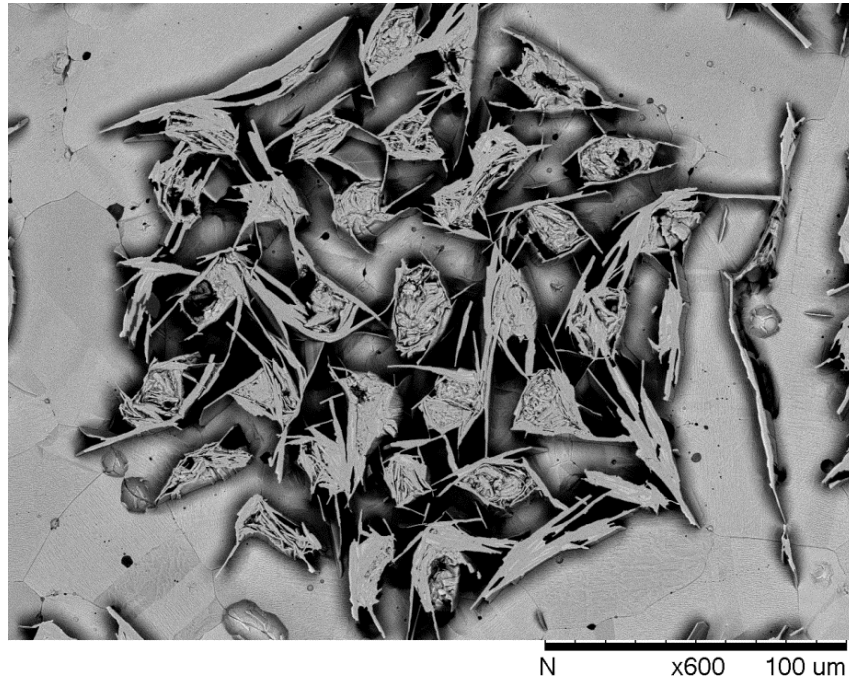
(a)



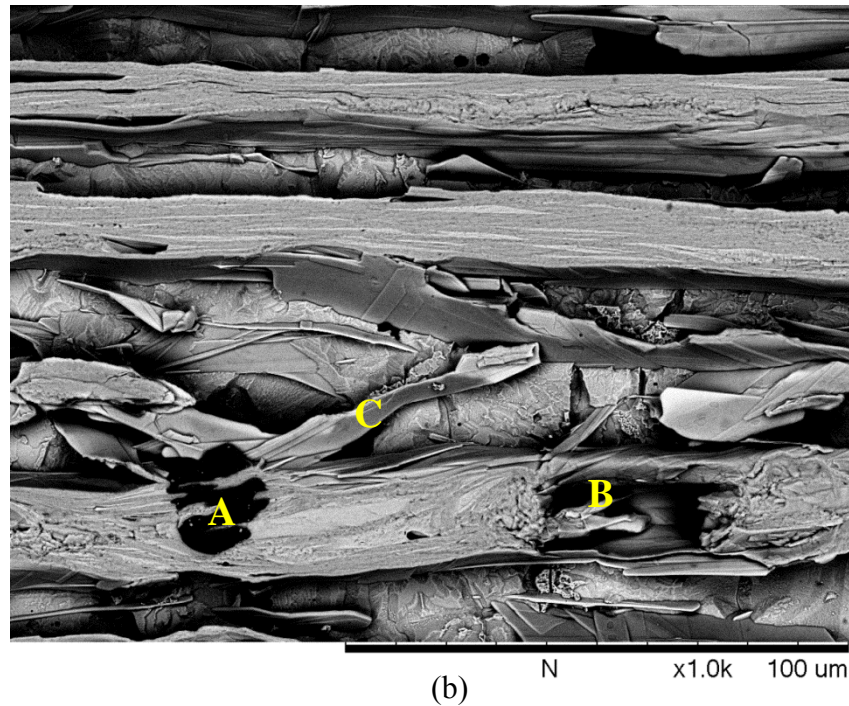
123

(b)

Figure 1-8 (a) cross-section and (b) longitudinal images of a multifilamentary OPIT wire before PMP



(a)



(b)

Figure 1-9 (a) cross-section and (b) longitudinal images of a multifilamentary OPIT wire after PMP. A: AEC, B: pores, C: interfilamentary bridging

There have been many studies focused on the optimization of PMP conditions on wires that vary the temperature, time and atmosphere to improve Bi2212 phase purity, grain connectivity and thus transport properties [37, 38]. These studies propose requirements on stoichiometry, phase purity, homogeneity and level of carbon content of Bi2212 precursors in the green wire. Yet, far fewer studies have discussed the effect of precursor stoichiometry on wire performance [27, 39-41], and most of those either focused solely on the synthesis process and properties of Bi2212 bulk materials [42, 43] or studied precursor properties by comparing superconducting tapes/thick films that had varying methods, geometries and substrates [44-50]. The main characteristics in the Bi2212 oxide precursor include cation stoichiometry, chemical homogeneity, impurity level, phase assemblage, carbon content and particle size. All of these factors are expected to affect the melting behavior and solidification during PMP, i.e. melting onset temperature, melting homogeneity, phase assemblage, nucleation and growth kinetics microstructures and the superconducting properties of the final conductor, i.e.  $T_c$  and  $J_c$ .

#### *Bi2212 powder synthesis*

The solid-state route starts with raw materials such as oxides, carbonates, nitrates or hydroxides and goes through a series of calcination and pulverizing processes [51-57]. High purity powders of SrO, CaO, Bi<sub>2</sub>O<sub>3</sub> and CuO are used in the preparation of Bi2212 phase. SrO and CaO are usually obtained by calcining SrCO<sub>3</sub> and CaCO<sub>3</sub> at 1200 °C. The final properties of Bi2212 powders, including phase assemblage, grain size and homogeneity, depend on the stoichiometry and particle size of the starting materials [58-61], calcination conditions [42, 62, 63] and the pulverizing process, such as grinding and ball milling. In previous studies, the common size of the starting material powders was in micrometers or

larger, resulting in chemical inhomogeneities and incompleteness of carbon release and thus required a repetition of calcination and pulverizing processes.

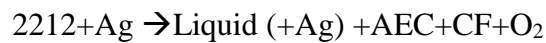
The liquid-phase route produces homogeneous and sub-micron size powders before calcination. Typical methods are spray pyrolysis [60], co-precipitation [44, 64] and sol-gel [65, 66], among which, the spray pyrolysis [67] is the most promising because it can control the stoichiometry precisely and produce homogeneous Bi2212 powders without pulverizing. Both co-precipitation and sol-gel require precise control of the solution pH value and solubility of the solvents to maintain the stoichiometry. Furthermore, a ball milling is usually involved which can affect stoichiometry.

A method combining NanoSpray Combustion<sup>TM</sup> processing and solid-state calcination is used to synthesize Bi2212 oxide precursor. Nanosize oxides produced by NanoSpray Combustion<sup>TM</sup> are used as a starting material to synthesize Bi2212 oxide precursors via solid-state calcination. During NanoSpray Combustion<sup>TM</sup> processing, the metal ions are homogeneously mixed at the atomic level. Vapor species containing gaseous atoms, ions and molecular-oxide species condense to form atomic clusters and then coalesce to form nanosize oxides [47, 60, 63, 68]. After one cycle of calcination in O<sub>2</sub>, high purity Bi2212 powder with precisely controlled stoichiometry, chemical homogeneity, uniform particle size and ultra-low carbon content can be synthesized.

#### Phase transformation during PMP

Generally, PMP is governed by two reactions:

Upon heating, Bi2212 precursor powders decompose into a liquid phase and non-superconducting crystalline phases including AEC and CF phases, along with a release of O<sub>2</sub>.



Upon cooling, Bi2212 grains form in the liquid and grows by a reverse peritectic reaction between the liquid, AEC and CF, along with absorption of O<sub>2</sub>.



Due to the phase segregation and kinetic limitations during solidification, however, the reverse peritectic reaction is incomplete, leaving remnant grains of AEC and CF phases in the fully-processed wire. Furthermore, Bi2201 grains and intergrowths growths also form beside and within Bi2212 grains [69-71].

Additionally, the incongruent melting temperature and phase assemblage in the melt strongly depend on O<sub>2</sub> partial pressure. For example, Bi2212 melting point is ~ 880 °C in 1 atm O<sub>2</sub>, but can be reduced by 20 – 30 °C in air [72-74].

#### Effects of stoichiometry and chemical homogeneity

Stoichiometry of precursor powder impacts the melting behavior, phase assemblage and thus transport J<sub>c</sub> of PMP wires [68]. Previous studies indicate the Bi2212 single phase region extends to a Bi-rich region and a slightly Ca-deficient composition results in high transport J<sub>c</sub> [43, 60, 75, 76]. Another important property of Bi2212 precursor is the chemical homogeneity within each batch for wire fabrication. For Bi2212 wire processing, a uniform melting behavior along the entire wire length is crucial to transport properties as phase assemblage and segregation are very sensitive to the PMP peak temperature [77]. Local stoichiometry variation may divert the solidification pathway after partial-melt, resulting in extensive formation of AEC, CF and/or Bi2201 grains.

#### Effects of impurities

Recent studies show that different impurity phases in Bi2212 wire play different roles on wire transport performance [78]. Two types of impurity phases are of particular interest,

Bi2201 and AEC phases. It was found that  $J_c$  is directly proportional to the percentage of “predominantly-Bi2212” filaments, and inversely proportional to the percentage of filaments “containing-large-Bi2201 grains”. And there is no or weak correlations between  $J_c$  and filaments containing CF, AEC or mixed secondary phases [41]. Based on these results, due to incomplete conversion from Bi2201 to Bi2212 during solidification in PMP, large Bi2201 grains remaining in heat treated wires have a significantly negative influence on transport  $J_c$  [27, 41, 79], which indicates that the absence of Bi2201 grains in the precursor powders is strongly preferred to lower the residue Bi2201 content after wire processing. Yet, AEC phases are not necessarily detrimental to wire transport. Large grains of AEC particles, i.e., larger than the wire filament size, can be detrimental to transport  $J_c$  as they act as big obstacles for current flow [41]. Small AEC grains, however, may act as nucleation sites for Bi2212 solidification during PMP [39]. Thus, the presence of AEC phases with particle sizes smaller than filament size is not considered to be a negative factor on transport  $J_c$ .

#### Effects of carbon content

Carbon residue in the powder can cause severe porosity in the wire filaments during PMP, significantly reducing transport  $J_c$  [43, 80, 81]. Excessive carbon is detrimental because carbon would react with  $O_2$  to form CO or  $CO_2$ , which cannot diffuse through Ag sheath and result in high internal gas pressures ( $P_{CO_2}$ ) within the wire at elevated temperatures during PMP [57, 82]. Furthermore, internal gas pressure in long-length wires drives creep of the Ag sheath during the heat treatment, causing wire to expand, lowering the density of Bi-2212 filaments, and therefore degrading the wire  $J_c$ ; the creep rupture of silver sheath naturally leads to the leakage of Bi-2212 liquid [82]. Therefore, it is crucial to minimize the carbon content during powder synthesis, especially in the calcination step. Generally, carbon content

should be minimized to be less than 250 ppm in wt% to eliminate bubbling in the tapes and wires [51, 83].

#### Effects of wire filament size

Previous studies show that the wire filament size has significant effects on wire transport behavior, particularly for the precursor powders with otherwise similar properties. Generally,  $J_c$  increases with decreasing filament size [27]. The reason is related to the increasing Ag/filament interfaces. Those interfaces provide more nucleation sites for Bi2212 solidification during PMP, resulting in a high degree of alignment as similarly observed in tapes. Furthermore, small filament size provides a geometric constraint on Bi2212 grain growth. Aksenova et al. suggested that preferential alignment of Bi2212 grains in the filament is a consequence of geometric constraint by Ag sheath and large growth anisotropy between a-b plane and c-plane [84]. When the filament size is below 12  $\mu\text{m}$ , however, the filament is unstable during PMP [85]. The reason is due to the presence of secondary phases and voids in the filament after PMP. With the sizes of non-superconducting secondary phases or voids being comparable to the filament size, the supercurrent is significantly blocked. Furthermore, Bi2212 crystals nucleate on arbitrary-shaped and randomly distributed secondary phase particles are aligned to the surface of the secondary particles instead of Ag/filament interface. Thus, with less Ag/filament interfaces than secondary phase surfaces in a small filament, Bi2212 grains are less aligned to the filament axis, which affects the current flow.

#### **Metallic-powder-in-tube method**

Although there are a number of different approaches to synthesizing oxide precursors [47, 50, 60, 86-91], the OPIT route has important shortcomings that limit the final Bi2212 wire

performance. One significant challenge is in low tap density. The tap densities typically range from 1 g/cm<sup>3</sup> to 2.5 g/cm<sup>3</sup>, whereas the density of Bi2212 is 6.45 g/cm<sup>3</sup>. Thus, starting from oxide precursors, it is not possible to obtain a 100% dense green wire. During PMP, bubbles and voids form and evolve, greatly reducing the transport critical current density ( $J_c$ ) of wire [35, 84, 86, 92-94]. Recently, over-pressure processing has shown to be effective in reducing gross microstructural porosity in Bi2212 wire, resulting in greatly increased  $J_c$  [95]. But, even with over-pressure processing, 100% theoretical density is not obtained in the filaments, and further densification is likely to result in even great improvements in wire  $J_c$  [96]. Another challenge facing Bi2212 for high field superconducting magnet is poor electromechanical performance. High field superconducting magnets experience very large Lorentz forces and thus strain tolerance is an important characteristic for high field conductors [97, 98]. There is evidence of an electrical “backbone” in Bi2212 round wires with significantly higher strain tolerance and reversible behavior, and improving the filament density by eliminating porosity and non-superconducting phases is expected to improve the strain tolerance by increasing the volume fraction of the strong backbone [99-101]. A recent study by Godeke et al. found that over-pressure processing does not increase the linear reversible strain (0.3% strain) relative to more porous, conventionally processed Bi2212 wires. In fact, the irreversible reduction in  $J_c$  for wires densified by over-pressure processing appears to be even larger than not-densified wires [102]. This may be a result of trapped gas within the filament during over-pressure processing.

An alternative to the oxide precursor route with the potential to address these issues is metallic precursors that are not oxidized until after wire deformation. Previously, metallic precursors were studied for Bi2223 metallic-precursor-in-tube (MPIT) tapes. Starting with

ductile metallic precursors, a relatively smooth interface between filament and Ag sheath and fine filaments as small as 5  $\mu\text{m}$  were achieved with metallic precursors for multifilamentary Bi2223 tapes [103-105]. After heat treatment, the Bi2223 tapes were flexible and ductile with high strain tolerance required for large-scale use [103].

There are key differences between Bi2212 and Bi2223 indicating that the metallic precursor route may be more suitable for Bi2212 than for Bi2223. One of the most fundamental differences between Bi2212 and Bi2223 is the stability of the superconducting phase. Bi2223 has a very small stable phase field, which may only exist when doped with Pb. Figure 1-10 shows the quaternary phase diagram of the  $\text{Bi}_2\text{O}_3$ -SrO-CaO-CuO system [106]. The stable phase field for Bi2212, however, is very large, covering a range of Bi, Sr, and Ca stoichiometries and a broad temperature space [39, 107, 108]. Thus, the direct conversion from metallic precursors to Bi2212 is likely to be straightforward and faster than the conversion to Bi2223. Rapid, direct conversion will also minimize the inter-diffusion of Bi2212 cations with the Ag sheath [73, 109-112]. Lastly, the Pilling-Bedworth ratio for Bi2212 and Bi2223 are 1.112 and 1.294, respectively, indicating that during the metal-to-ceramic conversion, the net expansion of Bi2212 is less than half of that of Bi2223.

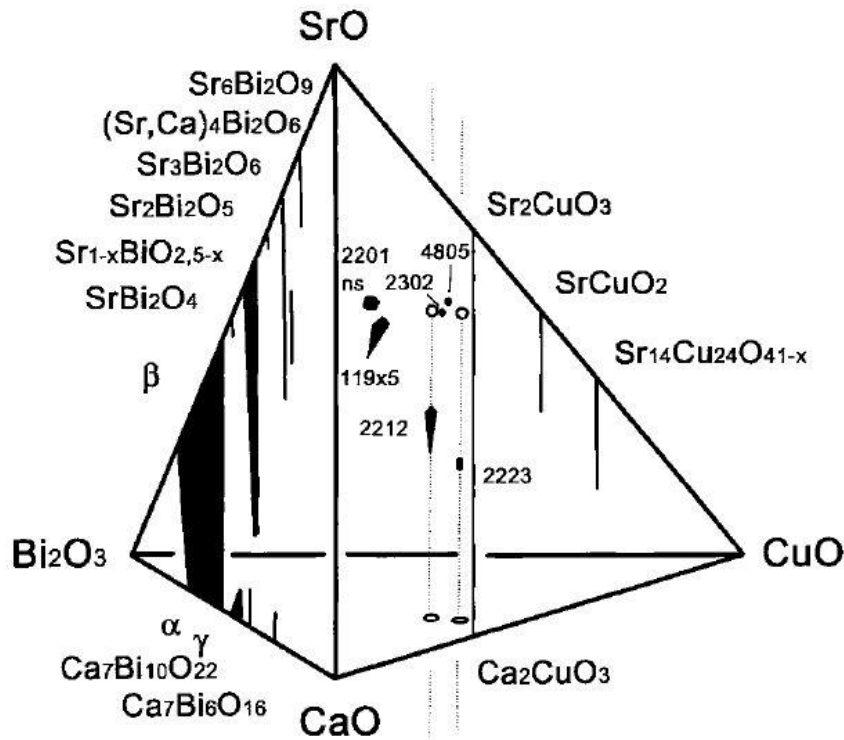


Figure 1-10 quaternary phase diagram of the  $\text{Bi}_2\text{O}_3$ - $\text{SrO}$ - $\text{CaO}$ - $\text{CuO}$  system [106].

*Metallic precursor synthesis by mechanical alloying*

Mechanical alloying (MA) is a dry, high energy ball milling process used to produce composite metal powder with a fine controlled microstructure. It was first studied around 1966 at INCO's Paul D Merica Research Laboratory to produce an alloy combining oxide dispersion strengthening with gamma prime precipitation hardening in a nickel-based super alloy [113]. It has been widely used since in processing a variety of alloys [114-123]; a schematic diagram of mechanical alloying of a single ball-powder-ball collision is illustrated in Figure 1-11 [124]. During this process, while powder particles are trapped between colliding grinding balls, there reaches an extreme state of hydrostatic compression and thus

materials that are brittle under tensile loading experience a large amount of plastic strain before fracture. As processing continues, repeated welding and fracturing occurs, leading to continual refinement of the internal structure of the metal powder. Finally, a balance is achieved between welding and fracturing, and a steady state particle size distribution develops.

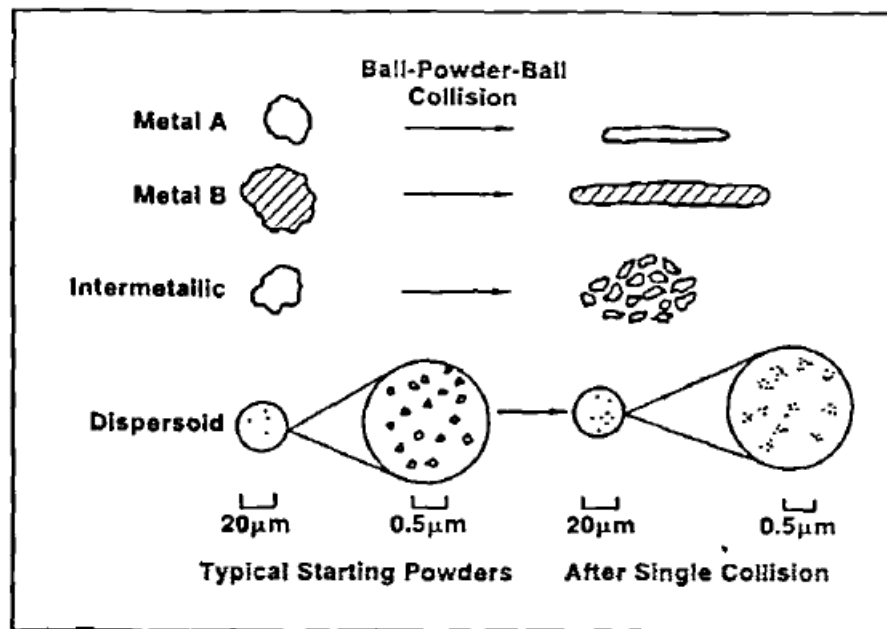


Figure 1-11 Schematic diagram of mechanical alloying of a single ball-powder-ball collision

[124].

Mechanical alloying (MA) is a nonequilibrium technique analogous to rapid solidification which modifies materials by refining the microstructure, homogenizing the composition, and extending solid solubilities [125]. With this method, solid-state amorphization reactions result from the severe mechanical deformation obtained by high-energy ball milling [125-

127]. The first definitive study of amorphization by MA was carried out by Koch et al. [128] in the easy-glass-forming alloy system Ni-Nb. It was argued by Schwarz et al. [129] and Hellstern and Schultz [130] that the process of amorphization by MA of elemental powders results in an ultrafine composite. Another key issue pertinent to MA processing is the formation of intermetallic compounds, discussed in detail by Koch [131, 132]. This method has been used to synthesize high magnetic field A15 superconductors such as Nb<sub>3</sub>Al and Nb<sub>3</sub>Sn [133] and recently has been applied to preparation of superconducting MgB<sub>2</sub> nanocrystalline precursor powder [134].

A homogeneous metallic precursor (MP) with controlled stoichiometry containing Bi, Sr, Ca, Cu, Ag, and its alloys is produced by mechanical alloying [37]. The starting metal powders are Bi, Sr, Ca, Cu and Ag. For one powder batch, 0.5-1.0 μm silver powder (purity of 99.9%) is added as well. After weighing and mixing all the powders in a high purity (<1 ppm oxygen) argon atmosphere in a glovebox, they are charged within a Spex zirconia milling vial and mechanically alloyed for 20 hours. Results show that Sr sticks preferably to the mixing media and that the intermittent scraping is beneficial. Note that Zr contamination from the ZrO<sub>2</sub> milling media is not found in the milled MP powder. After milling, powders are stored in glass vials in an argon atmosphere. Other than elemental metals, alloys like Ca-Cu and Sr-Bi also form during MA.

#### Direct oxidation of metallic precursors

Pressed MP pellets are formed to study the phase transformation and microstructure evolution during heat treatment. Schematic two-stage heat treatment profile is shown in Figure 1-12. The maximum temperature is between 800-855 °C, which is much lower than T<sub>peak</sub> in PMP. By introducing oxygen when Bi2212 starts to form and holding at an elevated

temperature for a sufficient time, the metallic precursors are oxidized and transformed into Bi2212.

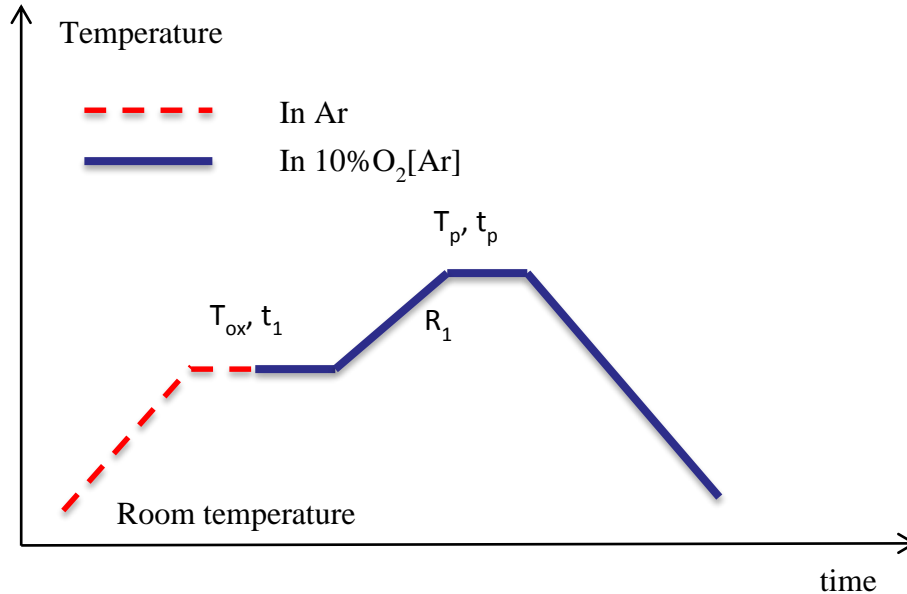


Figure 1-12 Schematic diagram of a two-step heat treatment profile to convert metallic precursor pellets into Bi2212 phase.

It is feasible to have Bi2201 as the only phase impurity after heat treatment, which is quite different from partial-melt processing of oxide precursors which results in AEC and CF phases as well. Any alloys formed during milling are reactive and not stable during heat treatment. Higher  $T_p$  and longer  $t_p$  facilitates conversion of metallic precursors to Bi2212 and a reduction of the Bi2201 content due to the very low diffusion rate of cations and high activation energy required to form Bi2212 via solid-state reactions [135, 136]. Furthermore, higher  $T_p$  results in larger and denser Bi2212 grains due to more efficient diffusion among grains [137, 138]. Although both Bi2201 and Bi2212 form in the temperature range 650 °C

to 790 °C [139], Bi2201 is more stable than Bi2212 and thus preferred. Additionally, the stability range of Bi2201 is only slightly reduced by decreasing the oxygen partial pressure, but is further reduced by increasing the temperature [140]. A higher heating rate  $R_1$  results in a shorter time between  $T_1$  and  $T_p$ , which suppresses the formation of Bi2201. Besides, the microstructure at the sample/silver interface suggests larger size and preferred orientation of Bi2212 grains with the aid of a silver surface.

#### Multifilamentary Bi2212/Ag wire/tape via MPIT route

Detrie and Sandhage made a monofilamentary Bi2212/Ag tape via solid metal-bearing precursor route [141]. Mixed  $\text{Bi}_2\text{O}_3$ , Sr, Ca and Cu powders were synthesized by mechanical alloying and filled into a Ag tube. After deformation and rolling, the tapes were 150-500  $\mu\text{m}$  thick with a core thickness of 50-160  $\mu\text{m}$ . The Ag along the side edges of the tapes was removed to facilitate oxidation processing. After oxidation and partial-melt in flowing oxygen, the resulting tapes exhibited average  $J_c$  of 320  $\text{A}/\text{mm}^2$  at 4.2K, self-field. But the samples used in Detrie and Sandhage's work were only 10 mm-20 mm in length and with one side of Ag sheath removed, which did not investigate the influence of closed Ag-sheath for long length application.

To make a multifilamentary wire via MPIT, the MP powders of around 100 gram were packed into a pure Ag tube in Ar atmosphere. The MP powder was tapped with tungsten rod down in the Ag tube on a vibration table and then vacuum sealed. A double-restack multifilamentary round wire was fabricated, as shown in Figure 1-13. The 1.05 mm diameter wire contains 7 bundles, the outer 6 bundles with 55 filaments ranging in size from 25  $\mu\text{m}$  to 40  $\mu\text{m}$ ; the fill factor is 30%. Part of the round wires was cold-rolled into flat tapes to reduce the Ag sheath thickness and filament size, as shown in Figure 1-14.

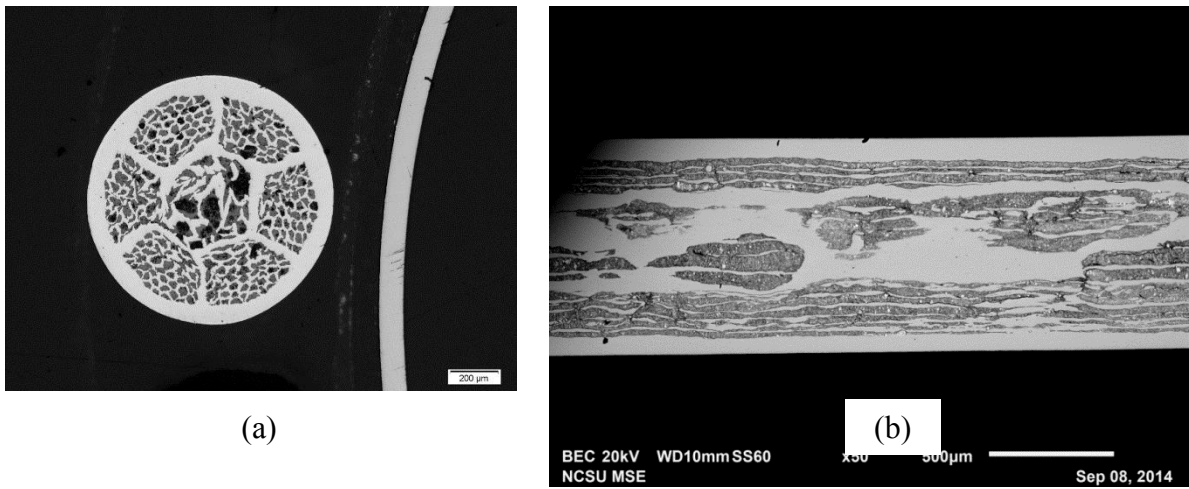


Figure 1-13 (a) cross-sectional and (b) longitudinal images of a multifilamentary MPIT round wire before heat treatment.

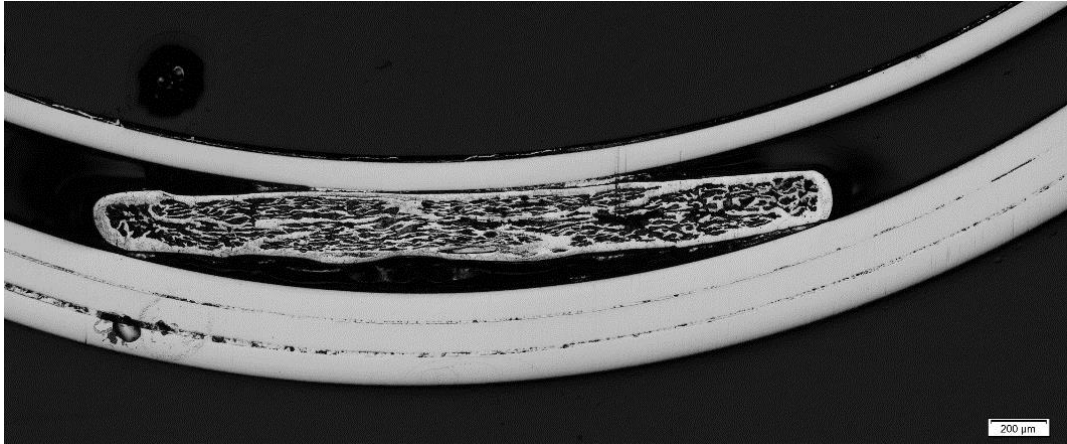


Figure 1-14 Cross-sectional image of a multifilamentary MPIT rolled tapes before heat treatment.

Heat treatment on Ag-sheathed round wires is different from direct oxidation on MP pellets. A series of heat treatments including oxidation, conversion to Bi2212 and PMP in pure O<sub>2</sub> are performed.

Three pathways of MP oxidation are identified in Ag-sheathed MPIT wires. The first one is direct reaction between MP powders and gaseous oxygen in the atmosphere. At the ends of wire, oxygen diffuses through the wire open ends and oxidizes MP powders quickly. The second one is the reaction between MP powders and atomic oxygen permeated through Ag sheath, both from outer and inter-filamentary Ag sheath. This pathway applies to the wire section where gaseous oxygen from the atmosphere is not available but Bi-rich liquid hasn't formed. The third one is the reaction between MP powders and the oxygen permeated

through both Ag sheath and Bi-rich liquid. This pathway applies to the middle section of the wire. Due to the affinity to oxygen, metallic, liquid Bi liquid infiltrates Ag grain boundaries, migrates towards the incoming oxygen and eventually concentrates at wire/atmosphere free surface.

For rolled tapes, thinner Ag sheath and smaller filament size allows faster MP oxidation. Although Bi-rich liquid still forms and starts to migrate through Ag grain boundaries, however, it is oxidized into  $\text{Bi}_2\text{O}_3$  and stops migration before reaching and concentrated at the wire/atmosphere free surface. The overall oxidation along the total 50 mm length of tape is homogeneous and without severe deformation. This serves as a prerequisite for homogeneous phase transformation into Bi2212 and enhanced texture in the following stages. After conversion stage at an elevated temperature of 830 °C, in the filaments where MP is fully oxidized, highly dense and homogeneous sub-oxides are obtained. The sub-oxides are of similar sizes of the metallic powders, and thus the homogeneity of elemental distribution is on the same order of a green MP wire.

After PMP, highest  $J_c$  obtained via MPIT is 415 A/mm<sup>2</sup> (self-field, 5T) after a complete heat treatment including oxidation, conversion and PMP stages. For 50 mm long samples,  $J_c$  measured only 10 mm from the round wire end is 2-4 times higher than in the middle section of each wire, indicating significant inhomogeneity in performance along the round wires. But for rolled tapes, the difference in  $J_c$  along the sample is within 3%.

#### Advantages over OPIT route

Highly dense filaments containing micron-size Bi2212 grains are obtained after conversion stage but before PMP, which is significantly different from the 70%-80% dense OPIT green

wire, indicating that starting with metallic precursors, over 95% dense Bi2212 filaments can be obtained.

After PMP, uni-axially c-axis textured Bi2212 grains within one filament are observed, which is different from a circular distribution of an OPIT Bi2212 after PMP [142]. The Bi2212 basal-planes from a wire cross section nearly extend to the total filament. Furthermore, Bi2201 grains are not observable, which is consistent with previous study on MP pellets [37].

#### Current-limiting factors in MPIT wires

The most negative factor on transport properties of MPIT wires is the filament discontinuity. Severe sausaging phenomenon is observed during wire deformation. The filament size varies along the wire length in a random distribution without obvious periodicity. Inhomogeneous filament microstructure and undulations of Ag/filament interface lead to reduced c-axis texture at the point of curvature change. Recrystallized Bi2212 grains during solidification in PMP follow the interface orientations, which reduce the macroscopic c-axis texture along the wire. Furthermore, some of the filaments smears and break, resulting in discontinued filaments of a length less than 500  $\mu\text{m}$ , which remain after heat treatment and were incapable of carrying current macroscopically [28].

Another current-limiting factor is the incomplete phase transformation from MP to Bi2212 due to cation depletion and oxygen deficiency during oxidation and conversion stages. Enhanced  $J_c$  homogeneity is achieved by smaller filament size and thinner Ag sheath thickness by rolling into tapes.

#### **Motivation and outline of this thesis**

Bi2212 Ag/Ag-alloy sheathed wire is the only high field superconductor available as an isotropic round wire. Powder-in-tube is the common method to fabricate multifilamentary wires. After deformation, the wires go through PMP, resulting in a complex heterogeneous microstructure. Wire transport properties,  $J_c(B, T)$ , depends not only on PMP conditions, but also largely on precursor powder properties. Although there are many studies on phase transformation and microstructure evolution during wire processing [37, 38], studies on precursor powder synthesis and properties are very limited.

Conventional oxide-powder-in-tube method uses high-purity Bi2212 powders as oxide precursors, which are usually synthesized via solid-state route or liquid-state route. Each of these methods, however, has its own disadvantages, which cannot produce Bi2212 powders that meet the requirements in stoichiometry, chemical homogeneity, carbon content, phase assemblage, grain size and large-scale production altogether. A new synthesis method is definitely needed. Furthermore, the effects of precursor powder properties on final wire performance are not clear. What is the ideal powder to make Bi2212/Ag wires remains a very important question to be answered. Most of the powder studies either focused solely on the synthesis process and properties of Bi2212 bulk materials [42, 43] or studied oxide precursor properties by comparing superconducting tapes/thick films that had varying methods, geometries and substrates [44-50]. A fundamental understanding of the relationships between powder properties and multifilamentary wire transport properties is essential to developing strategies for raising  $J_c$  by improved powder processing, alternative processing routes and better wire architectures.

In addition, issues with OPIT wires as low tap-density, bubbling [35, 84, 86, 92-94], and poor electromechanical performance [96] cannot be addressed by improving oxide precursor,

over-pressure processing or optimizing wire architecture. An alternative way with the potential to address these issues is the MPIT route, but studies on MPIT route on multifilamentary Bi2212/Ag wires remain under-developed. Detailed studies on the correlations between metallic precursor synthesis, heat treatment conditions, phase transformations, microstructure development and the final wire transport properties are crucial to the Bi2212/Ag multifilamentary wire development for high-field applications.

This thesis specifically focuses on the precursor powder synthesis for Bi2212/Ag multifilamentary wires, establishing key process-microstructure-properties relationships between precursor powder and wire performance. To achieve this goal, this thesis work will study the physical, chemical, magnetic and microstructural properties of Bi2212 precursor powder synthesized from two approaches, oxide and metallic. Furthermore, this thesis will focus on the relationships between precursor powder and Bi2212/Ag multifilamentary wire transport properties to answer the following questions:

How to synthesize Bi2212 oxide precursors to meet the requirements for fabricating Bi2212/Ag multifilamentary wires? What are the key properties of the Bi2212 powder that affect the wire transport properties? How to tailor oxide precursor to improve wire transport?  
(Chapter 2)

How to synthesize metallic precursor and convert to Bi2212 phase? What are the key differences in phase assemblage and microstructure between oxide precursor and metallic precursor? (Chapter 3)

How to fabricate a Bi2212/Ag multifilamentary wire via MPIT method? What types of chemical reactions, phase transformations and microstructural evolutions will occur in MPIT

wires? Why is MPIT method potentially advantageous over OPIT method and how to address the current-limiting factors? (Chapter 4)

Chapter 5 summarizes this thesis work and proposes the future work.

## REFERENCES

- [1] P. F. Dahl, "Kamerlingh Onnes and the Discovery of Superconductivity: The Leyden Years, 1911-1914," *Historical Studies in the Physical Sciences*, vol. 15, pp. 1-37, 1984.
- [2] D. A. Cardwell and D. S. Ginley, *Handbook of Superconducting Materials*: Institute of Physics, 2003.
- [3] W. Meissner and R. Ochsenfeld, "Ein neuer Effekt bei Eintritt der Supraleitfähigkeit," *Naturwissenschaften*, vol. 21, pp. 787-788, 1933/11/01 1933.
- [4] J. Bardeen, *et al.*, "Theory of Superconductivity," *Physical Review*, vol. 108, pp. 1175-1204, 1957.
- [5] L. N. Cooper, "Bound Electron Pairs in a Degenerate Fermi Gas," *Physical Review*, vol. 104, pp. 1189-1190, 1956.
- [6] <http://physics.aalto.fi/groups/nanospin/facilities/pulsed-laser-deposition/critical/>.
- [7] L. Landau, "On the Theory of Superfluidity," *Physical Review*, vol. 75, pp. 884-885, 1949.
- [8] M. Cyrot, "Ginzburg-Landau theory for superconductors," *Reports on Progress in Physics*, vol. 36, p. 103, 1973.
- [9] A. A. Abrikosov, "Vliyanie razmerov na kriticheskoe pole sverkhprovodnikov vtoroi gruppy," *Dokl. Akad. nauk SSSR*, vol. 86, p. 489, 1952.
- [10] E. H. Brandt, "Vortices in superconductors," *Physica C: Superconductivity*, vol. 369, pp. 10-20, 2002.
- [11] H. Maeda, *et al.*, "A New High-  $T_c$  Oxide Superconductor without a Rare Earth Element," *Japanese Journal of Applied Physics*, vol. 27, p. L209, 1988.
- [12] P. Majewski, "BiSrCaCuO High- $T_c$  Superconductors," *Advanced Materials*, vol. 6, pp. 460-469, 1994.
- [13] K. H. Fischer, "Vortices in layered high- $T_c$  superconductors," *Physica C: Superconductivity*, vol. 178, pp. 161-170, 1991.
- [14] J. Schwartz, *et al.*, "High field superconducting solenoids via high temperature superconductors," *IEEE Transactions on Applied Superconductivity*, vol. 18, pp. 70-81, 2008.

- [15] [https://nationalmaglab.org/images/magnet\\_development/asc/plots/JeChart041614-1022x741-pal.png](https://nationalmaglab.org/images/magnet_development/asc/plots/JeChart041614-1022x741-pal.png).
- [16] A. Devred, *et al.*, "Future accelerator magnet needs," *IEEE Transactions on Applied Superconductivity*, vol. 15, pp. 1192-1199, Jun 2005.
- [17] L. Rossi, "Superconductivity: its role, its success and its setbacks in the Large Hadron Collider of CERN," *Superconductor Science and Technology*, vol. 23, Mar 2010.
- [18] S. A. Gourlay, *et al.*, "Magnet R&D for the US LHC Accelerator Research Program (LARP)," *IEEE Transactions on Applied Superconductivity*, vol. 16, pp. 324-327, Jun 2006.
- [19] [http://www.wtec.org/loyola/scpa/05\\_02.htm](http://www.wtec.org/loyola/scpa/05_02.htm).
- [20] L. R. Motowidlo, *et al.*, "Multifilament BPSCCO superconductor: fabrication and heat treatment study," *Ieee Transactions on Applied Superconductivity*, vol. 3, pp. 942-945, 1993.
- [21] F. M. G. Johnson and P. Larose, "The diffusion of oxygen through silver," *Journal of the American Chemical Society*, vol. 46, pp. 1377-1389, 1924/06/01 1924.
- [22] T. A. Ramanarayanan and R. A. Rapp, "Diffusivity and Solubility of O in Liquid Sn and Solid Ag and the Diffusivity of O in Solid Ni," *Metall. Trans.*, vol. 3, pp. 3239-3246, 1972.
- [23] P. Franke and D. Neuschütz, "Ag-O (Silver - Oxygen)," in *Binary Systems. Part 5: Binary Systems Supplement 1*. vol. 19B5, P. Franke and D. Neuschütz, Eds., ed: Springer Berlin Heidelberg, 2007, pp. 1-2.
- [24] H. Kumakura, *et al.*, "Influence of Ag substrates on grain alignment and critical current density of Bi-2212 tape conductors," *IEEE Transactions on Applied Superconductivity*, vol. 9, pp. 1804-1807, 1999.
- [25] Y. Feng and D. C. Larbalestier, "Texture relationships and interface structure in Ag-sheathed Bi(Pb)-Sr-Ca-Cu-O superconducting tapes," *Interface Science*, vol. 1, pp. 401-410, 1994/12/01 1994.
- [26] H. Hong-Soo, *et al.*, "The effects of drawing parameters on sausageing and critical current density of Bi-2223/Ag HTS wires," *Ieee transactions on Applied Superconductivity*, vol. 11, pp. 3748-3751, 2001.
- [27] G. Naderi, *et al.*, "Bi2212 round wire processing studies based on split melt and introducing saw-tooth processing," presented at the International Cryogenic Materials Conference, 2011.

- [28] W. G. Wang, *et al.*, "The effect of mechanical deformation on silver - core interface and critical current density in Ag - Bi-2223 single- and multifilament tapes," *Superconductor Science and Technology*, vol. 9, p. 875, 1996.
- [29] K. R. Marken, *et al.*, "Progress in BSCCO-2212/silver composite tape conductors," *IEEE Transactions on Applied Superconductivity*, vol. 7, pp. 2211-2214, 1997.
- [30] K. R. Marken, *et al.*, "Processing issues for high critical current density in BSCCO-2212 composites," *IEEE Transactions on Applied Superconductivity*, vol. 11, pp. 3252-3255, 2001.
- [31] A. Malagoli, *et al.*, "Large critical current density improvement in Bi-2212 wires through the groove-rolling process," *Superconductor Science and Technology*, vol. 26, p. 045004, 2013.
- [32] A. S. Alexandrov, *et al.*, "Resistive Upper Critical Field of High- $T_c$  Single Crystals of Bi2212," *Physical Review Letters*, vol. 76, pp. 983-986, 1996.
- [33] Y. Wang, *et al.*, "Dependence of upper critical field and pairing strength on doping in cuprates," *Science*, vol. 299, pp. 86-89, January 3, 2003 2003.
- [34] Y. Ando and K. Segawa, "Magnetoresistance of Untwinned YBCO single crystals in a wide range of doping: anomalous hole doping dependence of the coherence length," *Physical Review Letters*, vol. 88, p. 167005, 2002.
- [35] W. T. Nachtrab, *et al.*, "Effect of Solidification Conditions on Partial Melt Processed Bi2212/Ag Round Wire," *IEEE Transactions on Applied Superconductivity*, vol. 21, pp. 2795-2799, Jun 2011.
- [36] T. Hatano, *et al.*, "High-temperature X-ray study of melting and solidification of the  $\text{Bi}_2\text{Sr}_2\text{CaCu}_2\text{O}_{8+\delta}$  on silver," *Journal of Low Temperature Physics*, vol. 117, pp. 777-781, 1999.
- [37] Y. Zhang, *et al.*, "Synthesis of  $\text{Bi}_2\text{Sr}_2\text{CaCu}_2\text{O}_x$  superconductors via direct oxidation of metallic precursors," *Superconductor Science and Technology*, vol. 27, p. 055016, 2014.
- [38] Y. Zhang, *et al.*, "Studies on multifilamentary  $\text{Bi}_2\text{Sr}_2\text{CaCu}_2\text{O}_x/\text{Ag}$  wire via metallic-powder-in-tube route," *Manuscript in progress*, 2015.
- [39] X. T. Liu, *et al.*, "Influencing factors on the electrical transport properties of split-melt processed  $\text{Bi}_2\text{Sr}_2\text{CaCu}_2\text{O}_x$  round wires," *Superconductor Science and Technology*, vol. 25, Jul 2012.

- [40] S. Tengming, *et al.*, "Heat treatment control of Ag–Bi<sub>2</sub>Sr<sub>2</sub>CaCu<sub>2</sub>O<sub>x</sub> multifilamentary round wire: investigation of time in the melt," *Superconductor Science and Technology*, vol. 24, p. 115009, 2011.
- [41] C. Evan Benjamin, *et al.*, "Statistical analysis of the relationship between electrical transport and filament microstructure in multifilamentary Bi<sub>2</sub>Sr<sub>2</sub>CaCu<sub>2</sub>O<sub>x</sub>/Ag/Ag–Mg round wires," *Superconductor Science and Technology*, vol. 27, p. 044020, 2014.
- [42] H. Miao, *et al.*, "Studies of Precursor Composition Effect on J<sub>c</sub> in Bi-2212/Ag Wires and Tapes," *AIP Conference Proceedings*, vol. 824, pp. 673-682, 2006.
- [43] M. O. Rikel, *et al.*, "Effect of composition on the melting behaviour of Bi2212-Ag conductors," *Journal of Physics: Conference Series*, vol. 43, p. 51, 2006.
- [44] N. Tohge, *et al.*, "Direct preparation of fine powders of the 80 K superconducting phase in the Bi-Ca-Sr-Cu-O system by spray pyrolysis," *Japanese Journal of Applied Physics*, vol. 28, p. L1175, 1989.
- [45] J. Fransaer, *et al.*, "Sol-gel preparation of high-T<sub>c</sub> Bi-Ca-Sr-Cu-O and Y-Ba-Ca-O superconductors," *Journal of Applied Physics*, vol. 65, pp. 3277-3279, 1989.
- [46] T. Tsukamoto, *et al.*, "Preparation and superconducting properties of high-quality Bi-2212 ceramics," *Journal of Alloys and Compounds*, vol. 209, pp. 225-229, 1994.
- [47] D. Sager, *et al.*, "Novel precursor reaction pathways to Bi-2212 bulk superconductors," *Physica C: Superconductivity*, vol. 417, pp. 85-97, 2005.
- [48] A. Polasek, *et al.*, "The influence of precursor powder on the microstructure and properties of Bi-2212 blocks," *Physica C: Superconductivity*, vol. 460–462, Part 2, pp. 1349-1350, 2007.
- [49] A. Sotelo, *et al.*, "Precursor influence on the electrical properties of textured Bi-2212 superconductors," *Journal of Superconductivity and Novel Magnetism*, vol. 24, pp. 19-25, Jan 2011.
- [50] V. Garnier, *et al.*, "Relationship among synthesis, microstructure and properties in sinter-forged Bi-2212 ceramics," *Physica C: Superconductivity*, vol. 319, pp. 197-208, 1999.
- [51] E. E. Hellstrom and W. Zhang, "Formation and prevention of bubbles when melt processing Ag-sheathed Bi<sub>2</sub>Sr<sub>2</sub>CaCu<sub>2</sub>O<sub>x</sub> (2212) conductors," *Superconductor Science and Technology*, vol. 8, p. 317, 1995.
- [52] W. Zhang, *et al.*, "Formation of Porosity and Its Effects on the Uniformity of J<sub>c</sub> in Bi-2212/Ag Tapes," in *Advances in Cryogenic Engineering Materials*. vol. 44, U. B. Balachandran, *et al.*, Eds., ed: Springer US, 1998, pp. 509-516.

- [53] M. O. Rikel, *et al.*, "Competitiveness of porosity and phase purity in melt processed Bi2212/Ag conductors," *Physica C: Superconductivity*, vol. 354, pp. 321-326, 2001.
- [54] J. Jiang, *et al.*, "Doubled critical current density in Bi-2212 round wires by reduction of the residual bubble density," *Superconductor Science and Technology*, vol. 24, p. 082001, 2011.
- [55] C. Scheuerlein, *et al.*, "Void and phase evolution during the processing of Bi-2212 superconducting wires monitored by combined fast synchrotron micro-tomography and x-ray diffraction," *Superconductor Science and Technology*, vol. 24, p. 115004, 2011.
- [56] T. Shen, *et al.*, "Role of internal gases and creep of Ag in controlling the critical current density of Ag-sheathed Bi<sub>2</sub>Sr<sub>2</sub>CaCu<sub>2</sub>O<sub>x</sub> wires," *Journal of Applied Physics*, vol. 113, pp. -, 2013.
- [57] W. Zhang and E. E. Hellstrom, "The influence of carbon on melt processing Ag sheathed Bi<sub>2</sub>Sr<sub>2</sub>CaCu<sub>2</sub>O<sub>8</sub> tape," *Physica C: Superconductivity*, vol. 234, pp. 137-145, 1994.
- [58] J. F. Mitchell, *et al.*, "Rapid synthesis of 93 K Bi-2212 superconductor from hydroxide precursors," *Physica C: Superconductivity*, vol. 245, pp. 126-130, 1995.
- [59] A. P. Baker and B. A. Glowacki, "The effect of Bi content on the phase purity and the superconducting critical temperature of a Sr and Ca deficient Bi-2212 stoichiometry," *Physica C: Superconductivity*, vol. 227, pp. 31-39, 1994.
- [60] D. Sager, *et al.*, "Influence of precursor calcination parameters on the critical current density of Bi-2212 superconductors," *Physica C: Superconductivity*, vol. 434, pp. 125-134, 2006.
- [61] I. Bloom, *et al.*, "Solid state synthesis of Bi<sub>2</sub>Sr<sub>2</sub>CaCu<sub>2</sub>O<sub>x</sub> superconductor," *Materials Research Bulletin*, vol. 26, pp. 1269-1276, 1991.
- [62] S. Yoshizawa, *et al.*, "Effect of particle size in raw material CuO on superconductivity of HTSC," in *Advances in Superconductivity III*, K. Kajimura and H. Hayakawa, Eds., ed: Springer Japan, 1991, pp. 287-290.
- [63] S. C. Kim, *et al.*, "Effect of composition on critical current density of Bi2212/Ag round wires," *Cryogenics*, vol. 49, pp. 277-279, 2009.
- [64] N. Tohge, *et al.*, "Preparation conditions and morphology of superconducting fine particles in the Bi-Ca-Sr-Cu-O system prepared by spray pyrolysis," *Journal of the American Ceramic Society*, vol. 74, pp. 2117-2122, 1991.

- [65] Y. Idemoto, *et al.*, "Oxygen nonstoichiometry of 2223 phase Bi-Pb-Sr-Ca-Cu-O system superconducting oxide," *Physica C: Superconductivity*, vol. 181, pp. 171-178, 1991.
- [66] J. Takada, *et al.*, "Superconductor with  $T_c = 117$  K in the Bi-Pb-Sr-Ca-Cu-O system," *Physica C: Superconductivity*, vol. 170, pp. 249-253, 1990.
- [67] L. Ben-Dor, *et al.*, "Physical characterization and vibrational spectroscopy of Bi(Pb) cuprate 2212 ceramics prepared by sol-gel," *Physica C: Superconductivity*, vol. 200, pp. 418-424, 1992.
- [68] T. G. Holesinger, *et al.*, "Characterization of the phase relations and solid solution range of the  $\text{Bi}_2\text{Sr}_2\text{Ca}_1\text{Cu}_2\text{O}_y$  superconductor," *Physica C: Superconductivity*, vol. 202, pp. 109-120, 1992.
- [69] W. Zhang, *et al.*, "Composition studies for Ag-sheathed  $\text{Bi}_2\text{Sr}_2\text{CaCu}_2\text{O}_x$  conductors processed in 100%  $\text{O}_2$ ," *Superconductor Science and Technology*, vol. 9, p. 211, 1996.
- [70] X. Liu, *et al.*, "Influencing factors on the electrical transport properties of split-melt processed  $\text{Bi}_2\text{Sr}_2\text{CaCu}_2\text{O}_x$  round wires," *Superconductor Science and Technology*, vol. 25, p. 075008, 2012.
- [71] X. T. Liu, *et al.*, "Effect of resolidification conditions on  $\text{Bi}_2\text{Sr}_2\text{CaCu}_2\text{O}_x/\text{Ag}/\text{AgMg}$  coil performance," *IEEE Transactions on Applied Superconductivity*, vol. 19, pp. 2232-2236, 2009.
- [72] T. G. Holesinger, *et al.*, "Solid-solution region of the  $\text{Bi}_2\text{Sr}_2\text{CaCu}_2\text{O}_y$  superconductor," *Physica C*, vol. 217, pp. 85-96, Nov 1993.
- [73] P. Majewski, *et al.*, "The High- $T_c$  superconducting solid solution  $\text{Bi}_{2-x}(\text{Sr,Ca})_3\text{Cu}_2\text{O}_{8+d}$  (2212 Phase)-chemical composition and superconducting properties," *Advanced Materials*, vol. 4, pp. 508-511, 1992.
- [74] H. Kumakura, *et al.*, "Effect of high oxygen partial pressure heat treatment on the superconducting properties of  $\text{Bi}_2\text{Sr}_2\text{CaCu}_2\text{O}_x/\text{Ag}$  tapes," *Journal of Applied Physics*, vol. 80, pp. 5162-5168, 1996.
- [75] H. Miao, *et al.*, "Development of Bi-2212 conductors for magnet applications," in *AIP Conference Proceedings*. vol. 711, ed, 2004, pp. 603-611.
- [76] K. Sandhage, *et al.*, "Critical issues in the OPIT processing of high- $J_c$  BSCCO superconductors," *The Journal of The Minerals, Metals & Materials Society*, vol. 43, pp. 21-25, 1991/03/01 1991.

- [77] G. D. Ulrich and N. S. Subramanian, "III. Coalescence as a Rate-Controlling Process," *Combustion Science and Technology*, vol. 17, pp. 119-126, 1977/12/01 1977.
- [78] G. R. Paz-Pujalt, "Solid state reactions in the formation of Bi-Sr-Ca-Cu-oxide superconductor from metallo-organic precursors," *Physica C: Superconductivity*, vol. 166, pp. 177-184, 1990.
- [79] G. Naderi, *et al.*, "Understanding processing–microstructure–properties relationships in  $\text{Bi}_2\text{Sr}_2\text{CaCu}_2\text{O}_x$  /Ag round wires and enhanced transport through saw-tooth processing," *Superconductor Science and Technology*, vol. 26, p. 105010, 2013.
- [80] E. E. Hellstrom, *et al.*, "Phase development and microstructure in Bi-based 2212 Ag-clad tapes processed at 880, 890, and 905 °C: The Cu-free phase and  $(\text{Sr,Ca})\text{CuO}_2$ ," *Applied Superconductivity*, vol. 1, pp. 1535-1545, 1993.
- [81] M. Polak, *et al.*, "The effect of the maximum processing temperature on the microstructure and electrical properties of melt processed Ag-sheathed  $\text{Bi}_2\text{Sr}_2\text{CaCu}_2\text{O}_x$  tape," *IEEE Transactions on Applied Superconductivity*, vol. 7, pp. 1537-1540, 1997.
- [82] T. Shen, *et al.*, "Role of internal gases and creep of Ag in controlling the critical current density of Ag-sheathed  $\text{Bi}_2\text{Sr}_2\text{CaCu}_2\text{O}_x$  wires," *Journal of Applied Physics*, vol. 113, p. 213901, 2013.
- [83] H. Miao, *et al.*, "Long length AgMg clad Bi-2212 multifilamentary tapes," *AIP Conference Proceedings*, vol. 614, pp. 709-716, 2002.
- [84] T. D. Aksenova, *et al.*, "Texture Formation in  $\text{Bi}_2\text{Sr}_2\text{Ca}_1\text{Cu}_2\text{O}_x$ /Ag Tapes Prepared By Thick Films," *Physica C*, vol. 205, pp. 271-279, Feb 1993.
- [85] W. T. Nachtrab, *et al.*, "The Effect of Filament Diameter on  $J_c$  in High Filament Count Bi2212/Ag Round Wire," *IEEE Transactions on Applied Superconductivity*, vol. 19, pp. 3061-3066, 2009.
- [86] A. Polasek, *et al.*, "Partial melt processing of high- $T_c$  bulk Bi-2212 starting from different precursor powders," in *8th European Conference on Applied Superconductivity*. vol. 97, S. Hoste and M. Ausloos, Eds., ed Bristol: Iop Publishing Ltd, 2008.
- [87] P. Majewski, *et al.*, " Relationships between the chemical composition and properties of the high-temperature superconductor  $\text{Bi}_{2+x}\text{Sr}_{2-y}\text{Ca}_{1+y}\text{Cu}_2\text{O}_{8+d}$ ," *Journal of Materials Science*, vol. 32, pp. 5137-5141, 1997.
- [88] J. Fransaer, *et al.*, "Sol-gel preparation of high- $T_c$  Bi-Ca-Sr-Cu-O and Y-Ba-Ca-O superconductors," *Journal of Applied Physics*, vol. 65, pp. 3277-3279, 1989.

- [89] R. S. FEIGELSON, *et al.*, "Superconducting Bi-Ca-Sr-Cu-O fibers grown by the laser-heated pedestal growth method," *Science*, vol. 240, pp. 1642-1645, June 17, 1988 1988.
- [90] H. Miao, *et al.*, "Optimization of melt-processing temperature and period to improve critical current density of Bi<sub>2</sub>Sr<sub>2</sub>CaCu<sub>2</sub>O<sub>x</sub>/Ag multilayer tapes," *Physica C*, vol. 320, pp. 77-86, Jul 1999.
- [91] Y. Zhang, *et al.*, "Synthesis of Bi<sub>2</sub>Sr<sub>2</sub>CaCu<sub>2</sub>O<sub>x</sub> oxide precursor from nano-oxides and its relationship with multifilamentary wire transport properties," *manuscript in progress*, 2015.
- [92] T. Lang, *et al.*, "Influence of the maximum temperature during partial melt-processing of Bi-2212 thick films on microstructure and j(c)," *Physica C*, vol. 294, pp. 7-16, Jan 1998.
- [93] T. Lang, *et al.*, "Phase assemblage and morphology during the partial melt processing of Bi-2212 thick films," *Physica C*, vol. 281, pp. 283-292, Aug 1997.
- [94] K. Nomura, *et al.*, "Fabrication conditions and superconducting properties of Ag-sheathed Bi-Sr-Ca-Cu-O tapes prepared by partial melting and slow cooling process," *Applied Physics Letters*, vol. 62, pp. 2131-2133, Apr 1993.
- [95] D. C. Larbalestier, *et al.*, "Isotropic round-wire multifilament cuprate superconductor for generation of magnetic fields above 30 T," *Nature Materials*, vol. 13, pp. 375-381, 2014.
- [96] G. Naderi and J. Schwartz, "Multiscale studies of processing-microstructure-transport relationships in over- pressure processed Bi 2 Sr 2 CaCu 2 O x /Ag multifilamentary round wire," *Superconductor Science and Technology*, vol. 27, p. 115002, 2014.
- [97] M. Minami, *et al.*, "Research and development of superconducting magnetic energy storage system - Influence of mechanical properties of Bi-2212/Ag Rutherford cable to its critical current," *Physica C*, vol. 357, pp. 1323-1326, Aug 2001.
- [98] M. T. Malachovsky and C. A. D'Ovidio, "SEM investigation of the critical current degradation onset in BSCCO-2223 multifilamentary tapes submitted to bending," *Superconductor Science and Technology*, vol. 18, pp. 289-293, Mar 2005.
- [99] Q. V. Le, *et al.*, "Two-dimensional peridynamic simulation of the effect of defects on the mechanical behavior of Bi<sub>2</sub>Sr<sub>2</sub>CaCu<sub>2</sub>O<sub>x</sub> round wires," *Superconductor Science and Technology*, vol. 27, p. 115007, 2014.

- [100] A. L. Mbaruku and J. Schwartz, "Statistical analysis of the electromechanical behavior of AgMg sheathed  $\text{Bi}_2\text{Sr}_2\text{CaCu}_2\text{O}_{8+x}$  superconducting tapes using Weibull distributions," *Journal of Applied Physics*, vol. 101, p. 073913, Apr 2007.
- [101] X. F. Gou and J. Schwartz, "Fractal analysis of the role of the rough interface between  $\text{Bi}_2\text{Sr}_2\text{CaCu}_2\text{O}_x$  filaments and the Ag matrix in the mechanical behavior of composite round wires " *Journal of Applied Physics (submitted)*, 2012.
- [102] A. Godeke, *et al.*, "Critical current of dense Bi-2212 round wires as a function of axial strain," *Superconductor Science and Technology*, vol. 28, p. 032001, 2015.
- [103] A. Otto, *et al.*, "Properties of high- $T_c$  wires made by the metallic precursor process," *Journal of the Minerals Metals & Materials Society*, vol. 45, pp. 48-52, Sep 1993.
- [104] A. Otto, *et al.*, "Multifilamentary Bi-2223 composite tapes made by a metallic precursor route," *Ieee Transactions on Applied Superconductivity, Vol 3, No 1, March 1993 Pts 2-4*, pp. 915-922, 1993.
- [105] A. Otto, *et al.*, "Progress towards a long length metallic precursor process for multifilament Bi-2223 composite superconductors," *Ieee Transactions on Applied Superconductivity*, vol. 5, pp. 1154-1157, Jun 1995.
- [106] P. Majewski, "Phase diagram studies in the system Bi-Pb-Sr-Ca-Cu-O- Ag," *Superconductor Science and Technology*, vol. 10, p. 453, 1997.
- [107] T. Shen, *et al.*, "Filament to filament bridging and its influence on developing high critical current density in multifilamentary  $\text{Bi}_2\text{Sr}_2\text{CaCu}_2\text{O}_x$  round wires," *Superconductor Science and Technology*, vol. 23, p. 025009, 2010.
- [108] J. Jiang, *et al.*, "Doubled critical current density in Bi-2212 round wires by reduction of the residual bubble density," *Superconductor Science & Technology*, vol. 24, p. 082001, 2011.
- [109] P. Majewski, "Phase diagram studies in the system Bi-Pb-Sr-Ca-Cu-O-Ag," *Superconductor Science and Technology*, vol. 10, p. 453, 1997.
- [110] L. M. Rubin, *et al.*, "Phase stability limits of  $\text{Bi}_2\text{Sr}_2\text{Ca}_1\text{Cu}_2\text{O}_{8+\delta}$  and  $\text{Bi}_2\text{Sr}_2\text{Ca}_2\text{Cu}_3\text{O}_{10+\delta}$ ," *Applied Physics Letters*, vol. 61, pp. 1977-1979, 1992.
- [111] L. M. Rubin, *et al.*, "Phase stability limits and solid-state decomposition of  $\text{Bi}_2\text{Sr}_2\text{CaCu}_2\text{O}_{8+\delta}$  and  $\text{Bi}_2\text{Sr}_2\text{Ca}_2\text{Cu}_3\text{O}_{10+\delta}$  in reduced oxygen pressures," *Physica C: Superconductivity*, vol. 217, pp. 227-234, 1993.
- [112] A. P. Mozhaev, *et al.*, "Phase stability, oxygen nonstoichiometry, and superconductivity properties of  $\text{Bi}_2\text{Sr}_2\text{CaCu}_2\text{O}_{8+\delta}$  and  $\text{Bi}_{1.8}\text{Pb}_{0.4}\text{Sr}_2\text{Ca}_2\text{Cu}_3\text{O}_{10+\delta}$ ," *Journal of Solid State Chemistry*, vol. 119, pp. 120-124, 1995.

- [113] P. S. Gilman and J. S. Benjamin, "Mechanical alloying," *Annual Review of Materials Science*, vol. 13, pp. 279-300, 1983.
- [114] H. Bahmanpour, *et al.*, "Mechanical behavior of bulk nanocrystalline copper alloys produced by high energy ball milling," *Journal of Materials Science*, vol. 46, pp. 6316-6322, Oct 2011.
- [115] R. K. Guduru, *et al.*, "Mechanical properties of nanocrystalline Fe-Pb and Fe-Al<sub>2</sub>O<sub>3</sub>," *Scripta Materialia*, vol. 54, pp. 1879-1883, Jun 2006.
- [116] R. K. Gupta, *et al.*, *Grain growth behaviour and consolidation of ball milled nanocrystalline iron-chromium alloys*. Warrendale: Minerals, Metals & Materials Soc, 2008.
- [117] H. Kotan, *et al.*, "Effect of annealing on microstructure, grain growth, and hardness of nanocrystalline Fe-Ni alloys prepared by mechanical alloying," *Materials Science and Engineering a-Structural Materials Properties Microstructure and Processing*, vol. 552, pp. 310-315, Aug 2012.
- [118] G. Liang and R. Schulz, "Phase structures and hydrogen storage properties of Ca-Mg-Ni alloys prepared by mechanical alloying," *Journal of Alloys and Compounds*, vol. 356-357, pp. 612-616, 2003.
- [119] T. D. Shen, *et al.*, "Solid-state reaction in nanocrystalline Fe/SiC composites prepared by mechanical alloying," *Journal of Materials Science*, vol. 32, pp. 3835-3839, Jul 1997.
- [120] K. M. Youssef, *et al.*, "Nanocrystalline Al-Mg alloy with ultrahigh strength and good ductility," *Scripta Materialia*, vol. 54, pp. 251-256, Jan 2006.
- [121] D. L. Zhang, *et al.*, "Bulk nanostructured Cu-2.5vol.%Al<sub>2</sub>O<sub>3</sub> alloy synthesized using high energy mechanical milling," in *Metastable, Mechanically Alloyed and Nanocrystalline Materials*. vol. 24-25, A. Inoue, Ed., ed Stafa-Zurich: Trans Tech Publications Ltd, 2005, pp. 639-642.
- [122] D. L. Zhang, *et al.*, "Applications of high energy mechanical milling in processing advanced materials: An overview of the understanding," in *Ismanam 2003: Metastable, Mechanically Alloyed and Nanocrystalline Materials*. vol. 20-21, C. S. Kiminami, *et al.*, Eds., ed Stafa-Zurich: Trans Tech Publications Ltd, 2004, pp. 103-110.
- [123] X. Zhang, *et al.*, "Preparation of bulk ultrafine-grained and nanostructured Zn, Al and their alloys by in situ consolidation of powders during mechanical attrition," *Scripta Materialia*, vol. 46, pp. 661-665, May 2002.

- [124] J. S. Benjamin, "Mechanical alloying — A perspective," *Metal Powder Report*, vol. 45, pp. 122-127, 1990.
- [125] C. C. Koch, "MATERIALS SYNTHESIS BY MECHANICAL ALLOYING," *Annual Review of Materials Science*, vol. 19, pp. 121-143, 1989.
- [126] C. C. Koch, "AMORPHIZATION BY MECHANICAL ALLOYING," *Journal of Non-Crystalline Solids*, vol. 117, pp. 670-678, Feb 1990.
- [127] C. C. Koch, "AMORPHIZATION REACTIONS DURING MECHANICAL ALLOYING/MILLING OF METALLIC POWDERS," *Sibirskii Khimicheskii Zhurnal*, pp. 67-75, 1991.
- [128] C. C. Koch, *et al.*, "Preparation of ``amorphous" Ni<sub>60</sub>Nb<sub>40</sub> by mechanical alloying," *Applied Physics Letters*, vol. 43, pp. 1017-1019, 1983.
- [129] R. B. Schwarz, *et al.*, "The synthesis of amorphous Ni Ti alloy powders by mechanical alloying," *Journal of Non-Crystalline Solids*, vol. 76, pp. 281-302, 1985.
- [130] P. F. Miceli, *et al.*, "X-ray refractive index: A tool to determine the average composition in multilayer structures," *Applied Physics Letters*, vol. 48, pp. 24-26, 1986.
- [131] C. C. Koch, "Intermetallic matrix composites prepared by mechanical alloying - a review," *Materials Science and Engineering a-Structural Materials Properties Microstructure and Processing*, vol. 244, pp. 39-48, Mar 1998.
- [132] C. C. Koch and J. D. Whittenberger, "Mechanical milling/alloying of intermetallics," *Intermetallics*, vol. 4, pp. 339-355, 1996.
- [133] F. A. Santos, *et al.*, "Obtaining and stability verification of superconducting phases of the Nb-Al and Nb-Sn systems by mechanical alloying and low-temperature heat treatments," *Journal of Alloys and Compounds*, vol. 491, pp. 187-191, Feb 2010.
- [134] W. Haessler, *et al.*, "Superconducting MgB<sub>2</sub> tapes prepared using mechanically alloyed nanocrystalline precursor powder," *Ieee Transactions on Applied Superconductivity*, vol. 17, pp. 2919-2921, Jun 2007.
- [135] M. O. Rikel and E. E. Hellstrom, "Development of 2201 intergrowths during melt processing Bi<sub>2</sub>Sr<sub>2</sub>Ca<sub>n-1</sub>Cu<sub>n</sub>O<sub>y</sub> with n=1,2, and 3," *Physica C: Superconductivity*, vol. 357-360, Part 2, pp. 1081-1090, 2001.
- [136] J. M. Tarascon, *et al.*, "Preparation, structure, and properties of the superconducting compound series Bi<sub>2</sub>Sr<sub>2</sub>Ca<sub>n-1</sub>Cu<sub>n</sub>O<sub>y</sub> with n=1,2, and 3," *Physical Review B*, vol. 38, pp. 8885-8892, 1988.

- [137] H. Ota, *et al.*, "Formation of phase intergrowth in the syntheses of Bi-superconducting thin films," *Applied Physics Letters*, vol. 70, pp. 1471-1473, 1997.
- [138] J. S. Luo, *et al.*, "Phase chemistry and microstructure evolution in silver-clad  $(\text{Bi}_{2-x}\text{Pb}_x)\text{Sr}_2\text{Ca}_2\text{Cu}_3\text{O}_y$  wires," *IEEE Transactions on Applied Superconductivity*, vol. 3, pp. 972-975, 1993.
- [139] G. D. Gu, *et al.*, "Anisotropy of Bi-2212 superconducting crystals," *Superconductor Science and Technology*, vol. 11, p. 1115, 1998.
- [140] T. G. Holesinger, *et al.*, "Isothermal Melt Processing Of  $\text{Bi}_2\text{Sr}_2\text{CaCu}_2\text{O}_{-\gamma}$  Round Wire," *Physica C*, vol. 253, pp. 182-190, Oct 1995.
- [141] T. J. Detrie and K. H. Sandhage, "Fabrication of  $\text{Ag}/\text{Bi}_2\text{Sr}_2\text{CaCu}_2\text{O}_{8\pm x}$  superconducting tapes by the oxidation and postoxidation (partial melt) annealing of malleable, metal-bearing precursors," *Journal of Materials Research*, vol. 15, pp. 306-316, 2000.
- [142] D. Bourgault, *et al.*, "Misalignment angles and the 2D–3D temperature crossover in Bi2212 multifilaments studied using transport critical current densities," *Superconductor Science and Technology*, vol. 17, p. 463, 2004.

## Chapter 2

### **BI<sub>2</sub>SR<sub>2</sub>CACU<sub>2</sub>O<sub>x</sub> OXIDE PRECURSOR SYNTHESIS FROM NANO-OXIDES AND ITS EFFECTS ON MULTIFILAMENTARY WIRE TRANSPORT PROPERTIES**

Yun Zhang<sup>1</sup>, Stephen Johnson<sup>2</sup>, Manasi Chaubal<sup>2</sup>, Joey Stieha<sup>2</sup>, Ganesh Venugopal<sup>2</sup>, Andrew Hunt<sup>2</sup>, Justin Schwartz<sup>1</sup>

<sup>1</sup>Department of Material Science and Engineering, North Carolina State University, Raleigh, NC 27695, USA

<sup>2</sup>nGimat, LLC, 2436 Over Dr, Lexington, KY, 40511

#### **Abstract**

Bi<sub>2</sub>Sr<sub>2</sub>CaCu<sub>2</sub>O<sub>x</sub> (Bi2212)/Ag-alloy wires are manufactured via the oxide-powder-in-tube route by filling Ag/Ag-alloy tubes with Bi2212 oxide precursor, deforming into wire, restacking and heat treating using partial-melt processing. Recent studies propose several requirements on precursor properties, including stoichiometry, chemical homogeneity, carbon content and phase purity. Here, nanosize oxides produced by NanoSpray Combustion™ are used as starting materials to synthesize Bi2212 oxide precursors via solid-state calcination. Precursor powders with precisely controlled stoichiometry and chemical homogeneity containing over 99.1 vol% of Bi2212 single crystals are synthesized. Alkaline-earth cuprate (AEC) are found to be the only impurity phase in the precursor powders. Phase transformation, carbon release and grain growth during calcination are studied extensively through a series of quench studies. Effects of particle size, surface area, stoichiometry, chemical homogeneity and microstructures of the starting materials on Bi2212 formation and wire transport properties are discussed. Small particle size, high surface area and short diffusion length of the starting materials result in a rapid and homogeneous phase

transformation to Bi2212, along with an early and rapid carbon release. The residual carbon of the precursor powder is between 50-90 ppm. The strong dependence of transport  $J_c$  on precursor stoichiometry indicates that compositional variations within precursor powders should be less than 1.5 mol%. Two Bi-rich and Ca-deficient stoichiometries give higher wire transport critical current density, with the highest being 2520 A/mm<sup>2</sup> (4.2 K, 5 T) with an optimal PMP peak temperature of 889 °C. AEC particles smaller than the wire filament size are not considered to be a negative factor on wire performance, but as potential additional nucleation sites during solidification. The absence of Bi2201 grains in the precursor powders is preferred.

**Key words:** Bi-2212, superconductor, precursor, calcination, critical current density

## **Introduction**

Many future magnet applications for high energy physics and nuclear magnetic resonance require a superconducting conductor capable of generating magnetic fields above 30 T [1]. Low temperature superconductors, such as NbTi and Nb<sub>3</sub>Sn, can only generate magnetic fields up to 10.5 T and 20 T [2-4] due to their upper critical fields being less than 25 T at 4.2 K. Thus, high temperature superconductors, such as YBa<sub>2</sub>Cu<sub>3</sub>O<sub>7-x</sub> (YBCO) and Bi<sub>2</sub>Sr<sub>2</sub>CaCu<sub>2</sub>O<sub>x</sub> (Bi2212), with upper critical field greater than 100 T, are promising candidates [5-7]. As the only high field superconductor available as an isotropic round wire, Bi2212 Ag/Ag-alloy sheathed wires are of particular interest.

Currently, Bi2212/Ag wires are manufactured via the oxide-powder-in-tube route by filling Ag/Ag-alloy tubes with Bi2212 oxide precursor, deforming into wire, restacking (sometimes twice) and heat treating using partial-melt processing (PMP). During the partial-melt, Bi2212 powder melts incongruently, forming several non-superconducting crystalline phases and a

liquid phase, which cannot convert completely to Bi2212 during subsequent cooling. Non-superconducting impurities remain after solidification, including  $\text{Bi}_2\text{Sr}_2\text{CuO}_x$  (Bi2201), a copper-free (CF) phase and alkaline earth cuprates (AEC) [8, 9]. Furthermore, bubbles and voids form and evolve during PMP because of the low tap density of the green wire and carbon residue in the Bi2212 oxide precursor [10-16].

Many methods have been developed to produce Bi-Sr-Ca-Cu-oxide precursors. The solid-state route starts with raw materials such as oxides, carbonates, nitrates or hydroxides and goes through a series of calcination and pulverizing processes [17-20]. The final properties of Bi2212 powders, including phase assemblage, grain size and homogeneity, depend on the stoichiometry and particle size of the starting materials [21-23], calcination conditions [19] and the pulverizing process, such as grinding and ball milling. In previous studies, the common size of the starting material powders was in micrometers or larger, resulting in chemical inhomogeneities and incomplete carbon release and thus required a repetition of calcination and pulverizing processes. The liquid-phase route produces homogeneous and sub-micron size powders before calcination. Typical methods are spray pyrolysis [24, 25], co-precipitation [26, 27] and sol-gel [28], among which, spray pyrolysis [29] is the most promising because it allows precise control of the stoichiometry and produces homogeneous Bi2212 powders without pulverizing. Both co-precipitation and sol-gel require precise control of the solution pH value and solubility of the solvents to maintain the stoichiometry. Furthermore, ball milling is usually involved which can affect stoichiometry. Most recently, a metallic precursor route was developed for the synthesis of Bi2212 superconductor, which also aimed at controllable stoichiometry, homogeneity and low carbon content [30, 31].

There have been many studies focused on the optimization of PMP conditions for wires that vary the temperature, time and atmosphere to improve Bi2212 phase purity, grain connectivity and transport properties [32-35]. These studies propose requirements on stoichiometry, phase purity, homogeneity and carbon content of Bi2212 precursors in the green wire. Yet, far fewer studies have discussed the effect of precursor stoichiometry on wire performance [23, 36], and most of those either focused solely on the synthesis process and properties of Bi2212 bulk materials [24, 37-42] or studied precursor properties by comparing superconducting tapes/thick films that had varying methods, geometries and substrates [10, 19, 29, 43, 44].

Here, a method combining NanoSpray Combustion™ processing and solid-state calcination is used to synthesize Bi2212 oxide precursor. Characteristics of starting raw materials, calcination conditions and formation of Bi2212 phase are studied. Bi2212 precursors are analyzed extensively, including thermal, chemical, microstructural and magnetic characterization. Three batches of Bi2212 precursors are used to form multifilamentary wires of two configurations, and the relationships between precursor properties and wire performance are discussed.

## **Experimental approach**

### *Powder synthesis*

The starting raw materials, referred to as “as-made” powders, are metal oxides produced via NanoSpray Combustion™ processing; details of this process are found elsewhere [45]. Three nominal cation stoichiometries are chosen for this study:  $\text{Bi}_{2.26}\text{Sr}_{1.90}\text{Ca}_{0.90}\text{Cu}_{1.98}\text{O}_x$  (Batch-I),  $\text{Bi}_{2.15}\text{Sr}_{1.89}\text{Ca}_{0.93}\text{Cu}_{1.95}\text{O}_x$  (Batch-II) and  $\text{Bi}_{2.26}\text{Sr}_{1.89}\text{Ca}_{0.86}\text{Cu}_{1.99}\text{O}_x$  (Batch-III). As-made powders are calcined in solid-state in 1 bar flowing oxygen to form the Bi2212 phase.

The alumina crucible used is lined with Ag foil (0.28 mm in thickness) to avoid reaction between powders and the crucible.

A series of quench studies is performed to investigate the phase transformations during calcination. The powders are quenched to room temperature after holding at calcination temperature ( $T_{\text{calcination}}$ ) for 10 min-72 hrs. After obtaining the required time to convert as-made powders to high-purity Bi2212 powders, a full heat treatment is carried out by holding the as-made powder at  $T_{\text{calcination}}$  for 72 hrs and then cooling to room temperature with different rates. Batches I and II were cooled initially at a slow rate of 6 °C/hr from  $T_{\text{calcination}}$  to 800 °C, at a fast rate of 750 °C/hr to 700 °C and finally at an intermediate rate of 260 °C/hr from 700 °C to room temperature. Batch III was cooled initially at an intermediate rate of 300 °C/hr from  $T_{\text{calcination}}$  to 800 °C and then at a slow rate of 90 °C/hr from 800 °C to room temperature. Each fully heat treated batch, referred to as “precursor powder”, is used to make a multifilamentary Bi2212/Ag/AgAl wire.

#### *Wire processing*

Three double-restack multifilamentary Bi2212/Ag/AgAl round wires are manufactured by Supramagnetics, Inc., via the powder-in-tube method with each precursor powder batch as described above. The Batch I and Batch II green wires consist of 259 filaments in a 37 x 7 configuration with a fill factor of 15.0%. Batch III green wire consists of 637 filaments in a 91 x 7 configuration with a fill factor of 12%. Each wire has a 0.81 mm outer diameter. Optical images of Batch II and Batch III green wires are shown in Figure 2-1. The filaments are in a pure Ag matrix contained within a Ag-0.1 wt% Al alloy outer sheath. The average filament size in both Batch I and Batch II green wires is 30 µm whereas in Batch III wire the average filament size is 14 µm.

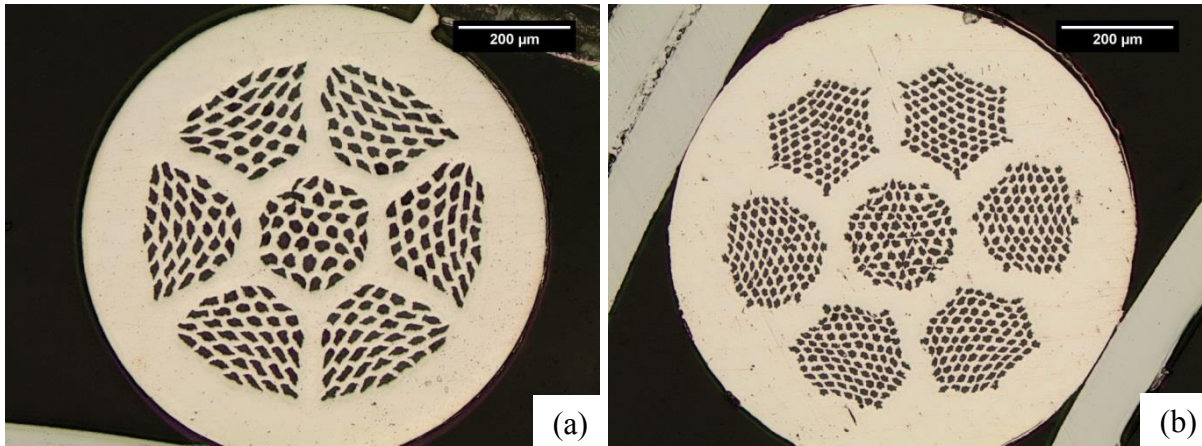


Figure 2-1 Optical microscope images of green wire cross-sections

(a) Batch II and (b) Batch III

Heat treatments on wires are performed on 5 cm long strands in 1 bar flowing oxygen in a horizontal quartz tube. Internal oxidation heat treatments are carried out before PMP. PMP peak temperatures range from 887 °C to 893 °C. Detailed heat treatment profiles are illustrated in Figure 2-2.

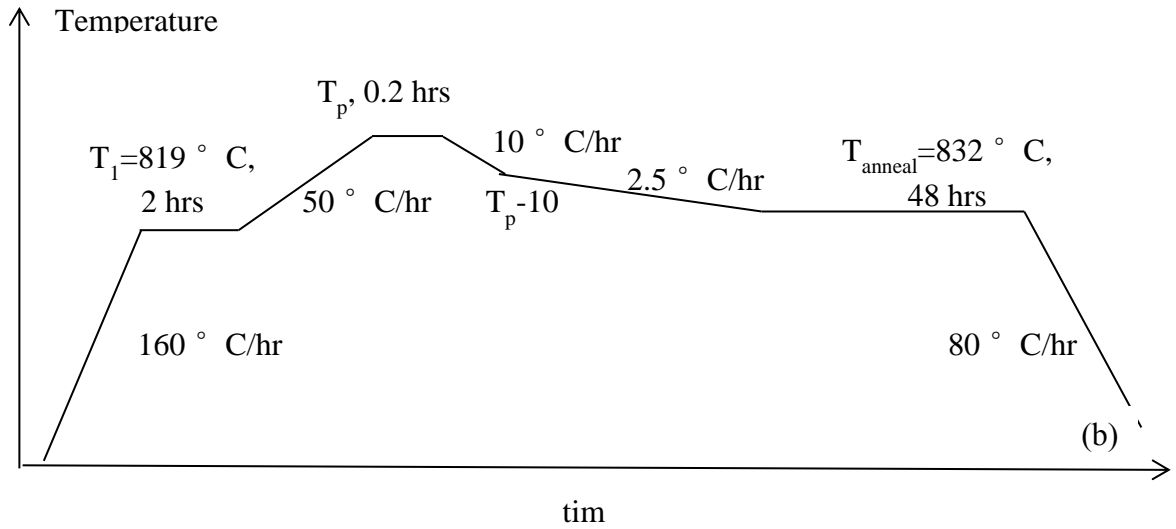
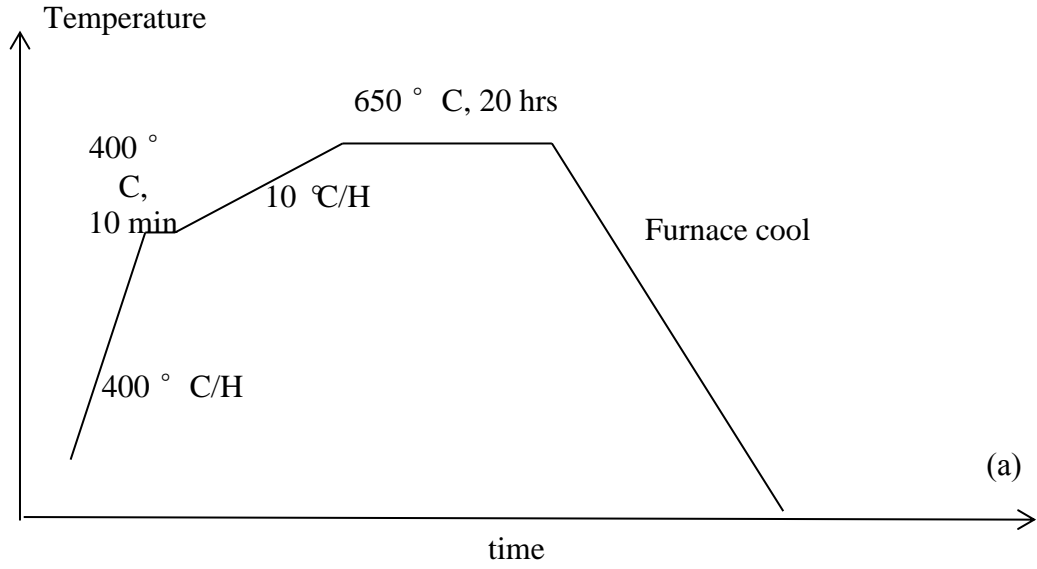


Figure 2-2 Heat treatment profiles for (a) internal oxidation and (b) PMP.

### *Characterization*

X-ray fluorescence (XRF) (SEA 2110 Element Monitor) is used to determine the stoichiometry and homogeneity of the three as-made powders. The reported values are an average of three measurements, and the standard deviations are calculated as the difference between each measurement and the average stoichiometry. Particle size and surface area analysis on as-made powders are carried out using the Brunauer–Emmett–Teller (BET) method (NOVA 2000e Surface Area and Pore Size Analyzer).

A carbon sensor (Viasensor G150) is instrumented on the gas outlet of the quartz furnace to measure the carbon dioxide release during powder calcination. A Leco CS230 is also used to measure the residue carbon content of precursor powders after calcination.

A Rigaku Smartlab X-ray diffractometer (XRD) is used for phase analysis on powders. The measurements are carried out with a  $\text{CuK}\alpha$  source over a  $2\theta$  range of  $5^\circ$ – $75^\circ$ , using 40 kV and 44 mA. The step size is  $0.04^\circ$  and the scan rate is 5 s/step. A Hitachi TM3000 scanning electron microscope (SEM), JOEL 6010LA SEM and energy dispersive spectrometry (EDS) are used to examine the minor impurity phases. Square pellets with side-length of 10 mm are made with precursor powders for impurity analysis. The volume fraction of impurities is calculated by image analysis on several backscattered electron images.

A FEI Quanta 3D FEG SEM, a JEOL 2000FX Scanning Transmission Electron Microscope (STEM) and a FEI Titan 80-300 probe aberration corrected scanning transmission electron microscope (STEM) with SUPER X EDS are used to investigate the crystal structures and microstructures of powders. For SEM samples, the powders are placed on a carbon tape with a spatula. For TEM and STEM samples, both as-made powders and ground precursor powders are dispersed in ethanol and dried on a Mo grid with a carbon film.

Magnetic properties are measured in a SQUID magnetometer (Quantum Design MPMS-5S) via magnetization versus temperature measurements. The samples are cooled to 4.2 K in zero field and measured in a 100 Oe applied field during warming to 95 K.

Differential thermal analysis (DTA) (Perkin Elmer STA 6000) is used to study the melting behavior of the three green wires after internal oxidation heat treatments. The samples are heated to 940 °C at 5 °C/min in 1 bar flowing oxygen (20 ml/min). All samples are 40 mg ± 5 mg. The onset of melting is determined using the intersection of the baseline and the tangent line to the steepest slope.

Critical current ( $I_c$ ) is measured using the four-point-probe method in liquid helium (4.2 K) with applied fields of 0 T and 5 T. A 1 µV/cm electric-field criterion, with 20 mm voltage tap spacing, is used to determine  $I_c$ . Critical current density ( $J_c$ ) is calculated by dividing  $I_c$  by the multiplier of the cross-sectional area and fill factor of the green wire.

## Results

### *As-made powders*

Table 2-1 summarizes the characteristics of the three batches of as-made powders. The differences between average values measured by XRF and nominal values show that the stoichiometries are precisely controlled within 1 mol% by NanoSpray Combustion™ processing. The standard deviation indicates the chemical homogeneity of each batch, showing that Batch I is measured as having less difference than Batches II and III. The average surface areas range from 9-14 m<sup>2</sup>/g, and the average particle diameter in nanometers is then calculated using

$$\text{average diameter} = \frac{6000}{S_{BET} \left( \text{in } \frac{\text{m}^2}{\text{g}} \right) \times \text{density} \left( \text{in } \frac{\text{g}}{\text{cm}^3} \right)};$$

a density of 6.4 g/cm<sup>3</sup> is used. The calculated particle sizes range from 67-104 nm.

Table 2-1 Characteristics of as-made powders

Characteristic	Batch I				Batch II				Batch III			
	Bi	Sr	Ca	Cu	Bi	Sr	Ca	Cu	Bi	Sr	Ca	Cu
Nominal stoichiometry	2.26	1.90	0.90	1.98	2.15	1.89	0.93	1.95	2.26	1.89	0.86	1.99
Measured stoichiometry	2.25	1.89	0.89	1.97	2.18	1.91	0.94	1.97	2.28	1.88	0.90	1.95
Standard deviation (mol%)	0.4				2.9				1.5			
Surface area $S_{\text{BET}}$ ( $\text{m}^2/\text{g}$ )	12±2				14±2				9±2			
Particle size (nm)	80±10				67±10				104±10			

Figure 2-3 shows a TEM image of the Batch II as-made powder. The as-made powder mostly consists of fine spherical to polyhedral particles with an average size of 51 nm. The difference between the calculated value from BET surface area and the TEM image is due to agglomeration or strongly absorbed surface gasses of the as-made powder during BET surface area measurement, where a small amount of surface was lost. Powders for Batch I and III show similar results.

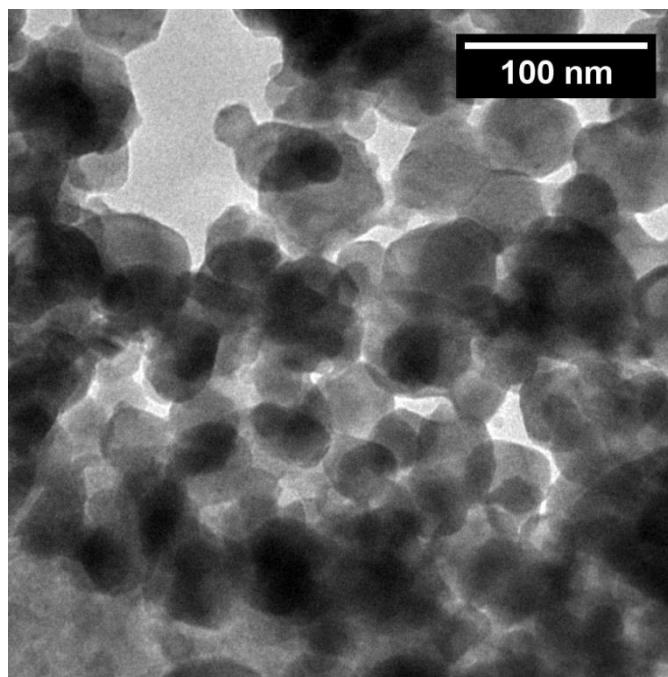


Figure 2-3 Bright field TEM image of Batch II as-made powder.

Figure 2-4 shows the XRD pattern of Batch II as-made powders. The as-made powder, before calcination, is a mixture of amorphous material and several oxides, including CuO, Ca-Bi-oxide, Bi-Sr-oxide and Bi2201. The peak broadening is due to the small particle size.

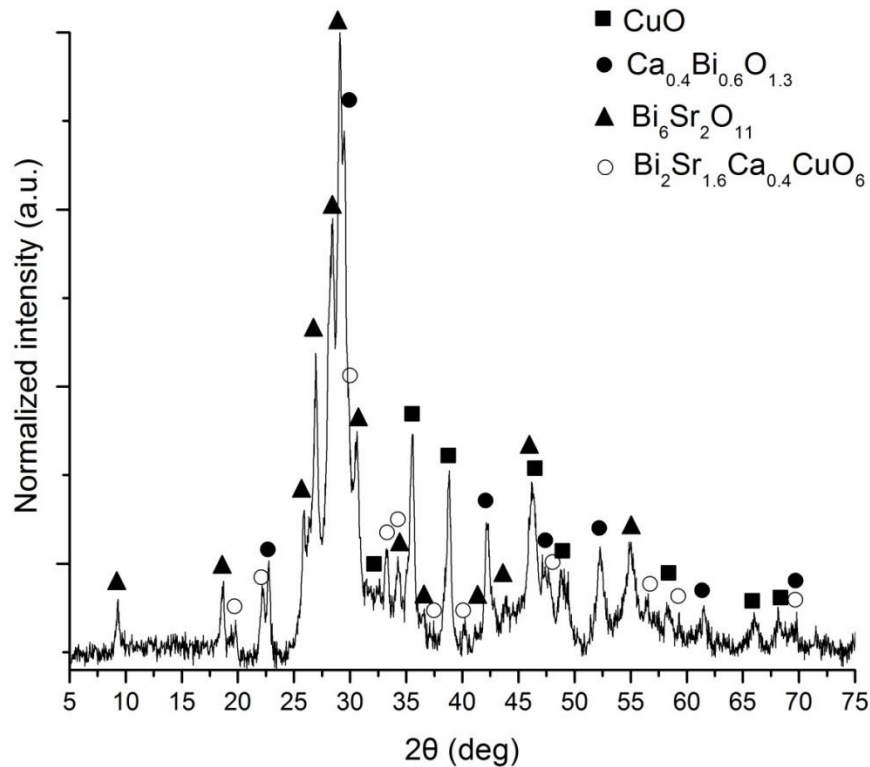
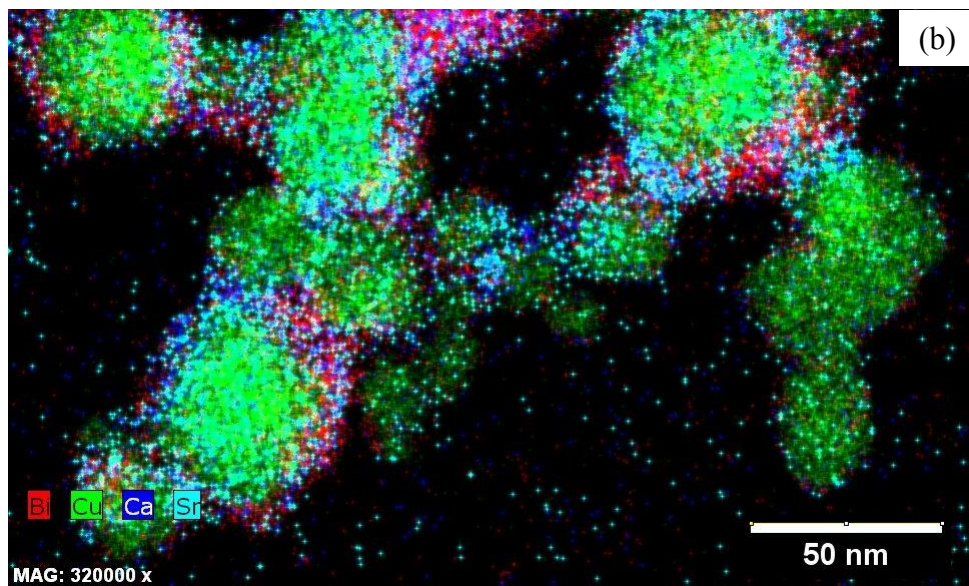
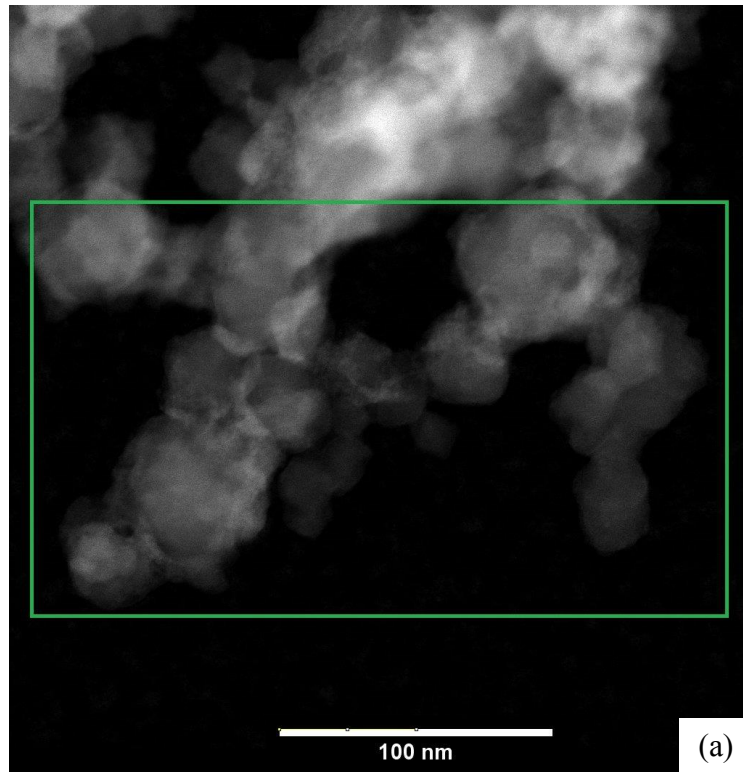
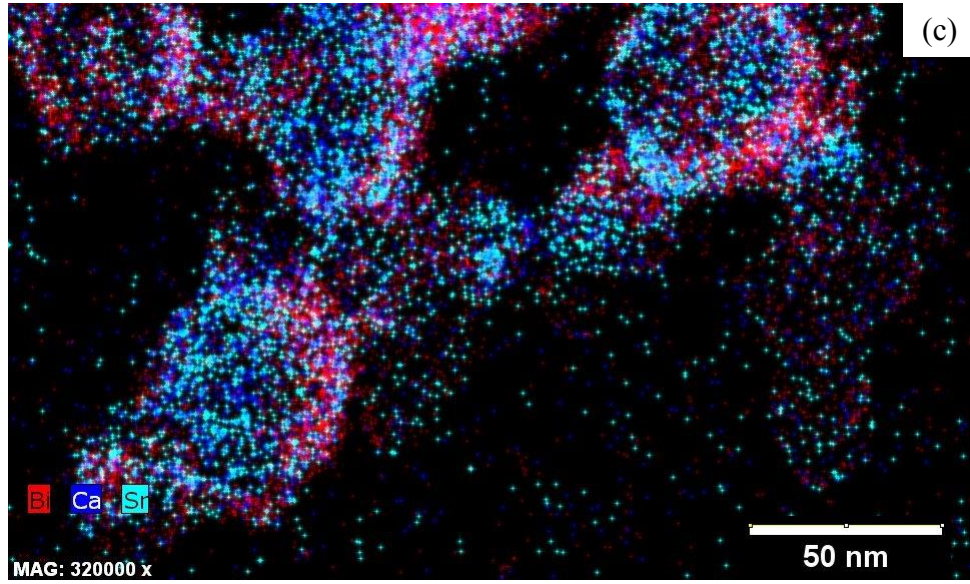


Figure 2-4 XRD pattern of Batch II as-made powder.

Figure 2-5 shows a high-angle annular dark field (HAADF) STEM image of Batch II as-made powder and the corresponding EDS maps of a selected area. EDS maps show that the spherical CuO particles are much larger than other oxides. Comparing EDS maps in (b) with Cu and (c) without Cu, a structure similar to a nanocomposite is observed. Oxides other than CuO are deposited onto the CuO particle surfaces in a layer that is ~10 nm thick.

Figure 2-5 (a) HAADF-STEM image of Batch II as-made powder (b) and (c) show corresponding EDS maps of the selected area.





*Phase transformations during calcination*

Figure 2-6 shows the XRD patterns of a series of quenched Batch II powders. Due to the extensive peak overlap, the peaks that only belong to a specific phase are marked by arrows on each pattern. Bi2212 forms after 10 min calcination. Several other phases also form at this point, including SrO, Sr<sub>2</sub>CuO<sub>3.24</sub> and Bi<sub>2</sub>O<sub>3</sub>, indicating complicated reactions occur during heating. Starting from a mixture of oxides, subsequent reactions between these oxides and intermediate compounds take place with increasing calcination time. The Bi2201, Bi<sub>2</sub>O<sub>3</sub> and SrO peaks diminish after a 36-hr calcination, and a 72-hr calcination further reduces the Sr<sub>2</sub>CuO<sub>3.24</sub> content below the XRD detection limit.

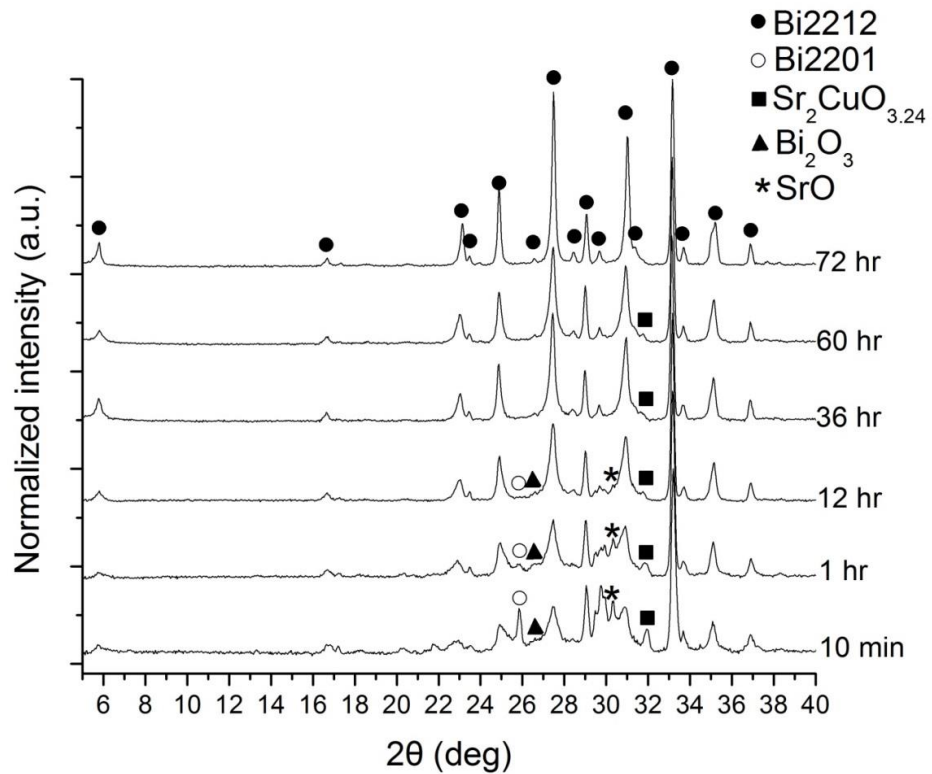


Figure 2-6 XRD patterns of Batch II powders quenched from T<sub>calcination</sub>.

Figure 2-7 shows the SEM images of quenched Batch II powders after calcinations of 10 min, 1 hr, 12 hrs and 72 hrs. After a 10-min calcination, thin Bi2212 grains of 1-2  $\mu\text{m}$  are observed, and small particles of other unreacted phases are also seen. After a 1-hr calcination, the size of Bi2212 grains increases to 3-4  $\mu\text{m}$ , and the amount of unreacted particles is reduced. After 12-hr and 72-hr calcinations, 3-7  $\mu\text{m}$  Bi2212 grains are observed, and the thickness increases. But from 12 hrs to 72 hrs the changes in grain size and morphology are subtle.

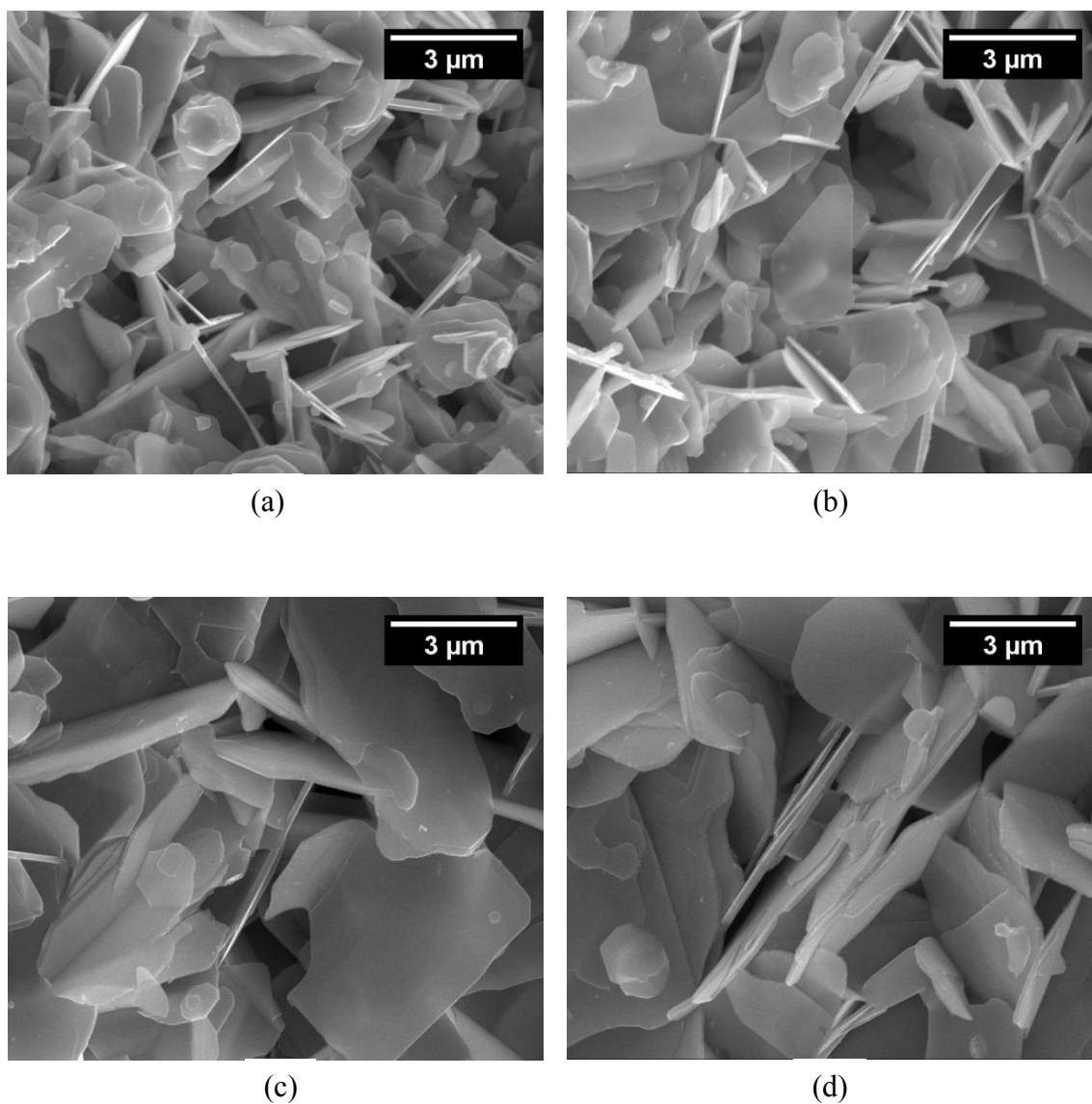


Figure 2-7 SEM images of quenched Batch II powders after (a) 10 min (b) 1 hr (c) 12 hr and (d) 72 hr calcination.

Figure 2-8 shows magnetization results of quenched Batch II powder. With increasing calcination time, the magnetic moment at 4.2 K increases due to increased Bi2212 phase purity and grain size. In Figure 2-8b, the same data is normalized to reference values at 4.2 K to show more clearly the superconducting transition at the critical temperature,  $T_c$ . All

quenched powders show a single transition in the temperature range of 78-82 K with a transition width from 6 K to 10 K. In general, as the calcination time increases,  $T_c$  increases and transition width decreases.

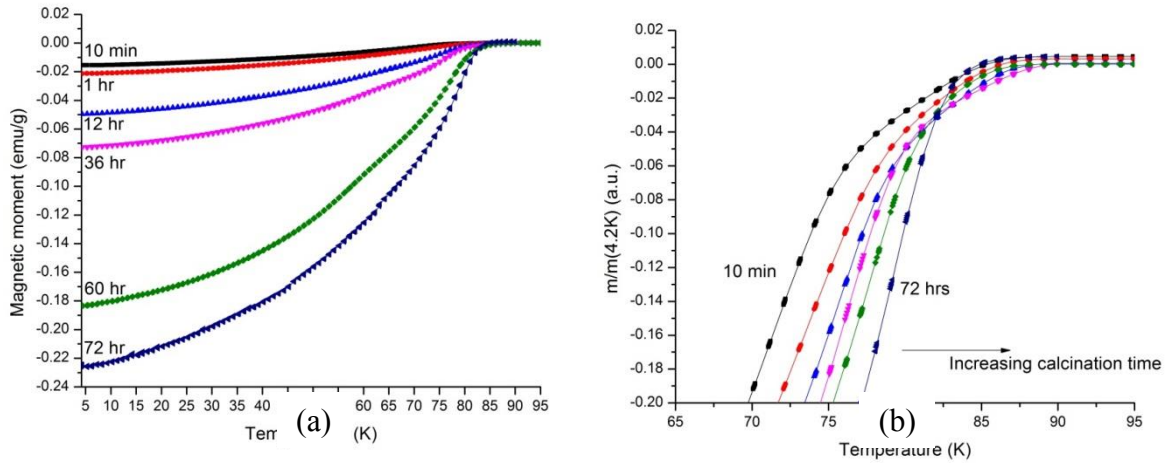


Figure 2-8 (a) Magnetization and (b) normalized magnetization versus temperature for quenched Batch II powders.

#### *Precursor powder and wire performance*

Figure 2-9 shows the  $CO_2$  release during the full calcination of Batch II precursor powder.  $CO_2$  release begins well below 600 °C and is complete before reaching the maximum temperature. There is no further measurable release during the 72-hr hold at  $T_{calcination}$  and subsequent furnace cooling stages. The residual carbon contents of all precursor powders are shown in Table 2-2; all are below 100 ppm.

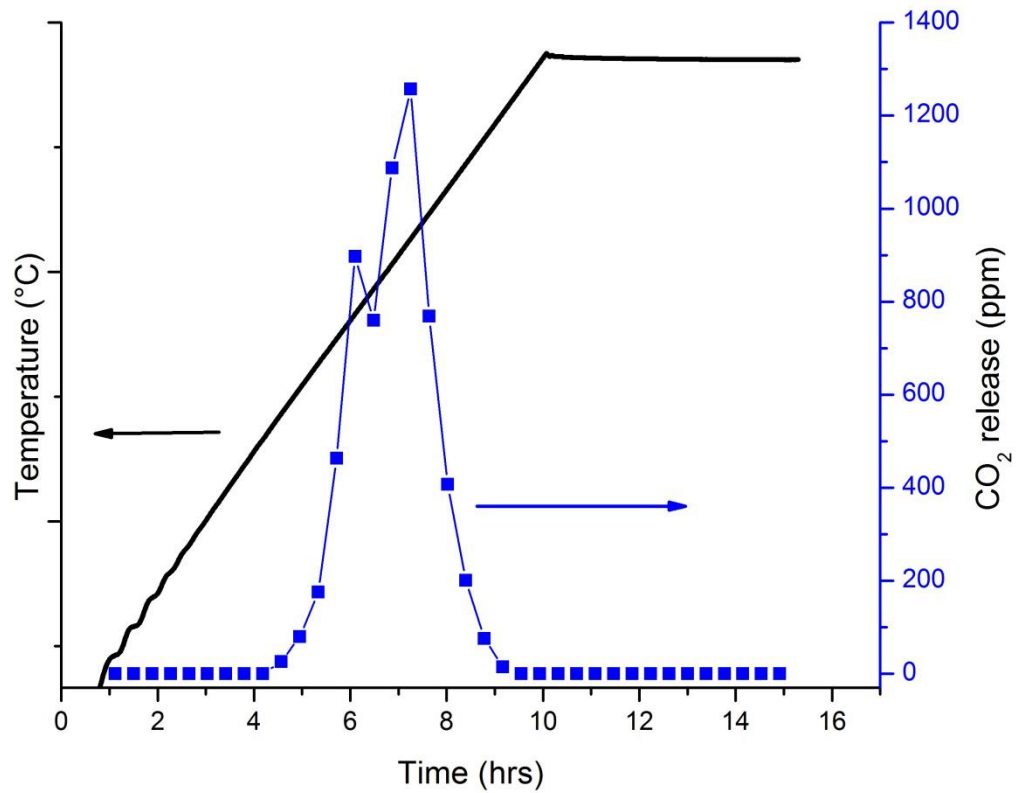


Figure 2-9 CO<sub>2</sub> release versus time and temperature during the calcination of Batch II precursor powder.

Table 2-2 Characteristics of precursor powders

Characteristic	Batch I	Batch II	Batch III
Residue carbon (ppm)	60	90	50
AEC vol%	0.29	0.03	0.86
AEC particle size (µm)	2-11	3-5	4-9

Figure 2-10 shows the XRD pattern of precursor powders from each batch, with the majority peaks of the Bi<sub>2</sub>2<sub>1</sub>2 phase indexed. Only Bi<sub>2</sub>2<sub>1</sub>2 peaks are observed for all batches, indicating at least 95 vol% pure Bi<sub>2</sub>2<sub>1</sub>2 content. Figure 2-11 shows SEM images of Batch II precursor powder. The precursor powder consists of soft agglomerations of Bi<sub>2</sub>2<sub>1</sub>2 grains which break readily via weak mechanical forces with a spatula. The primary particles are 3-7 μm Bi<sub>2</sub>2<sub>1</sub>2 grains, similar to that of powder quenched after a 72-hr calcination, indicating that there is little grain growth during the cooling stage. Figure 2-12 shows an SEM image of a polished pellet made with Batch III precursor powder. Dark particles marked by circles are AEC phases as identified by EDS. Image analysis is used to quantify the size and volume content of the AEC phases; the results are summarized in Table 2-2. The Bi<sub>2</sub>2<sub>1</sub>2 phase purity of all the precursor powders is at least 99 vol%. Batch III contains highest content of AEC phases and Batch II contains the lowest AEC content, smallest AEC particles and the narrowest AEC particle size distribution.

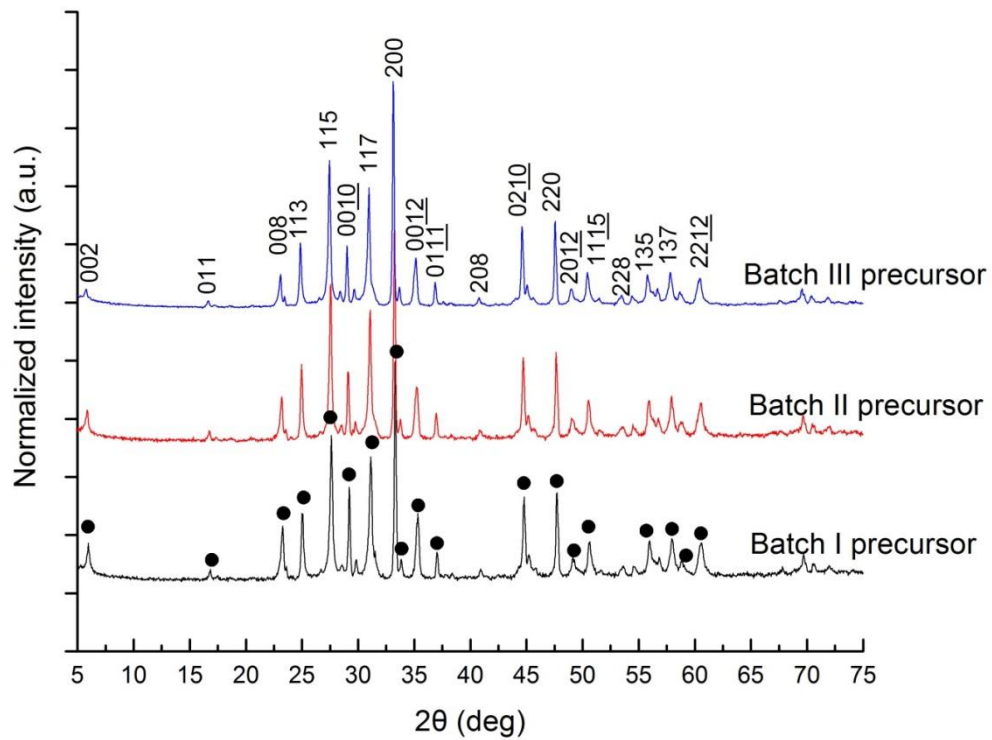


Figure 2-10 XRD results for the three precursor powders with the major peaks indexed.

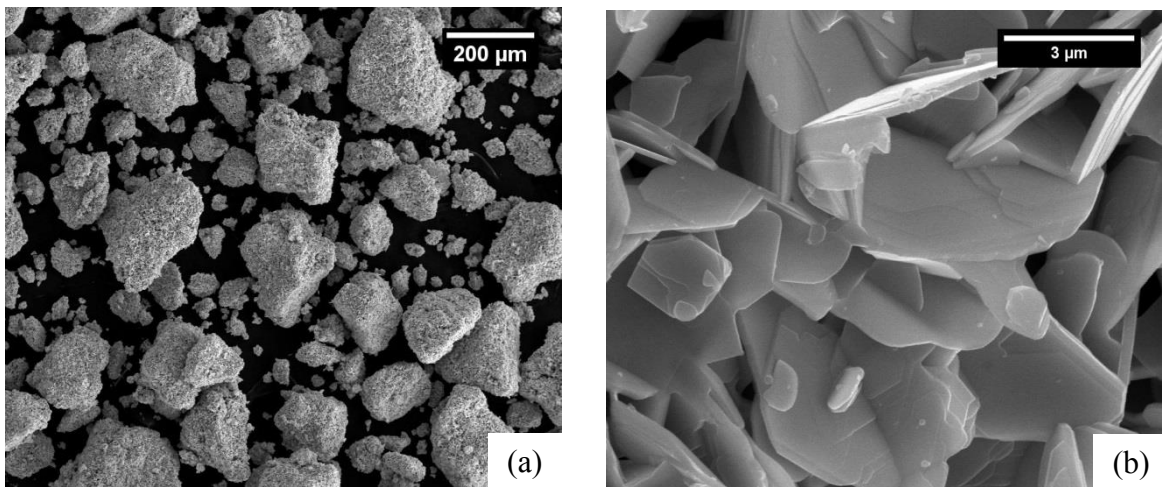


Figure 2-11 SEM images of Batch II precursor powder showing (a) soft agglomerates of Bi2212 grains and (b) morphology of individual Bi2212 grains.

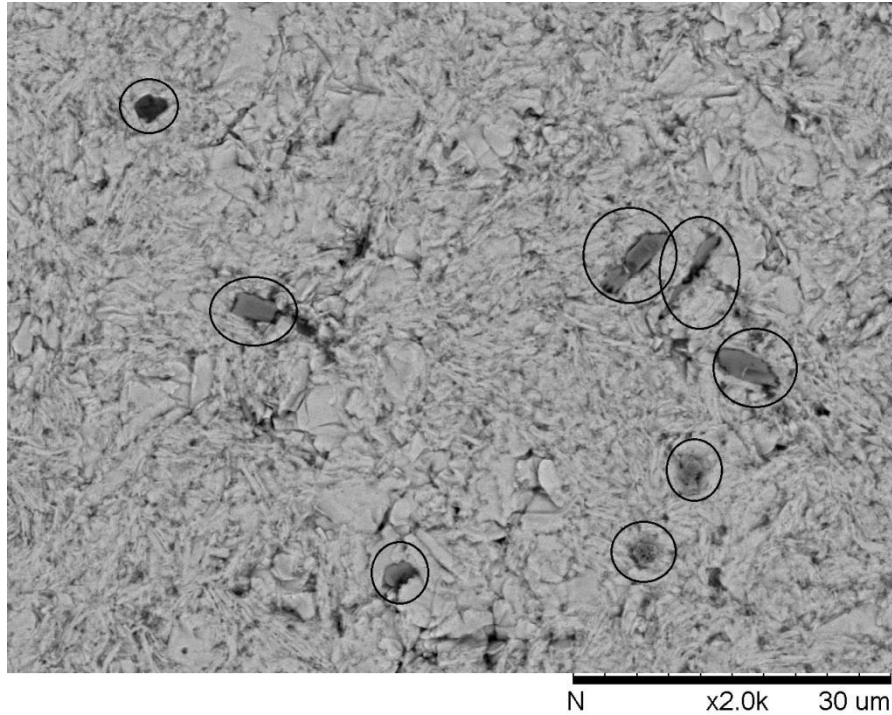


Figure 2-12 SEM image of Batch III precursor powder pellet with AEC particles indicated by circles.

Figure 2-13 shows a TEM image of a single Bi2212 grain from Batch II precursor powder and the corresponding [001] zone-axis diffraction pattern. Note that the precursor powder was ground to be transparent to the electron beam and dispersed in ethanol, and thus the particle size is much smaller than measured from SEM images. The diffraction pattern indicates that the grain is a Bi2212 single crystal, with an a-axis of 5.19 Å and a b-axis of 5.41 Å. Structural modulations are observed by satellite reflections along the b-axis.

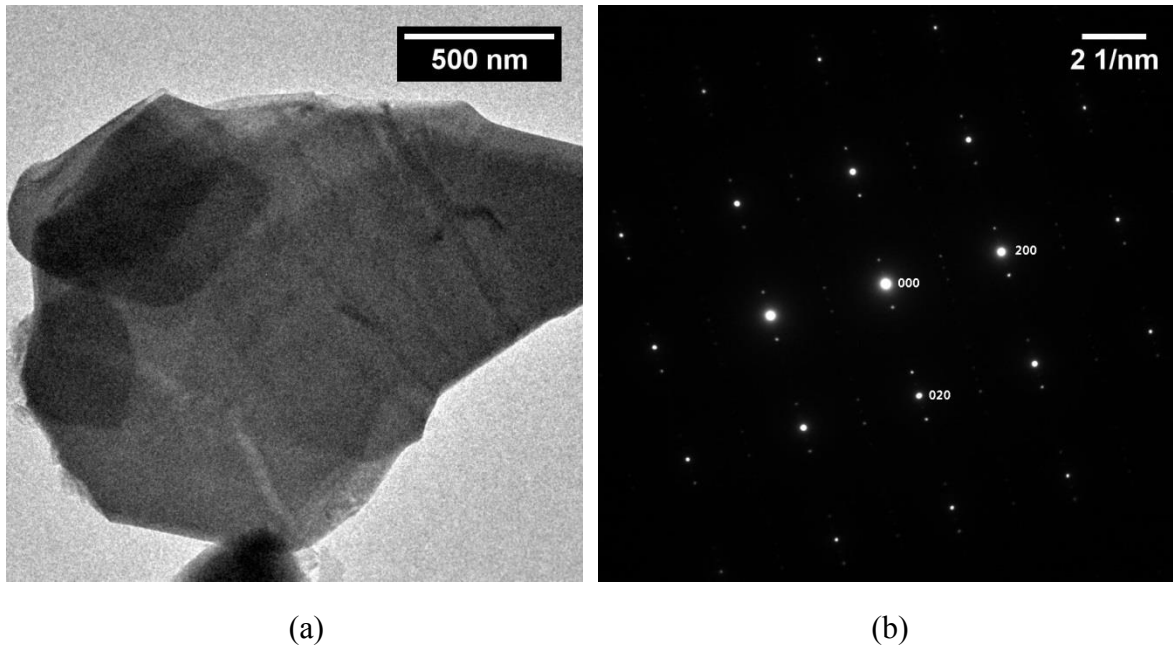


Figure 2-13 (a) TEM image of Batch II precursor powder and (b) a [001]-zone axis diffraction pattern.

Figure 2-14 shows the magnetization versus temperature for all precursor powders; clear differences are seen. Batch III shows the largest magnetic moment at 4.2 K, by about 50%, with that of Batch I about 10% stronger than Batch II. Note that the magnetic moments of all precursor powders are higher than those of the quenched powder after a 72-hr calcination, indicating that the residue impurity phases continue to convert to Bi2212 during the furnace cooling stage. Both Batch I and Batch II show a two-step transition, which is likely the result of inhomogeneous oxygen content in the Bi2212 grains. A common onset  $T_c$  of 87 K is observed for Batches I and II, but the second transition occurs at different temperatures, 74 K and 67 K, respectively. Batch III shows one smooth transition with an onset at 85 K.

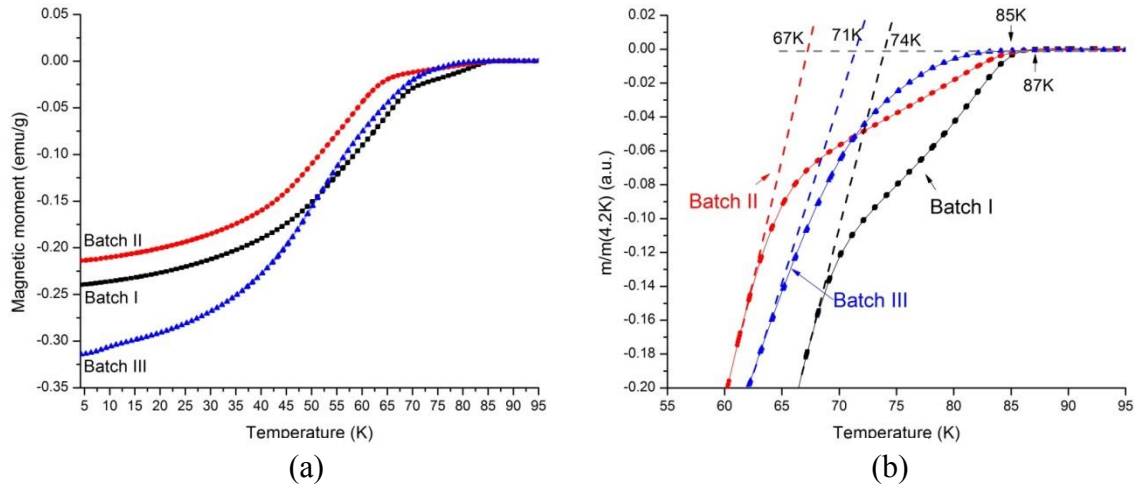


Figure 2-14 (a) Magnetization and (b) normalized magnetization versus temperature for precursor powders.

Figure 2-15 shows the melting behaviors of the three green wires after internal oxidation heat treatments. Batch II green wire shows a melting onset at a lower temperature than the other two batches and with a broader endothermic peak. This behavior suggests larger compositional inhomogeneity in Batch II green wire than the other two batches.

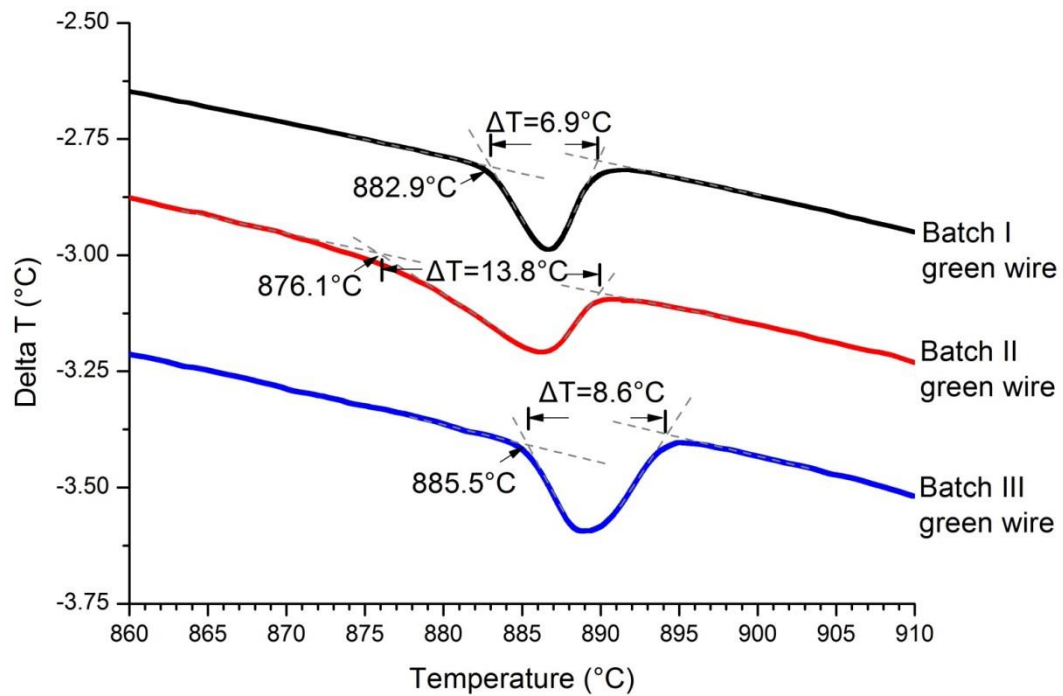


Figure 2-15 DTA curves of the green wires in pure, flowing oxygen after dispersion strengthening heat treatment.

Figure 2-16 shows the wire transport behavior after PMP as a function of peak temperature. The highest  $J_c$  (4.2 K, 5 T) obtained was 2520 A/mm<sup>2</sup> in Batch III wire. The window for peak temperature for less than a 20%  $J_c$  degradation for each wire is between 2 °C-3 °C.

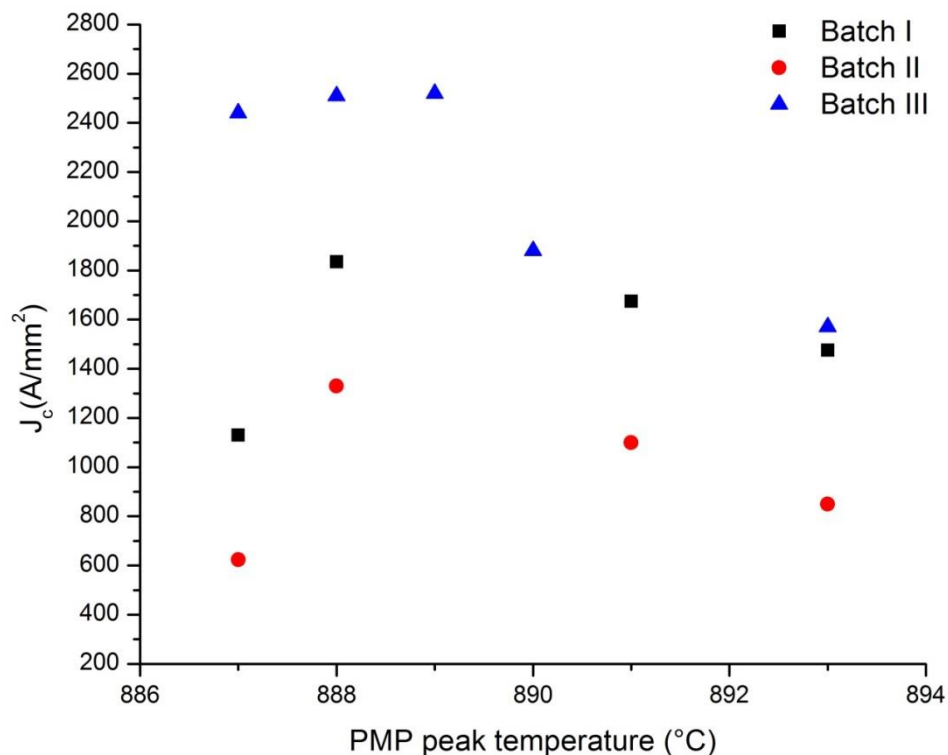


Figure 2-16 Transport  $J_c$  (4.2 K, 5 T) vs PMP peak temperature.

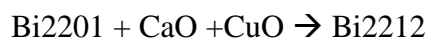
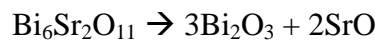
## Discussion

### *Calcination and phase transformations*

The XRD results of as-made and quenched powders show that, with sufficient calcination time, over 99 vol% of the metal oxides are reacted and converted to high-purity Bi2212 powder. The narrow particle size distribution of the precursor powders indicates that no liquid phase formed during calcinations. Previous studies show that a liquid phase during calcination impacts the phase content and microstructure of the calcined powder. On the one hand, without the aid of liquid, starting oxides/carbonates cannot be converted completely if they have poor homogeneity, i.e., in a large batch or with a large particle size [20]. This is

due to greatly suppressed cation diffusion over a long length scale. On the other hand, liquid formation can reduce the overall homogeneity of the calcined powder because a large amount of impurity phases with large particle sizes can form during partial-melt [19]. Excessive and uncontrolled grain growth was also observed with the presence of liquid [19]. Here, starting with nano-size oxides, the phase transformation to Bi2212 is thorough and fast due to the substantially smaller particle size and larger surface area. Based on BET theory, the surface area is inversely proportional to particle size and small particle size greatly increase the reactivity and rate of phase transformation [21]. Furthermore, small particle size significantly decreases phase segregation in the as-made powders over a long length scale and thus repeated pulverizations and calcinations are not needed to achieve high-purity Bi2212 precursors. Also, synergetic chemical reactions are expected due to the microstructure where the diffusion lengths between the outer oxide layer and the interior CuO particle are on the nano scale.

Here, the phase transformation pathway from as-made powders to Bi2212 precursor powders is similar to but more complicated than previous studies since several oxides consist of more than one metal ion [19, 20, 42, 46]. By analyzing the phase assemblage of as-made and quenched powders, the following chemical reactions are expected:



Before reaching  $T_{\text{calcination}}$ ,  $\text{Ca}_{0.4}\text{Bi}_{0.6}\text{O}_{1.3}$  and  $\text{Bi}_6\text{Sr}_2\text{O}_{11}$  decompose into  $\text{Bi}_2\text{O}_3$ ,  $\text{CaO}$  and  $\text{SrO}$ . After a 10-min calcination, some  $\text{Bi}_2\text{O}_3$  reacts with  $\text{CaO}$  and  $\text{CuO}$  to form  $\text{Bi}_2\text{O}_3\text{Ca}$ , and in the meantime,  $\text{Sr}_2\text{CuO}_3$  forms by a reaction between  $\text{SrO}$  and  $\text{CuO}$ . The  $\text{Sr}_2\text{CuO}_3$  then reacts with  $\text{Bi}_2\text{O}_3$  to form  $\text{Bi}_2\text{O}_3\text{Sr}$ . With increasing calcination time,  $\text{Bi}_2\text{O}_3$ ,  $\text{CaO}$  and  $\text{CuO}$  continue to convert to  $\text{Bi}_2\text{O}_3\text{Ca}$  while residual  $\text{Sr}_2\text{CuO}_3$  decomposes as  $\text{CuO}$  is consumed. After a 36-hr calcination,  $\text{Bi}_2\text{O}_3$ ,  $\text{Bi}_2\text{O}_3\text{Sr}$  and  $\text{SrO}$  are no longer detected by XRD and after an additional 24-36 hrs, the  $\text{Sr}_2\text{CuO}_3$  content is also below the XRD detection limit. As the  $\text{Bi}_2\text{O}_3\text{Ca}$  single phase region covers a wide range of cation stoichiometry, cation substitution and non-stoichiometric reactions should also be expected during calcinations [47]. Furthermore, image analysis and EDS show that the only impurity phase in each fully calcined precursor powder is the AEC (2,1) phase, which is a product of reactions between  $\text{Sr}_2\text{CuO}_3$  and  $\text{CaO}$ . The volume content of the AEC phase in all three batches is less than 1 vol%, which is low compared with previous results [39].

Microstructure analysis of quenched powders shows the grain growth and morphology changes during calcinations. The  $\text{Bi}_2\text{O}_3\text{Ca}$  grains grow rapidly from 10 min to 12 hrs with the average grain size tripled. This is also consistent with the rapid conversion from  $\text{Bi}_2\text{O}_3\text{Sr}$  to  $\text{Bi}_2\text{O}_3\text{Ca}$  during this period. After a 12-hr calcination, the grain growth is suppressed because only minor reactions are taking place after complete consumption of  $\text{Bi}_2\text{O}_3\text{Sr}$ . In addition, during furnace cooling, changes in  $\text{Bi}_2\text{O}_3\text{Ca}$  grain size and morphology are subtle.

Magnetization results of quenched powders show that both  $\text{Bi}_2\text{O}_3\text{Ca}$  grain growth and increasing phase purity result in increasing magnetization and decreasing transition width. Magnetization results of fully calcined precursor powders show the effect of cooling rate on oxygen homogeneity and thus the transition as well. The transition widths of quenched

powders are narrower than precursor powders due to very fast cooling during quenching ( $> 4000 \text{ }^\circ\text{C/hr}$ ). There is no oxygen redistribution during quenching and thus a sharp  $T_c$  transition is observed. In precursor powders, a second transition was observed in both I and II. A single but relatively broad transition was observed in III.  $T_c$  is a function of annealing temperature, and can be changed by as much as 17 K if powders are annealed between 750-850  $^\circ\text{C}$  [48, 49]. The second transitions in Batch I and II precursor powder result from significantly different cooling rates between 800  $^\circ\text{C}$  and 700  $^\circ\text{C}$ , which results in an inhomogeneous oxygen distribution. Batch III precursor powder, however, has a continuous transition from 85 K to 71 K rather than two abrupt ones due to the intermediate to slow cooling between 800  $^\circ\text{C}$  to room temperature, which allows oxygen redistribution during cooling stage.

#### *Stoichiometry: control and effects*

Comparing nominal and average stoichiometries shows that the non-stoichiometry of each as-made powder is controlled within 0.6 mol% or less, which is much narrower than previous studies [50]. The precursor powder stoichiometry impacts the melting behavior, phase assemblage and thus transport  $J_c$  of PMP wires [19, 36, 51, 52]. Here, transport  $J_c$  of Batch I and III wires are 37%-88% higher than Batch II wires for each PMP peak temperature. Based on XRF results, Batch I and Batch III precursor powders are about 0.7 mol% Ca-deficient and 1.4 mol% Bi-rich compared with Batch II powder, though all precursor powders are of similar Bi2212 phase purity. XRF variation of the same powder over many samplings and days is on the order of  $\sim 5\%$  on each subscript. According to previous studies, the Bi2212 single phase region extends to a Bi-rich region and a slightly Ca-deficient composition

results in high transport  $J_c$  [47, 51]. Precursor stoichiometries with reduced Ca and increased Bi result in increased Bi2212 during resolidification during PMP.

*Chemical homogeneity: control and effects*

Another important property of Bi2212 precursor is the chemical homogeneity within each batch. All standard deviations in stoichiometry reported here are much lower compared to previous studies [19, 22, 39, 50]. One reason is that during NanoSpray Combustion<sup>TM</sup> processing, the metal ions are homogeneously mixed at the atomic level. Vapor species containing gaseous atoms, ions and molecular-oxide species condense to form atomic clusters and then coalesce to form nano-size oxides [45]. Furthermore, the solution droplets that go through the NanoSpray Combustion<sup>TM</sup> processing are much smaller in size, compared to conventional spray pyrolysis and oxide-carbonate mixtures by mechanical milling [45]. This leads to a more homogeneous elemental distribution in as-made powders compared to other methods. The nanocomposite microstructure of the as-made powders also contribute to increased homogeneity. The unique particle assemblage of the as-made powders results from the interparticle collisions and fusion during combustion [53], which is different from randomly distributed oxide particles via conventional methods. Here, the CuO particles are surrounded by a nano-size layer of other oxides. Thus, the high surface area and ultra-short diffusion length between these oxides result in synergetic chemical reactions during calcination.

The strong dependence of transport  $J_c$  on precursor stoichiometry also indicates that the variation within each precursor batch should be below 1.5 mol%. This explains the different melting behavior between the three batches of green wire. The shallow transition at 876.1 °C and the broadened melting peak for Batch II wire indicate inhomogeneous melt. Since each

precursor powder is of similar Bi2212 phase purity, the shallow transition is a result of chemical inhomogeneity and multiple melting. For Bi2212 wire processing, uniform melting behavior along the entire wire length is crucial to transport properties as phase assemblage and segregation are sensitive to the PMP peak temperature [36, 54, 55]. For Batch II wire, the precursor powder melts non-uniformly along the wire length at each PMP peak temperature. Consequently, during subsequent solidification, excessive phase segregation is expected, reducing the transport  $J_c$  and increasing the reduction of  $J_c$  versus peak temperatures.

#### *Carbon content*

Residual carbon content is another concern for Bi2212 oxide processing. Carbon residue in the powder can cause severe porosity in the wire filaments during PMP, significantly reducing transport  $J_c$  [10, 11, 16]. Here, an early and rapid release of  $\text{CO}_2$  during calcination is observed. The carbon release begins at a temperature about 300 °C lower than via a conventional mix of carbonate-oxides and 70 °C lower than via metallo-organic precursors [56]. Carbon release is complete before the calcination temperature is reached, eliminating the reaction between carbon and several oxides during Bi2212 formation. Unlike previous studies, due to the high surface area and atomic level mixing of the as-made powder, the residual carbon content of each precursor powder is reduced to 50-90 ppm without repeated pulverization and calcination.

#### *Effects of impurities*

Recent studies show that different impurity phases in Bi2212 wire play different roles on wire transport [32, 35, 57]. Here, two types of impurity phases are of particular interest, Bi2201 and AEC phases. For all batches of precursor powders, no Bi2201 is observed and the AEC phase is the only impurity phase. Based on previous results, due to incomplete

conversion from Bi2201 to Bi2212 during solidification during PMP, large Bi2201 grains remaining in heat treated wires have a significantly negative influence on transport  $J_c$  [35], which indicates that the absence of Bi2201 grains in the precursor powders is strongly preferred to lower the residual Bi2201 content after wire processing. Yet, AEC phases are not necessarily detrimental to wire transport. Large grains of AEC particles, i.e., larger than the wire filament size, can be detrimental to transport  $J_c$  as they act as big obstacles for current flow [33]. Small AEC grains, however, may act as nucleation sites for Bi2212 solidification during PMP [32]. Thus, the presence of AEC phases with particle sizes smaller than filament size is not considered to be problematic.

#### *Effects of wire filament size*

Previous studies show that the wire filament size has significant effects on wire transport behavior. Generally,  $J_c$  increases with decreasing filament size [58-61]. A 91 x 7 filament wire with an average filament size of 12-15  $\mu\text{m}$  was favorable for Bi2212 wire development. Here, this is the wire configuration of the Batch III wire, which obtained the highest  $J_c$ . The stoichiometry, carbon content, AEC content and AEC particle size for Batch I and Batch III precursor powders are similar, so the 30% higher transport  $J_c$  in Batch III wire is likely due in part to the significant filament size difference between the two green wires.

#### **Conclusions**

Nanosize oxides are used as starting materials to synthesize  $\text{Bi}_2\text{Sr}_2\text{CaCu}_2\text{O}_x$  oxide precursor powders. Homogeneous oxide mixtures with precisely controlled stoichiometries are produced by NanoSpray Combustion<sup>TM</sup> processing, and after a solid-state calcination, precursor powders contain over 99.1 vol% pure Bi2212 single crystals. With a single 72 hrs calcination, AEC remains as the only impurity phase in the precursor powders and the

particle sizes are smaller than 11  $\mu\text{m}$ . The residual carbon content in the precursor powders are less than 90 ppm. A series of quench studies shows complicated phase transformations, carbon release and grain growth with increasing time. With the cation stoichiometry and standard deviation well controlled within 0.6 mol% of nominal values, a Bi-rich and Ca-deficient stoichiometry gives highest wire transport  $J_c$  of 2520 A/mm<sup>2</sup> (4.2 K, 5 T). Effects of particle size, surface area, stoichiometry, chemical homogeneity and microstructures of the starting materials on Bi2212 formation as well as wire transport properties are discussed. Small particle size, high surface area and short diffusion length of the starting materials result in rapid and homogeneous phase transformations to Bi2212 without the aid of a liquid phase, along with early and rapid carbon release. The strong dependence of transport  $J_c$  on precursor stoichiometry indicates that the variation within precursor powders should be less than 1.5 mol%, such that a uniform melting behavior is achieved during wire heat treatment. Filament size also has significant impact on wire transport performance, particularly for precursor powders with otherwise similar properties.

### **Acknowledgements**

The authors are grateful to Leszek Motowidlo and Supramagnetics Inc for manufacturing the multifilamentary wires for this study. The authors acknowledge the use of the Analytical Instrumentation Facility (AIF) at North Carolina State University, which is supported by the State of North Carolina and the National Science Foundation. The authors also want to thank Jenna Pilato and Kyle Malone for assistance with this study. This study is funded through DOE-STTR (DE-SC0009705)

## REFERENCES

- [1] J. Schwartz, *et al.*, "High field superconducting solenoids via high temperature superconductors," *Ieee Transactions on Applied Superconductivity*, vol. 18, pp. 70-81, 2008.
- [2] A. Devred, *et al.*, "Future accelerator magnet needs," *Ieee Transactions on Applied Superconductivity*, vol. 15, pp. 1192-1199, Jun 2005.
- [3] L. Rossi, "Superconductivity: its role, its success and its setbacks in the Large Hadron Collider of CERN," *Superconductor Science and Technology*, vol. 23, Mar 2010.
- [4] S. A. Gourlay, *et al.*, "Magnet R&D for the US LHC Accelerator Research Program (LARP)," *Ieee Transactions on Applied Superconductivity*, vol. 16, pp. 324-327, Jun 2006.
- [5] A. S. Alexandrov, *et al.*, "Resistive Upper Critical Field of High- $T_c$  Single Crystals of Bi2212," *Physical Review Letters*, vol. 76, pp. 983-986, 1996.
- [6] Y. Wang, *et al.*, "Dependence of upper critical field and pairing strength on doping in cuprates," *Science*, vol. 299, pp. 86-89, January 3, 2003 2003.
- [7] Y. Ando and K. Segawa, "Magnetoresistance of Untwinned YBCO single crystals in a wide range of doping: anomalous hole doping dependence of the coherence length," *Physical Review Letters*, vol. 88, p. 167005, 2002.
- [8] W. T. Nachtrab, *et al.*, "Effect of Solidification Conditions on Partial Melt Processed Bi2212/Ag Round Wire," *Ieee Transactions on Applied Superconductivity*, vol. 21, pp. 2795-2799, Jun 2011.
- [9] T. Hatano, *et al.*, "High-temperature X-ray study of melting and solidification of the  $\text{Bi}_2\text{Sr}_2\text{CaCu}_2\text{O}_{8+\delta}$  on silver," *Journal of Low Temperature Physics*, vol. 117, pp. 777-781, 1999.
- [10] E. E. Hellstrom and W. Zhang, "Formation and prevention of bubbles when melt processing Ag-sheathed  $\text{Bi}_2\text{Sr}_2\text{CaCu}_2\text{O}_x$  (2212) conductors," *Superconductor Science and Technology*, vol. 8, p. 317, 1995.
- [11] W. Zhang, *et al.*, "Formation of Porosity and Its Effects on the Uniformity of  $J_c$  in Bi-2212/Ag Tapes," in *Advances in Cryogenic Engineering Materials*. vol. 44, U. B. Balachandran, *et al.*, Eds., ed: Springer US, 1998, pp. 509-516.
- [12] M. O. Rikel, *et al.*, "Competitiveness of porosity and phase purity in melt processed Bi2212/Ag conductors," *Physica C: Superconductivity*, vol. 354, pp. 321-326, 2001.

- [13] J. Jiang, *et al.*, "Doubled critical current density in Bi-2212 round wires by reduction of the residual bubble density," *Superconductor Science and Technology*, vol. 24, p. 082001, 2011.
- [14] C. Scheuerlein, *et al.*, "Void and phase evolution during the processing of Bi-2212 superconducting wires monitored by combined fast synchrotron micro-tomography and x-ray diffraction," *Superconductor Science and Technology*, vol. 24, p. 115004, 2011.
- [15] T. Shen, *et al.*, "Role of internal gases and creep of Ag in controlling the critical current density of Ag-sheathed  $\text{Bi}_2\text{Sr}_2\text{CaCu}_2\text{O}_x$  wires," *Journal of Applied Physics*, vol. 113, pp. -, 2013.
- [16] W. Zhang and E. E. Hellstrom, "The influence of carbon on melt processing Ag sheathed  $\text{Bi}_2\text{Sr}_2\text{CaCu}_2\text{O}_8$  tape," *Physica C: Superconductivity*, vol. 234, pp. 137-145, 1994.
- [17] J. F. Mitchell, *et al.*, "Rapid synthesis of 93 K Bi-2212 superconductor from hydroxide precursors," *Physica C: Superconductivity*, vol. 245, pp. 126-130, 1995.
- [18] A. P. Baker and B. A. Glowacki, "The effect of Bi content on the phase purity and the superconducting critical temperature of a Sr and Ca deficient Bi-2212 stoichiometry," *Physica C: Superconductivity*, vol. 227, pp. 31-39, 1994.
- [19] D. Sager, *et al.*, "Influence of precursor calcination parameters on the critical current density of Bi-2212 superconductors," *Physica C: Superconductivity*, vol. 434, pp. 125-134, 2006.
- [20] I. Bloom, *et al.*, "Solid state synthesis of  $\text{Bi}_2\text{Sr}_2\text{CaCu}_2\text{O}_x$  superconductor," *Materials Research Bulletin*, vol. 26, pp. 1269-1276, 1991.
- [21] S. Yoshizawa, *et al.*, "Effect of particle size in raw material CuO on superconductivity of HTSC," in *Advances in Superconductivity III*, K. Kajimura and H. Hayakawa, Eds., ed: Springer Japan, 1991, pp. 287-290.
- [22] S. C. Kim, *et al.*, "Effect of composition on critical current density of Bi2212/Ag round wires," *Cryogenics*, vol. 49, pp. 277-279, 2009.
- [23] H. Miao, *et al.*, "Studies of Precursor Composition Effect on  $J_c$  in Bi-2212/Ag Wires and Tapes," *AIP Conference Proceedings*, vol. 824, pp. 673-682, 2006.
- [24] N. Tohge, *et al.*, "Direct preparation of fine powders of the 80 K superconducting phase in the Bi-Ca-Sr-Cu-O system by spray pyrolysis," *Japanese Journal of Applied Physics*, vol. 28, p. L1175, 1989.

- [25] N. Tohge, *et al.*, "Preparation conditions and morphology of superconducting fine particles in the Bi-Ca-Sr-Cu-O system prepared by spray pyrolysis," *Journal of the American Ceramic Society*, vol. 74, pp. 2117-2122, 1991.
- [26] Y. Idemoto, *et al.*, "Oxygen nonstoichiometry of 2223 phase Bi-Pb-Sr-Ca-Cu-O system superconducting oxide," *Physica C: Superconductivity*, vol. 181, pp. 171-178, 1991.
- [27] J. Takada, *et al.*, "Superconductor with  $T_c = 117$  K in the Bi-Pb-Sr-Ca-Cu-O system," *Physica C: Superconductivity*, vol. 170, pp. 249-253, 1990.
- [28] L. Ben-Dor, *et al.*, "Physical characterization and vibrational spectroscopy of Bi(Pb) cuprate 2212 ceramics prepared by sol-gel," *Physica C: Superconductivity*, vol. 200, pp. 418-424, 1992.
- [29] D. Sager, *et al.*, "Critical current densities of Bi-2212 thick films processed from commercial precursors," *Physica C: Superconductivity*, vol. 420, pp. 69-77, 2005.
- [30] Y. Zhang, *et al.*, "Synthesis of  $\text{Bi}_2\text{Sr}_2\text{CaCu}_2\text{O}_x$  superconductors via direct oxidation of metallic precursors," *Superconductor Science and Technology*, vol. 27, p. 055016, 2014.
- [31] Y. Zhang, *et al.*, "Studies on multifilamentary  $\text{Bi}_2\text{Sr}_2\text{CaCu}_2\text{O}_x/\text{Ag}$  wire via metallic-powder-in-tube route," *manuscript in progress*, 2015.
- [32] G. Naderi, *et al.*, "Bi2212 round wire processing studies based on split melt and introducing saw-tooth processing," presented at the International Cryogenic Materials Conference, 2011.
- [33] X. T. Liu, *et al.*, "Influencing factors on the electrical transport properties of split-melt processed  $\text{Bi}_2\text{Sr}_2\text{CaCu}_2\text{O}_x$  round wires," *Superconductor Science and Technology*, vol. 25, Jul 2012.
- [34] S. Tengming, *et al.*, "Heat treatment control of  $\text{Ag-Bi}_2\text{Sr}_2\text{CaCu}_2\text{O}_x$  multifilamentary round wire: investigation of time in the melt," *Superconductor Science and Technology*, vol. 24, p. 115009, 2011.
- [35] C. Evan Benjamin, *et al.*, "Statistical analysis of the relationship between electrical transport and filament microstructure in multifilamentary  $\text{Bi}_2\text{Sr}_2\text{CaCu}_2\text{O}_x/\text{Ag}/\text{Ag-Mg}$  round wires," *Superconductor Science and Technology*, vol. 27, p. 044020, 2014.
- [36] M. O. Rikel, *et al.*, "Effect of composition on the melting behaviour of Bi2212-Ag conductors," *Journal of Physics: Conference Series*, vol. 43, p. 51, 2006.

- [37] J. Fransaer, *et al.*, "Sol-gel preparation of high- $T_c$  Bi-Ca-Sr-Cu-O and Y-Ba-Ca-O superconductors," *Journal of Applied Physics*, vol. 65, pp. 3277-3279, 1989.
- [38] T. Tsukamoto, *et al.*, "Preparation and superconducting properties of high-quality Bi-2212 ceramics," *Journal of Alloys and Compounds*, vol. 209, pp. 225-229, 1994.
- [39] D. Sager, *et al.*, "Novel precursor reaction pathways to Bi-2212 bulk superconductors," *Physica C: Superconductivity*, vol. 417, pp. 85-97, 2005.
- [40] A. Polasek, *et al.*, "The influence of precursor powder on the microstructure and properties of Bi-2212 blocks," *Physica C: Superconductivity*, vol. 460-462, Part 2, pp. 1349-1350, 2007.
- [41] A. Sotelo, *et al.*, "Precursor influence on the electrical properties of textured Bi-2212 superconductors," *Journal of Superconductivity and Novel Magnetism*, vol. 24, pp. 19-25, Jan 2011.
- [42] V. Garnier, *et al.*, "Relationship among synthesis, microstructure and properties in sinter-forged Bi-2212 ceramics," *Physica C: Superconductivity*, vol. 319, pp. 197-208, 1999.
- [43] S.-L. Huang, *et al.*, "Comparison of fully-reacted and partly-reacted  $\text{Bi}_2\text{Sr}_2\text{CaCu}_2\text{O}_y$  precursor powders," *Physica C: Superconductivity*, vol. 282-287, Part 4, pp. 2617-2618, 1997.
- [44] P. Majewski, *et al.*, "Relationships between the chemical composition and properties of the high-temperature superconductor  $\text{Bi}_{2+x}\text{Sr}_{2-y}\text{Ca}_{1+y}\text{Cu}_2\text{O}_{8+d}$ ," *Journal of Materials Science*, vol. 32, pp. 5137-5141, 1997.
- [45] A. Hunt, *et al.*, "Nanomaterials via nanoSpray combustion chemical vapor condensation and their electronic applications," in *Nano-Bio- Electronic, Photonic and MEMS Packaging*, C. P. Wong, *et al.*, Eds., ed: Springer US, 2010, pp. 139-166.
- [46] P. Boháček, *et al.*, "Composition of phases and phase mixtures of the Bi-Sr-Ca-Cu-O system," *Physica C: Superconductivity*, vol. 171, pp. 108-120, 1990.
- [47] P. Majewski, *et al.*, "The High- $T_c$  superconducting solid solution  $\text{Bi}_{2+x}(\text{Sr,Ca})_3\text{Cu}_2\text{O}_{8+d}$  (2212 Phase)-chemical composition and superconducting properties," *Advanced Materials*, vol. 4, pp. 508-511, 1992.
- [48] J. H. P. M. Emmen, *et al.*, "Crystal growth and annealing experiments of the high  $T_c$  superconductor  $\text{Bi}_2\text{Sr}_2\text{CaCu}_2\text{O}_{8+\delta}$ ," *Journal of Crystal Growth*, vol. 118, pp. 477-482, 1992.

- [49] S. M. Khalil and A. Sedky, "Annealing temperature effect on the properties of Bi:2212 superconducting system," *Physica B: Condensed Matter*, vol. 357, pp. 299-304, 2005.
- [50] T. G. Holesinger, *et al.*, "Characterization of the phase relations and solid solution range of the  $\text{Bi}_2\text{Sr}_2\text{Ca}_1\text{Cu}_2\text{O}_y$  superconductor," *Physica C: Superconductivity*, vol. 202, pp. 109-120, 1992.
- [51] H. Miao, *et al.*, "Development of Bi-2212 conductors for magnet applications," in *AIP Conference Proceedings*. vol. 711, ed, 2004, pp. 603-611.
- [52] K. Sandhage, *et al.*, "Critical issues in the OPIT processing of high- $J_c$  BSCCO superconductors," *The Journal of The Minerals, Metals & Materials Society*, vol. 43, pp. 21-25, 1991/03/01 1991.
- [53] G. D. Ulrich and N. S. Subramanian, "III. Coalescence as a Rate-Controlling Process," *Combustion Science and Technology*, vol. 17, pp. 119-126, 1977/12/01 1977.
- [54] E. E. Hellstrom, *et al.*, "Phase development and microstructure in Bi-based 2212 Ag-clad tapes processed at 880, 890, and 905 °C: The Cu-free phase and  $(\text{Sr,Ca})\text{CuO}_2$ ," *Applied Superconductivity*, vol. 1, pp. 1535-1545, 1993.
- [55] M. Polak, *et al.*, "The effect of the maximum processing temperature on the microstructure and electrical properties of melt processed Ag-sheathed  $\text{Bi}_2\text{Sr}_2\text{CaCu}_2\text{O}_x$  tape," *Ieee Transactions on Applied Superconductivity*, vol. 7, pp. 1537-1540, 1997.
- [56] G. R. Paz-Pujalt, "Solid state reactions in the formation of Bi-Sr-Ca-Cu-oxide superconductor from metallo-organic precursors," *Physica C: Superconductivity*, vol. 166, pp. 177-184, 1990.
- [57] G. Naderi, *et al.*, "Understanding processing–microstructure–properties relationships in  $\text{Bi}_2\text{Sr}_2\text{CaCu}_2\text{O}_x$  /Ag round wires and enhanced transport through saw-tooth processing," *Superconductor Science and Technology*, vol. 26, p. 105010, 2013.
- [58] L. R. Motowidlo, *et al.*, "The influence of filament size and atmosphere on the microstructure and  $J_c$  of round multifilament  $\text{Bi}_2\text{Sr}_2\text{CaCu}_2\text{O}_x$  wires," *Ieee Transactions on Applied Superconductivity*, vol. 5, pp. 1162-1166, 1995.
- [59] K. R. Marken, *et al.*, "BSCCO-2212 conductor development at Oxford Superconducting Technology," *Ieee Transactions on Applied Superconductivity*, vol. 13, pp. 3335-3338, Jun 2003.
- [60] W. T. Nachtrab, *et al.*, "The effect of filament diameter on  $J_c$  in high filament count Bi2212/Ag round wire," *Ieee Transactions on Applied Superconductivity*, vol. 19, pp. 3061-3066, 2009.

- [61] T. Hasegawa, *et al.*, "HTS conductors for magnets," *Ieee Transactions on Applied Superconductivity*, vol. 12, pp. 1136-1140, 2002.

## Chapter 3

### SYNTHESIS OF $\text{Bi}_2\text{Sr}_2\text{CaCu}_2\text{O}_x$ SUPERCONDUCTORS VIA DIRECT OXIDATION OF METALLIC PRECURSORS

Yun Zhang, Carl.C. Koch and Justin Schwartz

Department of Materials Science and Engineering

North Carolina State University, Raleigh, NC 27695

Supercond. Sci. Technol. **27** (2014) 055016

<http://iopscience.iop.org/0953-2048/27/5/055016>

#### Abstract

$\text{Bi}_2\text{Sr}_2\text{CaCu}_2\text{O}_x$  (Bi2212)/Ag multifilamentary wires are manufactured via the powder-in-tube process using oxide powders. After deformation, the wires undergo a partial melt process, resulting in a complex, heterogeneous microstructure containing multiple secondary phases and porosity, limiting wire electrical and mechanical performance. Here, an alternative approach using the direct conversion of metallic precursors (MP) to Bi2212 is studied. The formation of metallic precursor powders via mechanical alloy is discussed. The MP powder is then converted to superconducting Bi2212 through a simple two-step heat treatment. By introducing oxygen at a temperature at which Bi2212 is a stable phase, and holding at an elevated temperature for a sufficient time, the metallic precursors are oxidized and transformed into Bi2212. Several factors that impact the formation and growth of Bi2212 grains are discussed. Peak temperature, holding time and heating rate are shown to affect the MP  $\rightarrow$  Bi2212 conversion, the Bi2201 content and the Bi2212 morphology and density. It is found that  $\text{Bi}_2\text{Sr}_2\text{CuO}_y$  (Bi2201) can be the only phase impurity after heat treatment, which is

quite different from what is observed in partial-melt processed wires derived from oxide precursors. Lastly, the microstructure at the sample/silver interface suggests larger size and preferred orientation of Bi2212 grains with the aid of a silver surface. Implications for MP Bi2212 wires is discussed.

**Key words:** Bi2212, superconductor, metallic precursor, oxidation, critical temperature

List of abbreviations

Bi2201	$\text{Bi}_2\text{Sr}_2\text{CuO}_y$
Bi2212	$\text{Bi}_2\text{Sr}_2\text{CaCu}_2\text{O}_x$
Bi2223	$\text{Bi}_2\text{Sr}_2\text{Ca}_2\text{Cu}_3\text{O}_z$
MP	metallic precursors
$J_c$	critical current density
OPIT	oxide-powder-in-tube
PMP	partial-melt processing
CF	copper-free
AEC	alkaline earth cuprates
$T_{\text{ox}}$	oxidation temperature
$t_1$	dwelling time at $T_{\text{ox}}$
$T_p$	peak temperature
$t_p$	dwelling time at $T_p$
$R_1$	heating rate from $T_{\text{ox}}$ to $T_p$
FC	furnace cooling
$T_c$	critical temperature

$\Delta T_c$	$T_c$ transition width
$\gamma$	XRD intensity ratio
$f$	the fraction of Bi2201 intergrowths in Bi2212 grains

## Introduction

The upper critical fields of low temperature superconductors such as NbTi and Nb<sub>3</sub>Sn limit the maximum magnetic fields that can be generated to about 10.5 T and 20 T [1-3]. To meet the requirements for future applications such as a High Energy Large Hadron Collider, a muon collider and high field nuclear magnetic resonance magnets, a superconducting conductor capable of generating magnetic fields above 20 T is needed. One option is Bi<sub>2</sub>Sr<sub>2</sub>CaCu<sub>2</sub>O<sub>x</sub> (Bi2212) round wire, which has high critical current density ( $J_c$ ) in magnetic fields at least as high as 45 T [4] . As the only high field superconductor available as an isotropic round wire, Bi2212 wire sheathed in Ag/Ag-alloy is of particular interest [4-7] .

Currently, Bi<sub>2</sub>Sr<sub>2</sub>CaCu<sub>2</sub>O<sub>x</sub>/Ag wires are manufactured via the oxide-powder-in-tube (OPIT) route by filling Ag-tube with oxide precursors, deforming into wire, restacking (sometimes twice) and heat treating using partial-melt processing (PMP) or variants theory [8-14]. Yet the oxide precursor route has many shortcomings. One significant challenge is in low tap density, typically ranging from 1 g/cm<sup>3</sup> to 2.5 g/cm<sup>3</sup>, whereas the density of Bi<sub>2</sub>Sr<sub>2</sub>CaCu<sub>2</sub>O<sub>x</sub> is 6.45 g/cm<sup>3</sup>. Thus, starting from oxide precursors, it is not possible to obtain a 100% dense green wire. During PMP, bubbles and voids form and evolve, greatly reducing the transport  $J_c$  of wire [15, 16]. Another challenge related to the use of oxide precursors is that during PMP the Bi2212 powder melts incongruently, forming several non-superconducting crystalline phases and a liquid phase [9, 17]. During subsequent cooling, these non-

superconducting phases cannot convert completely to Bi2212, resulting in phase impurities, including  $\text{Bi}_2\text{Sr}_2\text{CuO}_x$  (Bi2201), a copper-free (CF) phase and alkaline earth cuprates (AEC) [18, 19]. Furthermore, for multifilamentary OPIT Bi2212 wires, high  $J_c$  depends on interfilamentary bridging resulting from resolidification [20]. The Bi2212 bridges are the essential links that allow superconducting electrons to meander around porosity and non-superconducting phases. Due to bridging, however, the effective filament size from a magnetization perspective is the wire diameter, which may be problematic for some applications. A true multifilamentary wire, without bridges, porosity and non-superconducting phases, is sought.

An alternative to the oxide precursor route with the potential to address these issues is metallic precursors (MP) that are not oxidized until after wire deformation. Previously, MP were studied for  $\text{Bi}_2\text{Sr}_2\text{Ca}_2\text{Cu}_3\text{O}_z$  (Bi2223) powder-in-tube (PIT) tapes. While MP Bi2223 wires achieved a certain level of success, ultimately an OPIT process replaced the MP Bi2223 approach. There are key differences between Bi2212 wires and Bi2223 tapes indicating that the MP route may be more suitable for Bi2212 than for Bi2223. One of the most fundamental differences between Bi2212 and Bi2223 tapes is the stability of the superconducting phase. The phase equilibria of the quaternary system  $\text{Bi}_2\text{O}_3$ -SrO-CaO-CuO shows that the Bi2212 phase is thermodynamically stable over a wide temperature range and coexists with most of the compounds in this system. In contrast, Bi2223 phase is stable within a narrow temperature range and exhibits phase equilibria with only a few of the compounds in the system [21]. Pb-free Bi2223 single crystals and pure Bi2223 powders are difficult to obtain, and most Bi2223 tape research and development focused on Pb-doped stoichiometries [22-25]. In contrast, the stable phase field for Bi2212 covers a large range of

Bi, Sr, and Ca stoichiometries and a broad temperature space [26-30]. Thus, the direct conversion from metallic precursors to Bi2212 is likely to be straightforward and faster than the conversion to Bi2223. Rapid, direct conversion will also minimize the interdiffusion of Bi2212 cations with the Ag sheath [31]. Lastly, the Pilling-Bedworth ratio for Bi2212 and Bi2223 are 1.112 and 1.294, respectively, indicating that during the metal-to-ceramic conversion, the net expansion of Bi2212 is less than half of that of Bi2223.

Another potential advantage of the MP route is the absence of carbon. The presence of carbon and carbon contamination during oxide precursor processing has serious consequences due to the evolution of CO<sub>2</sub> during PMP, and as a result oxide powder manufacturers focus significant attention on minimizing the carbon content. The impact of carbon content on heat treated wires has been studied by varying calcination conditions before packing powders into Ag tubes. J<sub>c</sub> was greatly reduced by the presence of carbon, particularly in the form of carbonates. High carbon residue results in poor grain connectivity and increased porosity [32-34].

The current work focuses on the preparation of MP powders and their conversion to superconducting oxide Bi2212. Solid state sintering, including the crucial step of the direct oxidation of metallic precursors, is studied using pressed pellets. Heat treated pellets are studied extensively, including thermal, chemical, microstructural and magnetic characterizations.

## **Experimental approach**

### **1. Sample preparation**

The starting metals are 0.074 mm bismuth powders, 0.5-1.5 μm copper powders, 19 mm strontium granules and 1 mm calcium granules all with high purity (≥99.5%). For one

powder batch, 0.5-1.0  $\mu\text{m}$  silver powder (purity of 99.9%) is added as well. Before mixing, the Sr granules are charged within a Spex zirconia milling vial and ball-milled for 2 hrs using a Spex 8000 to reduce the particle size to 0.5  $\mu\text{m}$ .

The handling of MP requires particular caution because Ca and Sr are highly reactive with  $\text{O}_2$  and water. Thus, all the powder handling requires a carbon-free, oxygen-free, dry environment. Here, the weighing, storing and milling of MP are under an Ar atmosphere.

According to the phase diagram [35, 36], the central axes of the single phase region points to a Bi stoichiometry of 2.18 in the temperature range of 820  $^\circ\text{C}$  to 870  $^\circ\text{C}$  in air. As the temperature decreases, the single-phase region becomes large. For Bi2212 phase within the composition range  $\text{Bi}_{2.18}\text{Sr}_{3-y}\text{Ca}_y\text{Cu}_2\text{O}_{8+d}$  ( $y = 0.4 - 2.0$ ), the single phase extends furthest when  $y=1.10$  and decreases slightly as  $y$  increases [26]. Here, the starting materials are mixed with a cation ratio of Bi:Sr:Ca:Cu of 2.18:1.90:1.10:2.00, a stoichiometry in the middle of the single-phase region. The endpoints of the Bi2212 solid solution region remain almost unchanged from 100%  $\text{O}_2$  to 1.0%  $\text{O}_2$ . Therefore, this stoichiometry remains in the center of the single phase region as the oxygen partial pressure varies from 100% to 1.0% [36].

Two batches of powders are milled with the same Bi:Sr:Ca:Cu ratio; in one batch 5wt% Ag is added. After weighing and mixing all the powders in a high purity (<1 ppm oxygen) argon atmosphere in a glovebox, they are charged again within a Spex zirconia milling vial and mechanically alloyed for 20 hours. After milling, powders are stored in glass vials in an argon atmosphere. Table 3-1 lists the cation ratios of Bi, Sr, Ca, Cu and weight percentage of Ag as detected by chemical analysis after milling but before heat treatment. Batch I was milled continuously while Batch II was milled with intermittent scraping. The cation ratios and Ag content deviate from the starting stoichiometry of  $\text{Bi}_{2.18}:\text{Sr}_{1.90}:\text{Ca}_{1.10}:\text{Cu}_{2.00}$ , which

may be due to some elements sticking preferentially to the milling vial and balls; intermittent scraping of Batch II was used to reduce this effect.

Table 3-1: Chemical analysis of metallic precursors after milling

<b>Sample</b>	<b>Bi</b>	<b>Sr</b>	<b>Ca</b>	<b>Cu</b>	<b>Ag(wt%)</b>
<b>Starting mixture (pre-milling)</b>	2.18	1.90	1.10	2.00	-
<b>Batch-I (milled &amp; unreacted)</b>	2.22	1.82	1.15	2.00	0
<b>Batch-II (milled &amp; unreacted)</b>	2.19	1.87	1.13	2.00	1.94

Pellets with a 6 mm diameter, 1.0-1.2 mm thickness and 0.18-0.20 g mass are made from milled powders; 3 pellets are made from Batch I (I-1-3) and 6 from Batch II (II-1-6). A reference pellet is also made from oxide precursor (as received Nexans Bi2212 granules). All pellets are pressed using a uniaxial press at a pressure up to 2 GPa and a density of up to 5.30 g/cm<sup>3</sup>. Milled metallic precursors are filled and sealed into a 6 mm die in a glovebox and then the die is taken out for pressing.

## 2. Heat treatment

To avoid intense reactions between the metallic precursors and oxygen, and to ensure that the starting stoichiometry to be in the single phase region, a series of two-step heat treatments are carried out under 10% O<sub>2</sub> (Ar balance) atmosphere with different temperatures and times in a quartz tube furnace. Figure 3-1 shows a schematic drawing of typical two-step heat treatment profile. For each heat treatment, the pellet sample is taken from the glovebox just before heat treatment and put on a silver foil in an alumina boat. The furnace is then sealed, vacuumed

and refilled with pure Ar repeatedly to ensure that there is no oxygen in the quartz tube before heat treatment.

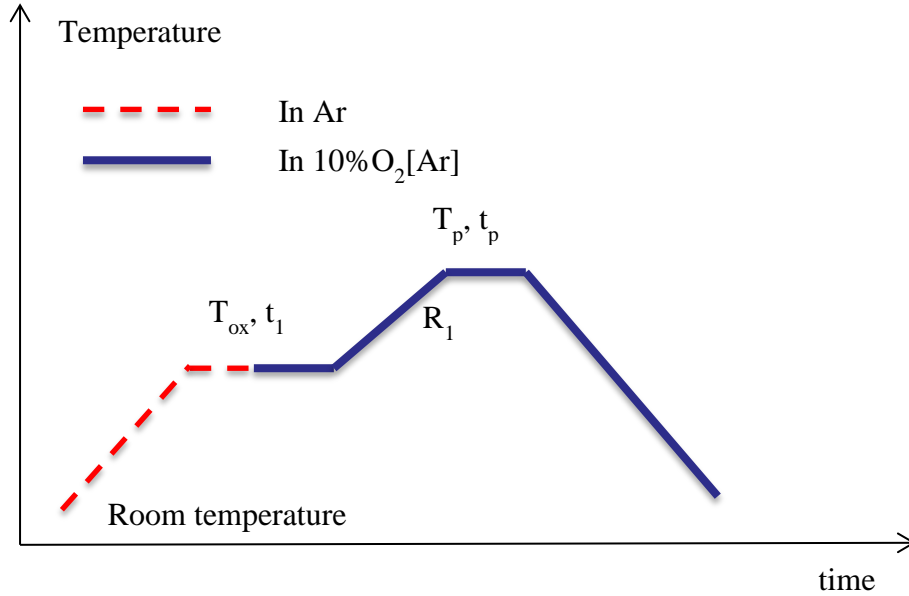


Figure 3-1 Schematic drawing of the two-step heat treatment temperature-time profile.

Heat treatments include two dwelling steps, one at  $T_{ox}$  and the other at  $T_p$ . Step 1 is used to directly oxidize the metallic precursors at  $T_{ox}$  instead of  $T_p$ , avoiding melting as there is considerable amount of Bi and Sr, with melting points of 271.4 °C and 768.8 °C, in the green pellets. Hence, early oxidation, before the temperature reaches  $T_p$ , is needed to prevent elemental diffusion within a liquid phase which might harm the final homogeneity of the pellet. Moreover, Bi2212 crystallization at 630 °C in air from glass oxide precursors has been reported [26]. Hence, two values of  $T_{ox}$  are studied, 600 °C and 650 °C. Compared to conventional PMP in 100% oxygen, the reduced oxygen partial pressure used here reduces

the Bi2212 melting temperature to around 870 °C [37]. Thus, to avoid partial melting during heat treatment,  $T_p$  is studied in the range 800 °C - 855 °C.

After pumping, the sealed furnace is heated to  $T_{ox}$  at a rate of 300 °C/h in flowing Ar and held for 10 minutes to allow the temperature to stabilize, after which a flow of 10%  $O_2$  mixed gas is introduced. After holding at  $T_{ox}$  for a specific amount of time,  $t_1$ , the system is heated to  $T_p$  at a rate of  $R_1$  and held for  $t_p$ . Finally, the system is cooled to room temperature at a rate of 100 °C/h or furnace cooled (FC) (~400 °C/h). Detailed heat treatment parameters are listed in Table 3-2.

Table 3-2: Detailed heat treatment parameters for each sample

<b>Sample</b>	<b><math>T_{ox}</math> (°C)</b>	<b><math>t_1</math> (h)</b>	<b><math>T_p</math> (°C)</b>	<b><math>t_p</math> (h)</b>	<b><math>R_1</math> (°C/h)</b>	<b>Cooling rate (°C/h)</b>
<b>I-1</b>	650	2	800	2	200	100
<b>I-2</b>	600	2	830	2	200	100
<b>I-3</b>	650	2	830	2	200	100
<b>II-1</b>	650	0	845	16	200	FC
<b>II-2</b>	650	0	845	48	200	FC
<b>II-3</b>	650	0	855	16	200	FC
<b>II-4</b>	650	0	855	48	200	FC
<b>II-5</b>	650	0	855	16	60	FC
<b>II-6</b>	650	0	855	48	60	FC

### 3. Characterization

Inductive-coupled-plasma emission spectroscopy (ICP-ES) (Perkin Elmer 2000 Dual View spectrometer) is used to determine the stoichiometry of milled batches (Table I). Samples are weighed on Teflon microwave digest sample holders to the nearest  $10^{-5}$  g. 5 mL of 4:1 ([conc. HCl]: [conc. HNO<sub>3</sub>]) is then added to each sample. The solution then sits for 48 hr.

A JEOL 10LA scanning electron microscope (SEM) with energy dispersive spectrometry (EDS) is used to examine the homogeneity of the elemental distribution of milled batches. Hitachi S3200 and TM3000 SEMs are used to investigate the microstructures of heat treated samples.

An FEI Titan 80-300 probe aberration corrected scanning transmission electron microscope (STEM) with SUPER X EDS is used to characterize the Bi2201 intergrowths of a heat treated sample.

A Rigaku Smartlab X-ray Diffractometer (XRD) is used for phase analysis. The measurements are carried out with a Cu-K<sub>α</sub> source over a 2θ range of 5 to 75 degrees, using 40 kV and 44 mA. To avoid oxidation of metallic precursors during handling, a thin mineral oil film is coated on the pellet surface in the glovebox before removal for analysis. For heat treated samples, the pellets are pulverized into fine powders before scanning.

The superconducting critical temperature, T<sub>c</sub>, is measured in a SQUID magnetometer (Quantum Design MPMS-5S) via magnetization versus temperature measurements. The samples are cooled to 4.2 K in zero field and measured in a 100 Oe applied field during warming.

Differential thermal analysis (DTA) (Perkin Elmer STA 6000) is used to study the melting behavior of heat treated samples to investigate the phase purity. All tested samples are 40 mg  $\pm$  0.002 mg and are heated to 980 °C at 10 K/min in flowing 10% O<sub>2</sub> (20 ml/min).

## Results

### 1. MP powder characterization

Figure 3-2 shows an SEM micrograph and corresponding EDS maps of the elemental distributions of Bi, Sr, Ca and Cu in Batch I before heat treatment. A homogeneous distribution of elements is observed after milling. Similar homogeneity is observed in Batch II. Figure 3-3 shows the XRD results for both batches after milling but before heat treatment. Note that in addition to elemental metals (Bi, Cu and Sr), some alloys formed during milling (Ca-Cu and/or Bi-Sr).

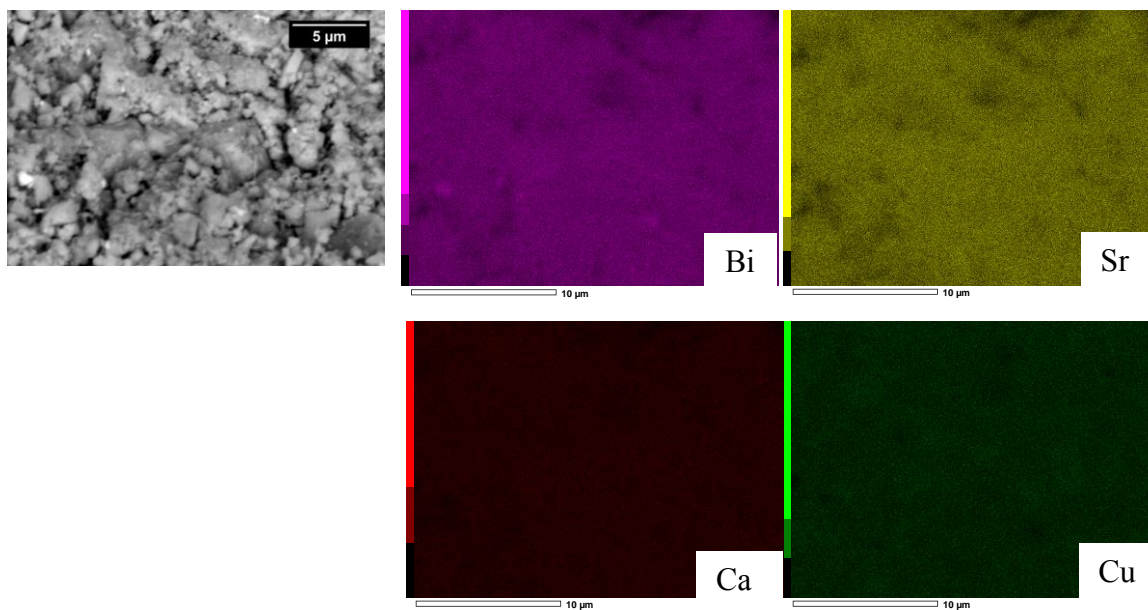


Figure 3-2 SEM micrograph and EDS maps of batch I after milling but before heat treatment.

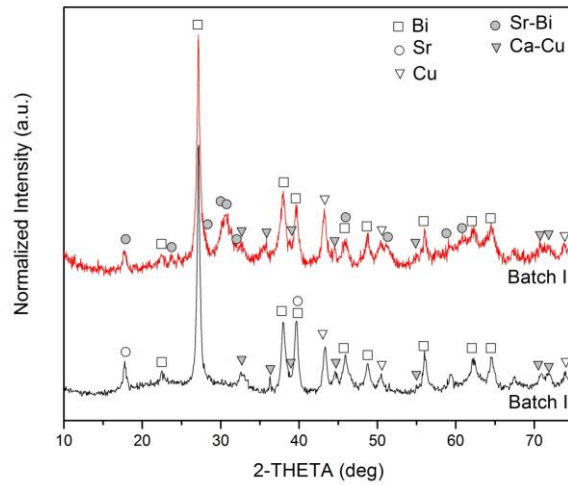


Figure 3-3 XRD results for Batch I and II after milling but before heat treatment.

## 2. Heat treated pellets

Figure 3-4 and 5 show magnetic properties of heat treated samples measured by SQUID. Figure 3-4 shows the absolute magnetic moment versus temperature for samples from Batch I and Batch II. All heat treated samples show a superconducting transition in the range of 69 K to 81 K, and only sample I-1 had a lower magnetic moment at 4.2 K than Nexans granules. Figure 3- 5 shows the same data normalized by reference values at 4.2 K. Only sample I-1 exhibits a shallower transition than Nexans granules.  $T_c$ s of samples I-1-3 (Figure 3- 5(a)) are 69.0 K, 77.5 K and 79.0 K, respectively, and  $T_c$ s of samples II-1-4 are 79.0 K, 79.5 K, 80.5 K and 81.0 K, respectively (Figure 3- 5(b)). The Nexans granules sample has a  $T_c$  of 67.5 K .

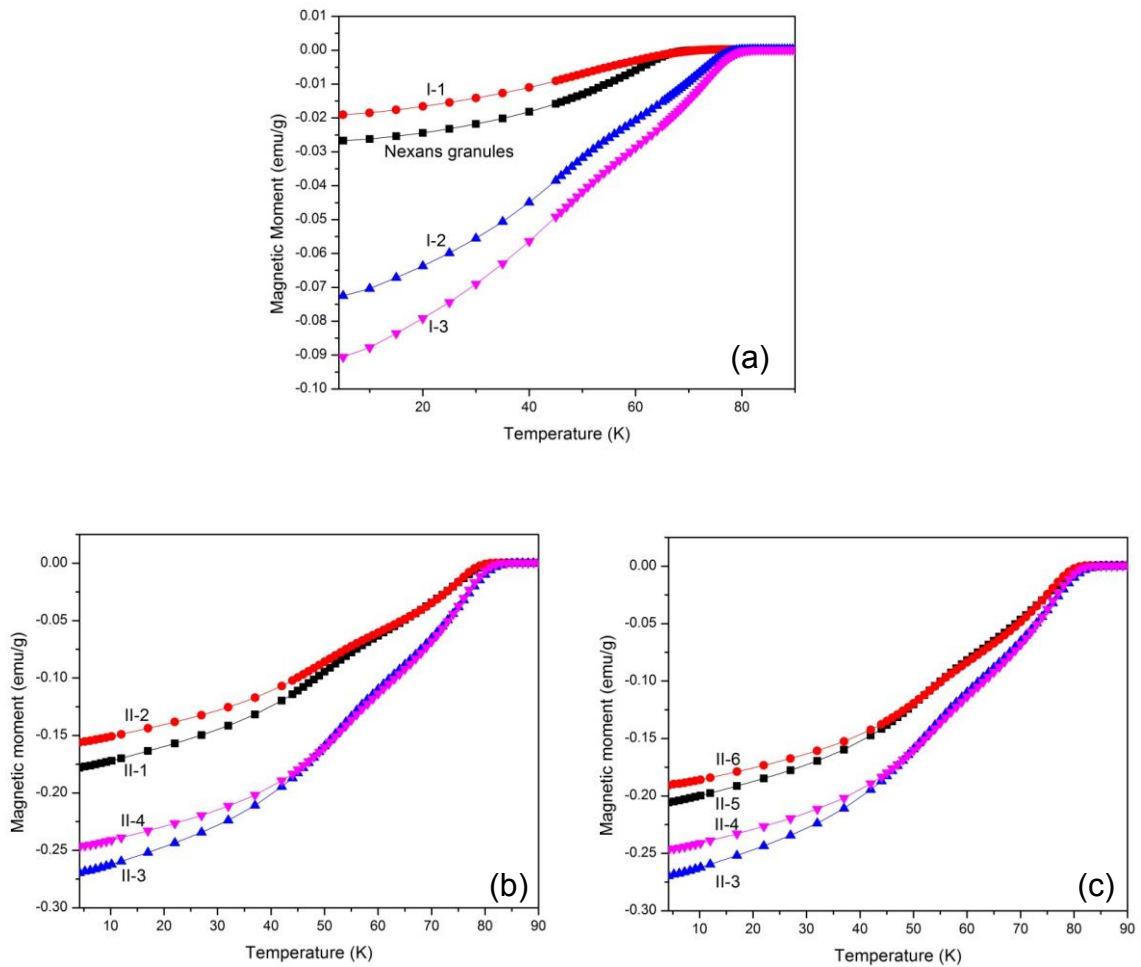


Figure 3-4 Magnetization versus temperature of heat treated samples and a reference Nexans granule sample. Samples from (a) batch I and the Nexans granule sample, (b) batch II to compare the effects of  $T_p$  and  $t_p$ , and (c) batch II to compare the effect of R1. Note that (a) has a much smaller range of moment than (b) and (c).

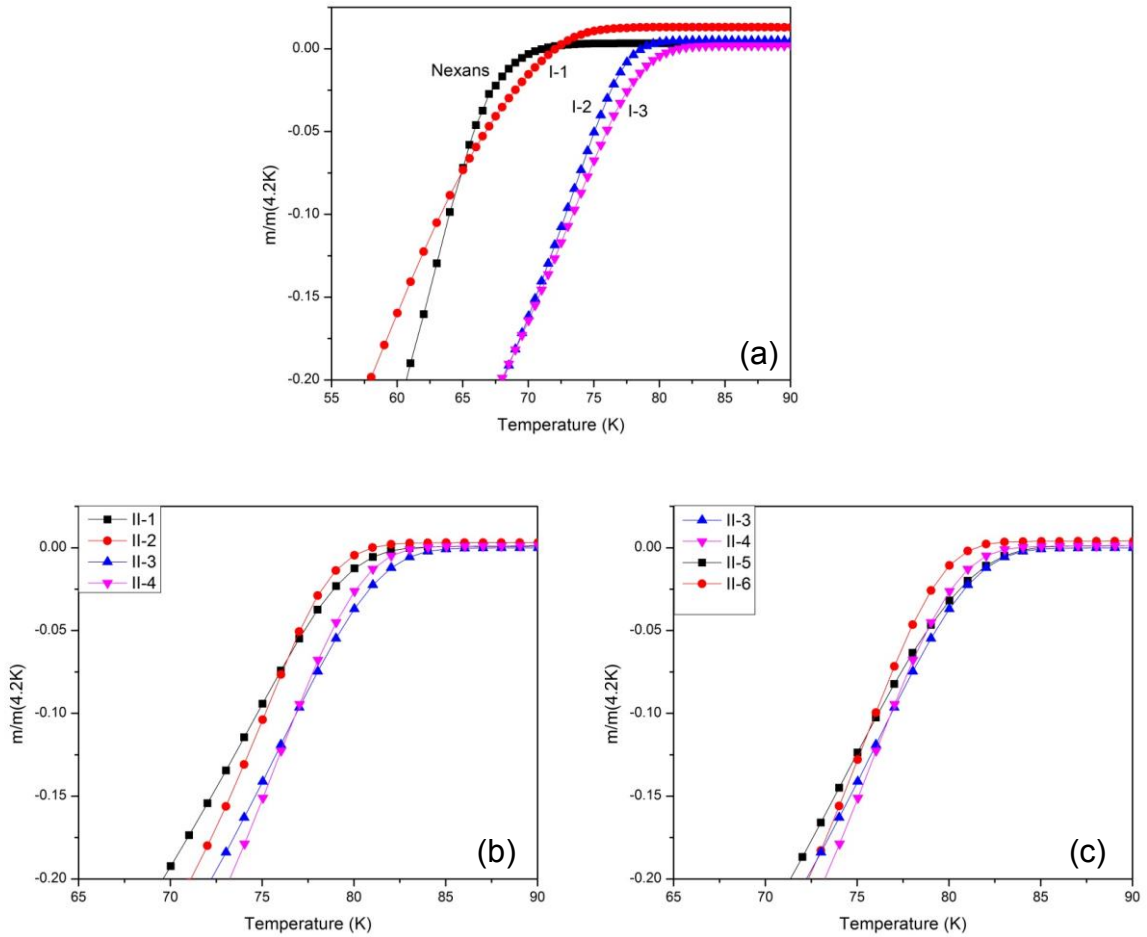


Figure 3-5 Normalized magnetization versus temperature. Samples from (a) batch I and the Nexans granule sample, (b) batch II to compare the effects of  $T_p$  and  $t_p$ , and (c) batch II to compare the effect of  $R_1$ .

Figure 3-6 shows the XRD patterns for three heat treated samples, I-3, II-1 and II-4; the major peaks of each phase are indexed. XRD results (not shown) from Batch I indicate that all samples contain Bi2212, Bi2201 and Cu-free phase. In contrast, for Batch II, only sample

II-1 contains Cu-free phase whereas the others contain only Bi2201 and Bi2212. Thus, the XRD patterns in Figure 3-6 are indicative of all samples. Figure 3-7 shows enlarged sections for  $2\theta$  between  $21^\circ$  and  $24^\circ$ , showing the relative intensity of the 006 (Bi2201) peak and 008 (Bi2212) peak of different samples from Batch II.

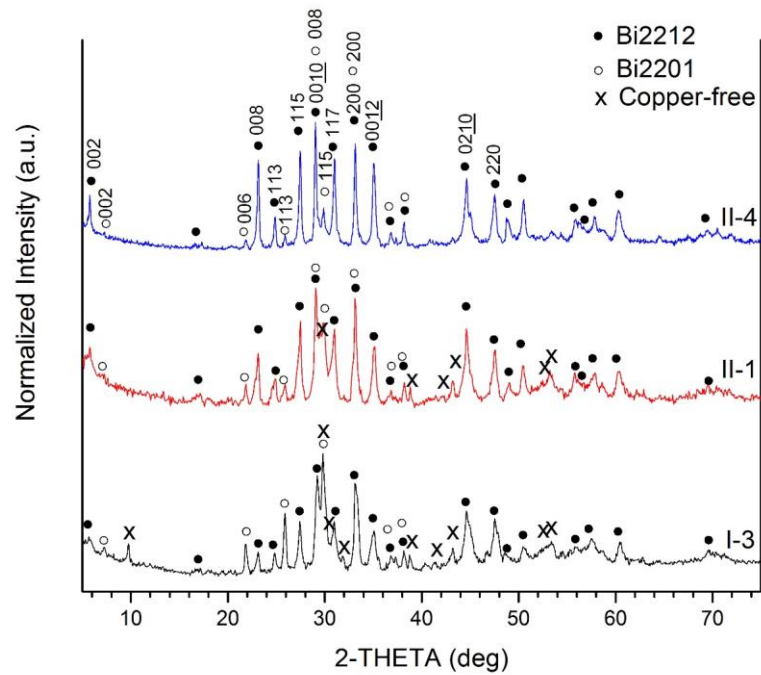


Figure 3-6 XRD results of heat treated samples I-3, II-1 and II-4.

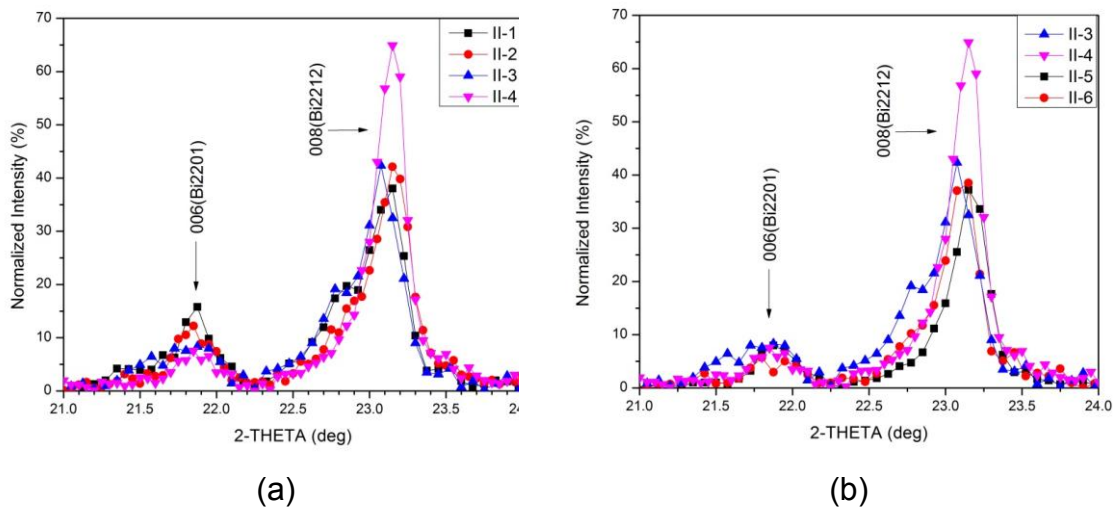


Figure 3-7 XRD results, focusing on the Bi2201 006 and Bi2212 008 peaks, to compare

(a) the effects of  $T_p$  and  $t_p$ , (b) the effect of  $R_1$ .

DTA curves of different heat treated samples and Nexans granules are shown in Figure 3-8. Additional peaks around the main melting peak are indicated by arrows. The melting onsets of samples II-1-6 are all  $876 \pm 1$  °C. Figure 3-8(a) compares samples II-1-4 to show the effects of  $T_p$  and  $t_p$  while (b) compares samples II-3-6 to show the effects of  $R_1$ . The peak width of Nexans granules is much wider than that for the converted metallic precursor samples. In (a), for samples II-1-3 and Nexans granules, there are additional peak(s) around the main melting peak, suggesting multiple melting events. There is no observable additional peak for sample II-4. In (b) there are also additional peaks around the main melting peak for samples with a low heating rate, i.e. samples II-5 and II-6.

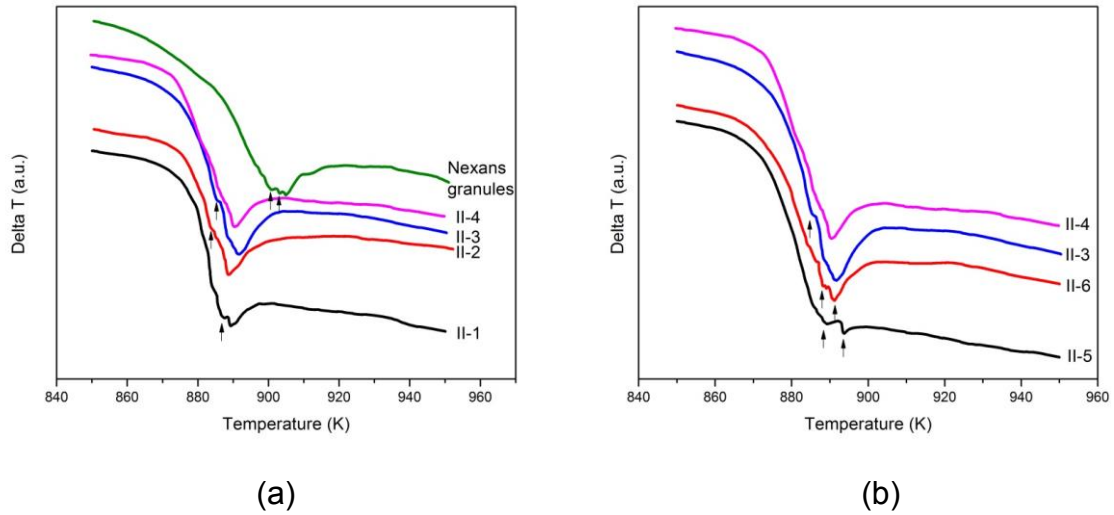
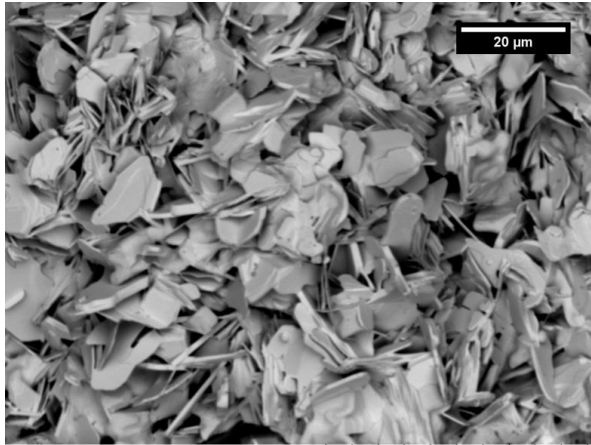


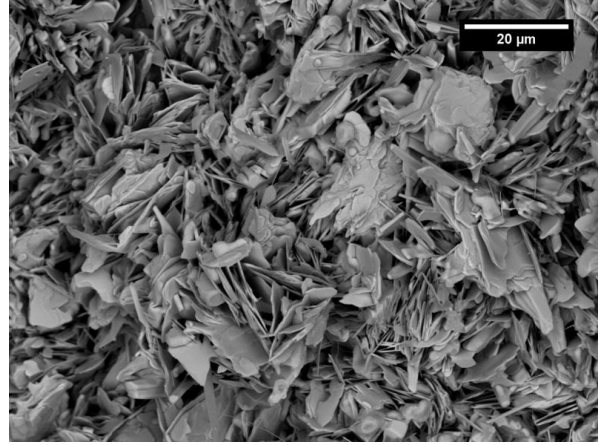
Figure 3-8 DTA curves showing melting peaks to compare

(a) effects of  $T_p$  and  $t_p$ ; (b) effect of  $R_1$ .

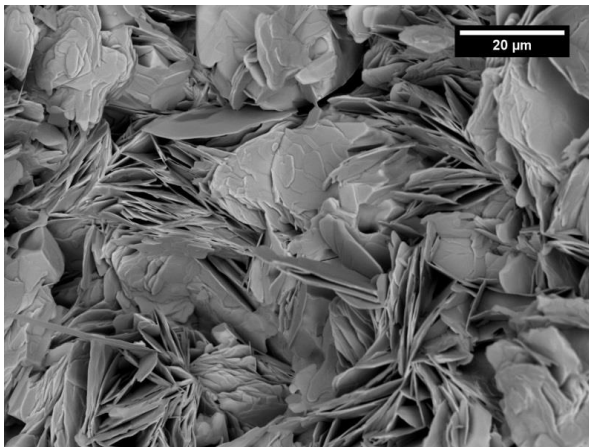
Figure 3-9 shows top surface SEM images of samples II-1-4. By increasing  $T_p$  from 845 °C to 855 °C, the grain size increases from approximately 10-15  $\mu\text{m}$  to more than 20-25  $\mu\text{m}$ . By increasing  $t_p$  from 16 hours ((a) and (c)) to 48 hours ((b) and (d)), the grain size increases, but the effect is less dramatic than temperature. Figure 3-10 shows cross-sectional SEM images of polished samples II-3 and II-4. Closely stacked Bi2212 grains with an average size of 25  $\mu\text{m}$  are formed when  $T_p$  reaches 855 °C. Porosity exists between the aligned grains in sample II-3 and is reduced in sample II-4. Figure 3-11 shows the microstructure at the pellet/Ag interface of samples II-1 and II-2. Comparing the images from the top of those samples with those at the Ag interface, the Bi2212 grains at the Ag interface are much larger than those at the top and are well connected.



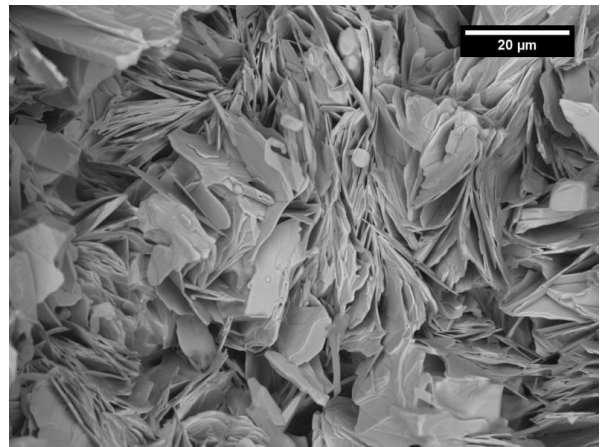
(a)



(b)



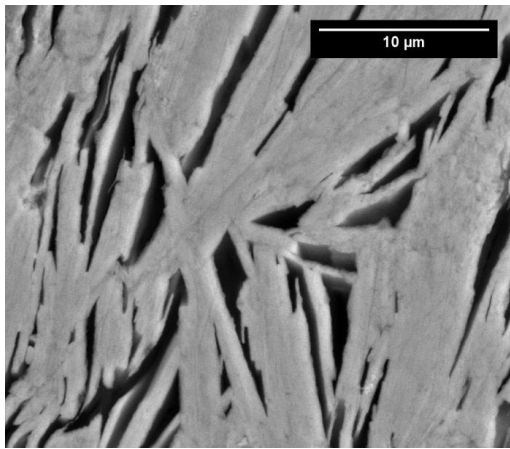
(c)



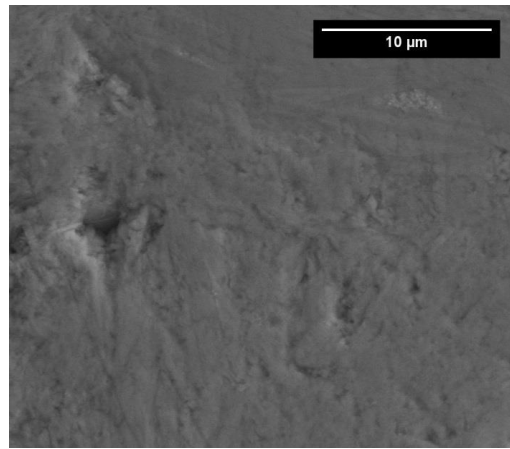
(d)

Figure 3-9 SEM images of the top surfaces of heat treated samples.

(a) II-1 (b) II-2 (c) II-3 (d) II-4.

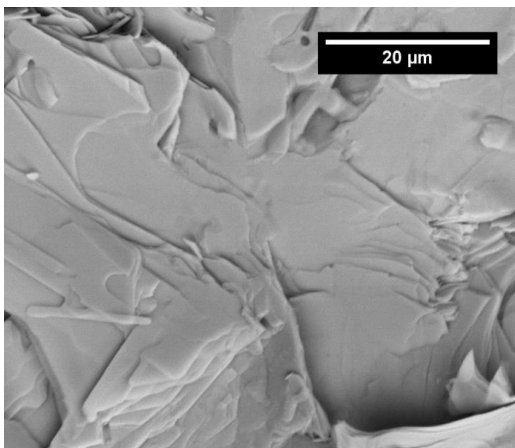


(a)

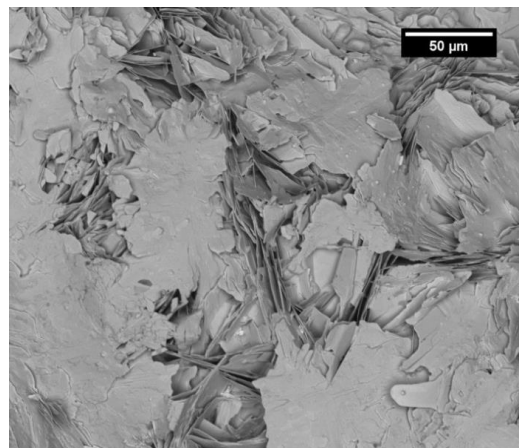


(b)

Figure 3-10 Cross-sectional SEM images of polished samples (a) II-3 and (b) II-4.



(a)



(b)

Figure 3-11 SEM images of the pellet/Ag interface of samples (a) II-1 and (b) II-2.

Figure 3-12 shows STEM images of sample II-4. Bi2212 grains with Bi2201 half-cell intergrowths are seen. With increasing magnification, it is clear that each bright line in (a) and (b) is a half unit cell of Bi2201 with a 1.2 nm spacing. In (c), one Bi2212 unit cell with a 3.1 nm spacing is seen between the two Bi2201 half-cells. EDS mapping confirms that the two bright lines in the STEM images are Ca-deficient. No large Bi2201 grains are observed in this sample.

Table 3-3 shows the XRD intensity ratio  $\gamma$  ( $\gamma = \frac{I_{008}}{I_{0010}} \times 100\%$ ) of 008 and 0010 peaks of the Bi2212 phase for six samples. The  $\gamma$  values are used to calculate the fraction of Bi2201 intergrowths in Bi2212 grains ( $f$ ) based on the model developed by Rikel et al. [38, 39]; these are also listed in Table 3-3.

Figure 3-12 (a), (b) STEM images of Bi2212 grains from sample II-4 with Bi2201 intergrowths and (c) EDS maps showing the Bi2201 halfcell intergrowths.

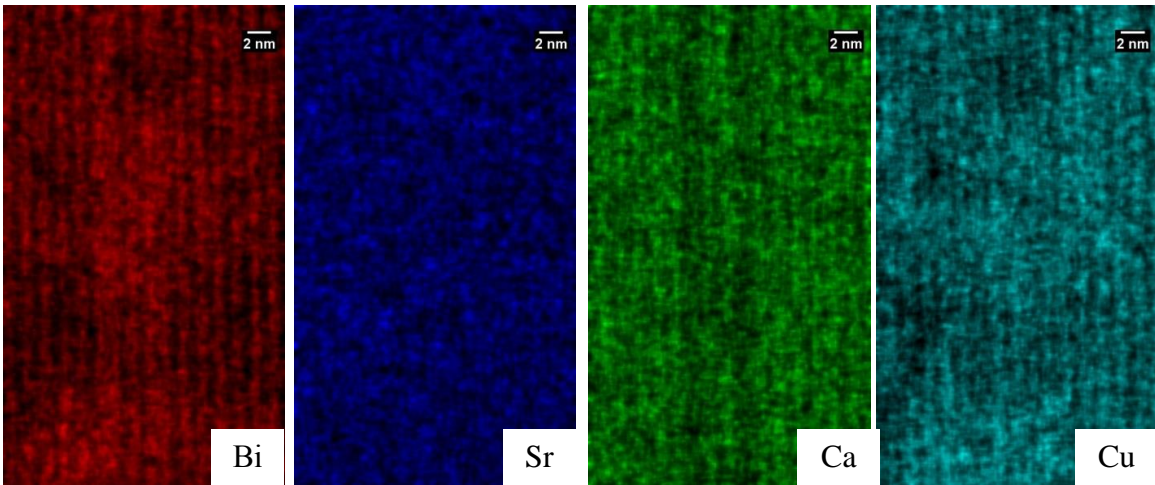
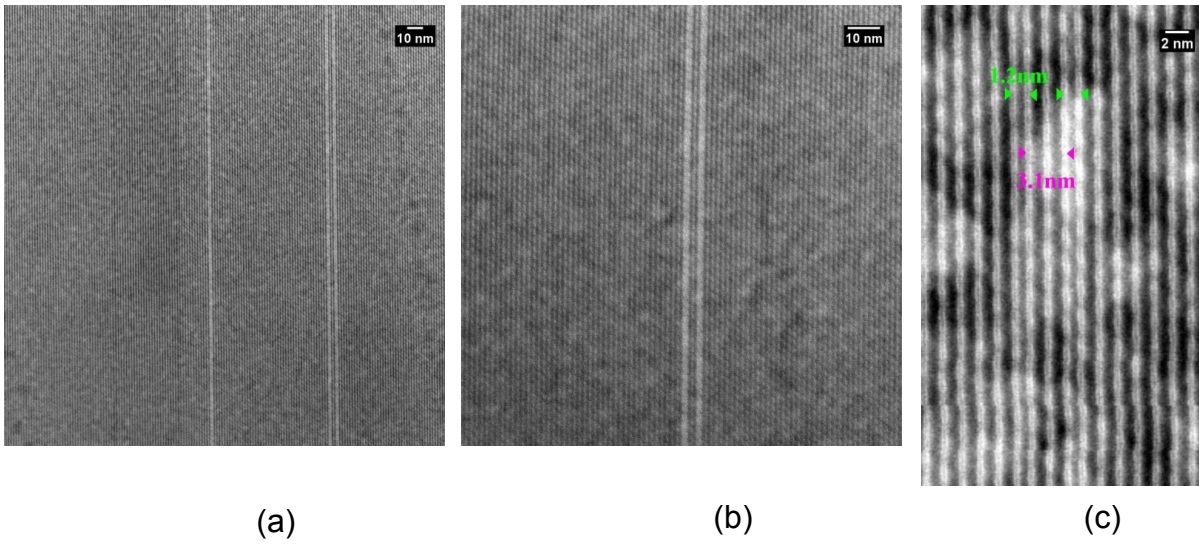


Table 3-3: Intensity ratio  $\gamma$  and fraction  $f$  of Bi2201 intergrowth in Bi2212 grains

Sample	II-1	II-2	II-3	II-4	II-5	II-6
$\gamma$	53 $\pm$ 1	52 $\pm$ 1	53 $\pm$ 1	73 $\pm$ 1	49 $\pm$ 1	50 $\pm$ 1
$f$ (%)	11 $\pm$ 3	12 $\pm$ 3	11 $\pm$ 2	5 $\pm$ 2	14 $\pm$ 4	13 $\pm$ 4

## Discussion

### 1. Properties of metallic precursors

The XRD results of milled precursors in Figure 3-3 show a combination of elemental metals (Bi and Cu) and metal alloys. A Ca-Cu alloy is common to both batches, whereas Batch II also shows a Sr-Bi alloy which might be a result of the intermittent scraping giving a more homogeneous mixing of powders. Chemical analysis in Table 1 shows that the result of cation ratios in Batch II is closer to the nominal stoichiometry of the starting powders, indicating that Sr sticks preferably to the mixing media and that the intermittent scraping is beneficial.

The metal alloys formed during milling may be a source of impurities upon oxidation, such as copper-free phases in samples I-1-4 and II-1 as shown in Figure 3-6. As there is no detectable copper-free phase or other non-superconducting phases in samples II-2-6, any alloys formed during milling are reactive and not stable during heat treatment.

### 2. Effects of heat treatment parameters $T_p$ and $t_p$

Magnetic measurements of the three Batch I samples indicate that a higher peak temperature yields a larger magnetic response, indicative of enhanced Bi2212 formation.  $T_p$  is either 800 °C or 830 °C, which is 80 °C or 50 °C below the Bi2212 melting temperature in 10% O<sub>2</sub>.

The reactions of oxidized powders were not complete and a considerable amount of Cu-free phase and Bi2201 phase was found in heat-treated samples. This is probably due to the very low diffusion rate of cations and high activation energy required to form Bi2212 via solid-state reactions [40, 41]. The activation energy of the transformation from Bi2201 to Bi2212 in the solid state, without the aid of liquid, is 3.0 to 6.7 times larger than with partial melt processing. Kinetic studies of Bi-Sr-Ca-Cu-O phases also imply a diffusion-controlled transformation [41]. Thus, the non-superconducting phases that formed in the early stages of the heat treatments are not fully converted to Bi2212 by diffusion at low  $T_p$ . With  $T_p$  well below the melt temperature, the phase transformation is limited. Note that increased  $T_p$  also increases  $T_c$ , consistent with results reported by others [26, 42]. The transition width  $\Delta T_c$  of sample I-1 is 5-6 K while those for samples I-2 and I-3 are within 2 K, indicating increased oxygen homogeneity in samples I-2 and I-3 [43]. This also confirms the more efficient diffusion among grains due to the increase in  $T_p$ .

Based on the Batch I results, Batch II studies focused on higher  $T_p$  (845 °C and 855 °C) and longer  $t_p$  (16 hrs and 48 hrs). Samples II-1-4 were heated from 650 °C to  $T_p$  at 200 °C/h. Magnetization measurements show that the samples with higher  $T_p$  (II-3 and II-4) have approximately 35% larger magnetization than those with lower  $T_p$  (II-1 and II-2). Furthermore, the magnetic results show that longer  $t_p$  results in an 8%- 12% decrease in magnetic moment at 4.2 K.  $T_c$  results indicate that for  $T_p$ s of 845 °C and 855 °C, the influence of increasing  $T_p$  on  $T_c$  is small. Also,  $T_c$ s of samples II-1-4 are all close to 80 K, with oxygen content  $x$  close to 8.0 [44]. The transition width  $\Delta T_c$  of these four samples are within 1 K, indicating a more homogeneous distribution of oxygen content with increased  $T_p$  [43].

Figure 2- 7 shows the relative intensity of the 006 (Bi2201) peak and 008 (Bi2212) peak as a function of  $T_p$  and  $t_p$ . With increasing  $T_p$  and  $t_p$ , the 006 (Bi2201) peak decreases and the 008 (Bi2212) peak increases. The XRD results show that for Batch II, only sample II-1, which was heat treated with lower  $T_p=845$  °C and shorter  $t_p=16$  hours, has Cu-free phases while the others have only Bi2201 and Bi2212 phases. There is no obvious peak for the ordered 4413 phase (an intermediate phase of mixed Bi2212 and Bi2201) as reported by others [39, 45, 46]. Rikel et al. developed a model that correlates the Bi2201 intergrowth fraction in Bi2212 with the intensity ratio  $\gamma$  ( $\gamma = \frac{I_{008}}{I_{0010}} \times 100\%$ ) of 008 and 0010 peaks of Bi2212 phase [38, 39]. According to this model, for a Bi2212 single crystal that contains fraction  $f$  of randomly distributed Bi2201 intergrowths, the average value  $\langle f(1-f) \rangle$  is inversely related to intensity ratio  $\gamma$ . If  $f < 0.5$ , the average value  $\langle f(1-f) \rangle$  increases monotonically with increasing  $f$ . Thus, for Bi2201 intergrowth  $f < 50\%$ , less Bi2201 intergrowth content should result in larger  $\gamma$ . Intensity ratio  $\gamma$  and  $f$ -values for samples II-1-6 are listed in Table 3-3. For samples II-1-4,  $\gamma$  ranges from 53-73 %, which, according to the correlation map in [39], the Bi2201 intergrowth fraction  $f$  ranges from 5% for II-4 to 11% for II-2. These values are similar to what Heeb et al. showed previously for a sample annealed at 850 °C for more than 80 hours [47], however, here the annealing was for only 48 hours. Therefore, with further increases in  $t_p$ , the fraction of Bi2201 may be reduced further [48]. Furthermore,  $f$ -values here are much less than the average values of a PMP Bi2212/Ag conductor, which range from 6.4% to 35%, explaining the absence of any observable 4413 phase peak. In addition, only a low content of Bi2201 half-cell intergrowths are observed in sample II-4 under STEM, indicating large Bi2201 grains either do not form or are converted to Bi2212 with higher  $T_p$  and longer  $t_p$ .

SEM images in Figure 2- 9 show that by increasing  $T_p$  from 845 °C to 855 °C, the grain size increases from 10-15  $\mu\text{m}$  to more than 20-25  $\mu\text{m}$ , a result of increased growth rate at elevated temperature. Closed-stacked Bi2212 grains are found when  $T_p$  reaches 855 °C (Figure 2- 9 (c-d)). Cross-sectional images for sample II-3 and 4 give a clearer view of layered Bi2212 grains and flakes. With a short  $t_p$ , porosity is favored between the Bi2212 flakes while with longer  $t_p$ , a more dense structure is formed.

### 3. Effects of varying the testing rate $R_1$

Samples II-5 and II-6 share the same  $T_{\text{ox}}=650$  °C,  $T_p=855$  °C,  $t_p$  and cooling rate (furnace cooled) as samples II-3 and II-4, but the heating rate  $R_1$  is decreased to from 200 °C/h to 60 °C/h. Magnetization results show that by decreasing  $R_1$ , there is a ~23% decrease in magnetic moment at 4.2 K. Again, there is no effect on  $T_c$ , indicating that the oxygen content is mostly influenced by  $T_p$ . The XRD results in Figure 3-7(b) show that with the lower  $R_1$ , the 008 (Bi2212) peak decreases, indicating more Bi2201 is formed. The  $\gamma$  values calculated for samples II-5 and II-6 are 49% and 50%, respectively, suggesting around 13-14% of Bi2201, significantly higher than samples II-3 and II-4. Furthermore, DTA curves in Figure 3-8(b) for samples II-5 and II-6 show additional peaks around the main melting peak, indicating reduced Bi2212 content when processed with lower  $R_1$ .

Although both Bi2201 and Bi2212 form in the temperature range 650 °C to 790 °C [37], Bi2201 is more stable than Bi2212 and thus preferred. Additionally, the stability range of Bi2201 is only slightly reduced by decreasing the oxygen partial pressure, but is further reduced by increasing the temperature [45]. Hence, with a lower heating rate, the time for heating is increased from 1.0 hour to 3.4 hours, allowing more time for Bi2201 formation and growth.

#### 4. Analysis of the pellet/Ag interface

Figure 3-11 shows that the Bi2212 grains at the Ag interface are much larger than those at the sample free surface. These grains are well connected, which is commonly observed in Ag-clad Bi2212 conductors after PMP [18, 49, 50]. In PMP Bi2212/Ag tapes, nucleation and grain alignment begin at the oxide/Ag interface [51]. Also, based on a grain alignment model developed by Buhl et al., Bi2212 grains bend during growth when they reach a Ag surface and turn parallel to the Ag surface [52].

Here, rapid diffusion at the pellet/Ag interface is the essential factor influencing Bi2212 formation and growth. The peak temperature is 845 °C for samples II-1 and II-2, which is nearly 30 °C below the melting temperature ( $876 \pm 1$  °C as determined by DTA), so the bulk does not melt during the heat treatment. A 5.2wt% silver addition to Bi2212 powders reduces the melt temperature by more than 20 °C [53]. Thus, in the region influenced by the Ag interface, the melting temperature of Bi2212 is at least 20 °C lower than in the bulk, ensuring rapid diffusion. Because the growth in the a-b plane direction is much faster than in the c-direction, very large platelet Bi2212 grains form at the interface. When dwelling at  $T_p$ , Bi2212 grains grow rapidly, reach the Ag interface, and then turn parallel to the Ag surface [52]. The smoothness of the Ag surface also influences Bi2212 grain orientation [54]. For the remainder of the pellet (which is not proximate to the Ag), the Bi2212 grains form and grow in colonies but without any alignment relative to the Ag sheath. With layer thickness greater than the grain size (about 150 μm), the colonies of Bi2212 grains are no longer parallel to the Ag substrate [55]. Also, the rest of the pellet is still nearly 30 °C lower than its melting temperature, so grain growth via diffusion is limited in solid state.

#### 5. Implications for MP Bi2212 wires

The results show several potential advantages of MP powders with a direct oxidation heat treatment over conventional OPIT with PMP. Several potential challenges must also be considered for wire processing.

Through mechanical alloying, MP powder can have a controllable stoichiometry and homogeneous elemental distribution. Composition is a potentially significant factor in future Bi2212 wire optimization. With sufficient intermittent scraping and optimized milling time, an elementally homogeneous MP powder with the desired stoichiometry can be obtained, avoiding phase segregation and inhomogeneous oxidation after heat treatment.

Results here show that by using a direct oxidation approach to forming Bi2212 grains without a partial melt, Bi2201 is the only phase impurity formed, and the Bi2201 content is much lower than in tapes and wires. Recent results indicate that although large Bi2201 grains reduce  $J_c$ , Bi2201 intergrowths within Bi2212 grains do not, and in fact may provide flux pinning [19, 56]. Through direct oxidation of MP, any CF or AEC grains that may form in the early stage of heat treatment are fully reacted, whereas this is not the case with PMP of oxide precursors. The solid-state reaction converting  $MP \rightarrow Bi2212$  also limits void agglomeration, a significant limiting factor for transport  $J_c$  in OPIT wire [57, 58].

Results here show that high density Bi2212 colonies are formed during the  $MP \rightarrow Bi2212$  transformation and that large, textured grains are aligned at the Ag interface. For multifilamentary wires with filament sizes between 10-30  $\mu m$ , highly aligned Bi2212 grains are expected after heat treatment.

One important issue for MP wires that has not been addressed here is the need for sufficient and rapid oxygen diffusion through the Ag sheath to ensure homogeneous oxidation and to avoid phase segregation. In the work reported here, the MP pellets have a free surface

exposed to the flowing oxygen, so even with a 10% oxygen atmosphere, access to oxygen is sufficient. In wires, the time constant for oxygen diffusion through the Ag sheath must be compared to that of solid-state metallic reactions and/or phase segregation within the precursor. This will require significant study with Ag-sheathed MP wires.

## **Conclusion**

A metallic precursor approach to synthesizing  $\text{Bi}_2\text{Sr}_2\text{CaCu}_2\text{O}_x$  is presented. A homogeneous MP with a controlled stoichiometry containing Bi, Sr, Ca, Cu, Ag, and/or its alloys is produced by mechanical alloying with intermittent scraping. Pressed pellets are formed and heat-treated with simple two-stage heat treatments. By introducing oxygen when Bi2212 starts to form and holding at an elevated temperature for a sufficient time, the MP oxidizes and transforms into Bi2212. A series of samples has been investigated based on chemical, thermal, microstructural, phase and magnetic property analysis to understand the preparation of MP and its conversion to Bi2212 under various heat treatment conditions. Since the peak temperature is at least 20 °C below the melting temperature, it is feasible to have Bi2201 as the only phase impurity after heat treatment, which is quite different from partial-melt processing of oxide precursors which results in AEC and CF phases as well. Several factors impacting the nucleation and growth of Bi2212 grains are discussed. Higher  $T_p$  and longer  $t_p$  facilitates conversion of MP to Bi2212 and a reduction of the Bi2201 content. The oxygen content is mostly influenced by  $T_p$ . Furthermore, higher  $T_p$  results in larger and denser Bi2212 grains. A faster heating rate  $R_1$  results in a shorter time between  $T_1$  and  $T_p$ , suppressing Bi2201 nucleation. Additionally, the microstructure at the sample/silver interface suggests larger size and preferred orientation of Bi2212 grains with the aid of a silver interface.

## **Acknowledgements**

The authors acknowledge the use of the Analytical Instrumentation Facility (AIF) at North Carolina State University, which is supported by the State of North Carolina and the National Science Foundation. The authors are grateful to Dr. Yi Liu, Golsa Naderi, Amir Kajbafvala (NCSU) and William Nachtrab (Supercon. Inc.) for assistance with this project.

## REFERENCES

- [1] A. Devred, *et al.*, "Future accelerator magnet needs," *Ieee Transactions on Applied Superconductivity*, vol. 15, pp. 1192-1199, Jun 2005.
- [2] L. Rossi, "Superconductivity: its role, its success and its setbacks in the Large Hadron Collider of CERN," *Superconductor Science & Technology*, vol. 23, Mar 2010.
- [3] S. A. Gourlay, *et al.*, "Magnet R&D for the US LHC Accelerator Research Program (LARP)," *Ieee Transactions on Applied Superconductivity*, vol. 16, pp. 324-327, Jun 2006.
- [4] J. Schwartz, *et al.*, "High Field Superconducting Solenoids Via High Temperature Superconductors," *Ieee Transactions on Applied Superconductivity*, vol. 18, pp. 70-81, 2008.
- [5] H. Kumakura, "Development of Bi-2212 conductors and magnets for high-magnetic-field generation," *Superconductor Science and Technology*, vol. 13, p. 34, 2000.
- [6] K. R. Marken, *et al.*, "Progress in Bi-2212 wires for high magnetic field applications," *Ieee Transactions on Applied Superconductivity*, vol. 16, pp. 992-995, Jun 2006.
- [7] W. T. Nachtrab, *et al.*, "Development of high superconductor fraction Bi<sub>2</sub>Sr<sub>2</sub>CaCu<sub>2</sub>O<sub>x</sub>/Ag wire for MRI," *Ieee Transactions on Applied Superconductivity*, vol. 18, pp. 1184-1187, Jun 2008.
- [8] T. D. Aksenova, *et al.*, "Texture Formation in Bi<sub>2</sub>Sr<sub>2</sub>Ca<sub>1</sub>Cu<sub>2</sub>O<sub>x</sub>/Ag Tapes Prepared By Thick Films," *Physica C*, vol. 205, pp. 271-279, Feb 1993.
- [9] T. Lang, *et al.*, "Phase assemblage and morphology during the partial melt processing of Bi-2212 thick films," *Physica C*, vol. 281, pp. 283-292, Aug 1997.
- [10] T. Lang, *et al.*, "Influence of the maximum temperature during partial melt-processing of Bi-2212 thick films on microstructure and j(c)," *Physica C*, vol. 294, pp. 7-16, Jan 1998.
- [11] W. T. Nachtrab, *et al.*, "Effect of Solidification Conditions on Partial Melt Processed Bi2212/Ag Round Wire," *Ieee Transactions on Applied Superconductivity*, vol. 21, pp. 2795-2799, Jun 2011.
- [12] K. Nomura, *et al.*, "Fabrication Conditions And Superconducting Properties Of Ag-sheathed Bi-Sr-Ca-Cu-O Tapes Prepared By Partial Melting And Slow Cooling Process," *Applied Physics Letters*, vol. 62, pp. 2131-2133, Apr 1993.

- [13] A. Polasek, *et al.*, "Partial Melt Processing of High-Tc Bulk Bi-2212 Starting from different Precursor Powders," in *8th European Conference on Applied Superconductivity*. vol. 97, S. Hoste and M. Ausloos, Eds., ed Bristol: Iop Publishing Ltd, 2008.
- [14] G. Naderi, *et al.*, "Understanding processing–microstructure–properties relationships in  $\text{Bi}_2\text{Sr}_2\text{CaCu}_2\text{O}_x/\text{Ag}$  round wires and enhanced transport through saw-tooth processing," *Superconductor Science and Technology*, vol. 26, p. 105010, 2013.
- [15] F. Kametani, *et al.*, "Bubble formation within filaments of melt-processed Bi2212 wires and its strongly negative effect on the critical current density," *Superconductor Science & Technology*, vol. 24, Jul 2011.
- [16] M. O. Rikel, *et al.*, "Competitiveness of porosity and phase purity in melt processed Bi2212/Ag conductors," *Physica C: Superconductivity*, vol. 354, pp. 321-326, 2001.
- [17] T. Hatano, *et al.*, "High-temperature X-ray Study of Melting and Solidification of the  $\text{Bi}_2\text{Sr}_2\text{CaCu}_2\text{O}_{8+\delta}$  on Silver," *Journal of Low Temperature Physics*, vol. 117, pp. 777-781, 1999.
- [18] W. Zhang and E. E. Hellstrom, "The development of an aligned microstructure during melt processing of  $\text{Bi}_2\text{Sr}_2\text{CaCu}_2\text{O}_x$  (BSCCO-2212) doctor-bladed films," *Physica C: Superconductivity*, vol. 218, pp. 141-152, 1993.
- [19] E. B. Callaway, *et al.*, "Statistical study of the relationship between electrical transport and filament microstructure in multifilamentary  $\text{Bi}_2\text{Sr}_2\text{CaCu}_2\text{O}_x/\text{Ag}/\text{Ag-Mg}$  round wires," *Superconductor Science & Technology*, vol. 27 (in press), 2014.
- [20] T. Shen, *et al.*, "Filament to filament bridging and its influence on developing high critical current density in multifilamentary  $\text{Bi}_2\text{Sr}_2\text{CaCu}_2\text{O}_x$  round wires," *Superconductor Science and Technology*, vol. 23, p. 025009, 2010.
- [21] P. Majewski, "BiSrCaCuO High-Tc Superconductors," *Advanced Materials*, vol. 6, pp. 460-469, 1994.
- [22] Q. Y. Hu, *et al.*, "Formation mechanism of high-Tc and critical current in  $(\text{Bi,Pb})_2\text{Sr}_2\text{Ca}_2\text{Cu}_3\text{O}_{10}/\text{Ag}$  tape," *Physica C: Superconductivity*, vol. 250, pp. 7-14, 1995.
- [23] J.-C. Grivel and R. Flükiger, "Formation mechanism of the Pb free  $\text{Bi}_2\text{Sr}_2\text{Ca}_2\text{Cu}_3\text{O}_{10}$  phase," *Superconductor Science and Technology*, vol. 11, p. 288, 1998.
- [24] P. E. D. Morgan, *et al.*, "Low level mobile liquid droplet mechanism allowing development of large platelets of high-Tc "Bi-2223" phase within a ceramic," *Physica C: Superconductivity*, vol. 176, pp. 279-284, 1991.

- [25] S. Bernik, "Synthesis and phase relations of the 110 K superconducting 2223 phase in the Bi-Pb-Sr-Ca-Cu-O system," *Superconductor Science and Technology*, vol. 10, p. 671, 1997.
- [26] P. Majewski, *et al.*, "The High-Tc superconducting solid solution  $\text{Bi}_{2+x}(\text{Sr,Ca})_3\text{Cu}_2\text{O}_{8+d}$  (2212 Phase)—chemical composition and superconducting properties," *Advanced Materials*, vol. 4, pp. 508-511, 1992.
- [27] P. Majewski, "Phase diagram studies in the system Bi-Pb-Sr-Ca-Cu-O-Ag," *Superconductor Science and Technology*, vol. 10, p. 453, 1997.
- [28] L. M. Rubin, *et al.*, "Phase stability limits of  $\text{Bi}_2\text{Sr}_2\text{Ca}_1\text{Cu}_2\text{O}_{8+\delta}$  and  $\text{Bi}_2\text{Sr}_2\text{Ca}_2\text{Cu}_3\text{O}_{10+\delta}$ ," *Applied Physics Letters*, vol. 61, pp. 1977-1979, 1992.
- [29] L. M. Rubin, *et al.*, "Phase stability limits and solid-state decomposition of  $\text{Bi}_2\text{Sr}_2\text{CaCu}_2\text{O}_{8+\delta}$  and  $\text{Bi}_2\text{Sr}_2\text{Ca}_2\text{Cu}_3\text{O}_{10+\delta}$  in reduced oxygen pressures," *Physica C: Superconductivity*, vol. 217, pp. 227-234, 1993.
- [30] A. P. Mozhaev, *et al.*, "Phase stability, oxygen nonstoichiometry, and superconductivity properties of  $\text{Bi}_2\text{Sr}_2\text{CaCu}_2\text{O}_{8+\delta}$  and  $\text{Bi}_{1.8}\text{Pb}_{0.4}\text{Sr}_2\text{Ca}_2\text{Cu}_3\text{O}_{10+\delta}$ ," *Journal of Solid State Chemistry*, vol. 119, pp. 120-124, 1995.
- [31] P. Majewski, *et al.*, "Cu diffusion into Ag during BSCCO tape processing," *Physica C: Superconductivity*, vol. 351, pp. 62-66, 2001.
- [32] E. E. Hellstrom and W. Zhang, "Formation and prevention of bubbles when melt processing Ag-sheathed  $\text{Bi}_2\text{Sr}_2\text{CaCu}_2\text{O}_x$  (2212) conductors," *Superconductor Science and Technology*, vol. 8, p. 317, 1995.
- [33] W. Zhang and E. E. Hellstrom, "The influence of carbon on melt processing Ag sheathed  $\text{Bi}_2\text{Sr}_2\text{CaCu}_2\text{O}_8$  tape," *Physica C: Superconductivity*, vol. 234, pp. 137-145, 1994.
- [34] L. Margulies, *et al.*, "The effect of carbon on the peritectic melting of Bi2212 and  $\text{Bi}_{2212} + \text{Ag}$ ," *Physica C: Superconductivity*, vol. 264, pp. 133-136, 1996.
- [35] W. Lo and B. A. Glowacki, "A study of the formation processes of the 2212 phase in the Bi-based superconductor systems," *Physica C: Superconductivity*, vol. 193, pp. 253-263, 1992.
- [36] T. G. Holesinger, *et al.*, "Solid-Solution Region Of the  $\text{Bi}_2\text{Sr}_2\text{CaCu}_2\text{O}_y$  Superconductor," *Physica C*, vol. 217, pp. 85-96, Nov 1993.
- [37] T. G. Holesinger, *et al.*, "Isothermal Melt Processing Of  $\text{Bi}_2\text{Sr}_2\text{CaCu}_2\text{O}_{-\gamma}$  Round Wire," *Physica C*, vol. 253, pp. 182-190, Oct 1995.

- [38] J. M. Tarascon, *et al.*, "Preparation, structure, and properties of the superconducting compound series  $\text{Bi}_2\text{Sr}_2\text{Ca}_{n-1}\text{Cu}_n\text{O}_y$  with  $n=1,2$ , and  $3$ ," *Physical Review B*, vol. 38, pp. 8885-8892, 1988.
- [39] M. O. Rikel and E. E. Hellstrom, "Development of 2201 intergrowths during melt processing  $\text{Bi}2212/\text{Ag}$  conductors," *Physica C: Superconductivity*, vol. 357-360, Part 2, pp. 1081-1090, 2001.
- [40] H. Ota, *et al.*, "Formation of phase intergrowth in the syntheses of Bi-superconducting thin films," *Applied Physics Letters*, vol. 70, pp. 1471-1473, 1997.
- [41] J. S. Luo, *et al.*, "Phase chemistry and microstructure evolution in silver-clad  $(\text{Bi}_{2-x}\text{Pb}_x)\text{Sr}_2\text{Ca}_2\text{Cu}_3\text{O}_y$  wires," *Ieee Transactions on Applied Superconductivity*, vol. 3, pp. 972-975, 1993.
- [42] G. Triscone, *et al.*, "Variation of the superconducting properties of  $\text{Bi}_2\text{Sr}_2\text{CaCu}_2\text{O}_{8+x}$  with oxygen content," *Physica C: Superconductivity*, vol. 176, pp. 247-256, 1991.
- [43] J. H. P. M. Emmen, *et al.*, "Crystal growth and annealing experiments of the high  $T_c$  superconductor  $\text{Bi}_2\text{Sr}_2\text{CaCu}_2\text{O}_{8+\delta}$ ," *Journal of Crystal Growth*, vol. 118, pp. 477-482, 1992.
- [44] P. Majewski, *et al.*, "The oxygen content of the high-temperature superconducting compound  $\text{Bi}_{2+x}\text{Sr}_{3-y}\text{Ca}_y\text{Cu}_2\text{O}_{8+d}$  as a function of the cation concentration," *Physica C: Superconductivity*, vol. 229, pp. 12-16, 1994.
- [45] D. Sager, *et al.*, "Enhanced residual secondary phase dissolution by atmosphere control in Bi-2212 superconductors," *Physica C: Superconductivity*, vol. 405, pp. 103-116, 2004.
- [46] H. Heinrich, *et al.*, "HREM observation of stacking sequences in bulk Bi-Sr-Ca-Cu-O superconductors and identification of phases by ED and EDX," *Ultramicroscopy*, vol. 49, pp. 265-272, 1993.
- [47] B. Heeb, *et al.*, "From Imperfect To Perfect  $\text{Bi}_2\text{Sr}_2\text{CaCu}_2\text{O}_x$  (Bi-2212) Grains," *Journal of Materials Research*, vol. 8, pp. 2170-2176, Sep 1993.
- [48] M. M. Matthiesen, *et al.*, "The effects of anneal time and cooling rate on the formation and texture of  $\text{Bi}_2\text{Sr}_2\text{CaCu}_2\text{O}_8$  films," *Ieee Transactions on Magnetics*, vol. 27, pp. 1223-1226, 1991.
- [49] E. Cecchetti, *et al.*, "A model for texture development in BSCCO high-  $T_c$  superconductors," *Superconductor Science and Technology*, vol. 13, p. 1270, 2000.
- [50] D. R. Dietderich, *et al.*, "Textured Thick-films of  $\text{Bi}_2\text{Sr}_2\text{Ca}_1\text{Cu}_2\text{O}_x$ ," *Japanese Journal of Applied Physics Part 2-Letters*, vol. 29, pp. L1100-L1103, Jul 1990.

- [51] T. G. Holesinger, *et al.*, "Directional isothermal growth of highly textured Bi(2212)," *Applied Physics Letters*, vol. 63, pp. 982-984, Aug 1993.
- [52] D. Buhl, *et al.*, "Texture in Melt-Processed Bi-2212," *Journal of Electroceramics*, vol. 1, pp. 133-144, 1997/09/01 1997.
- [53] T. Lang, *et al.*, "Melting of Bi-2212 under controlled oxygen partial pressures with silver," *Physica C: Superconductivity*, vol. 275, pp. 284-292, 1997.
- [54] H. Kumakura, *et al.*, "Influence of Ag substrates on grain alignment and critical current density of Bi-2212 tape conductors," *Ieee Transactions on Applied Superconductivity*, vol. 9, pp. 1804-1807, 1999.
- [55] D. Buhl, *et al.*, "Phase composition and grain alignment in partial melt processed Bi-2212 thick films," *Ieee transaction of Applied Superconductivity*, vol. 4, pp. 299-317, 1996.
- [56] G. Naderi and J. Schwartz, "On the role of Bi<sub>2</sub>Sr<sub>2</sub>CuO<sub>x</sub> intergrowths in Bi<sub>2</sub>Sr<sub>2</sub>CaCu<sub>2</sub>O<sub>x</sub>/Ag round wire transport," *Nature Materials*, 2014 (submitted).
- [57] C. Scheuerlein, *et al.*, "Void and phase evolution during the processing of Bi-2212 superconducting wires monitored by combined fast synchrotron micro-tomography and x-ray diffraction," *Superconductor Science and Technology*, vol. 24, p. 115004, 2011.
- [58] J. Jiang, *et al.*, "Doubled critical current density in Bi-2212 round wires by reduction of the residual bubble density," *Superconductor Science and Technology*, vol. 24, p. 082001, 2011.

**STUDIES ON MULTIFILAMENTARY  $\text{Bi}_2\text{Sr}_2\text{CaCu}_2\text{O}_x/\text{Ag}$  WIRE FORMED VIA  
A METALLIC PRECURSOR POWDER-IN-TUBE PROCESS**

Yun Zhang, Carl C. Koch, Justin Schwartz

*Department of Materials Science and Engineering*

*North Carolina State University, Raleigh, NC 27695*

**Abstract**

Previously, a metallic precursor approach to synthesizing  $\text{Bi}_2\text{Sr}_2\text{CaCu}_2\text{O}_x$  (Bi2212), with a homogeneous mixture of Bi, Sr, Ca, Cu and Ag was produced by mechanical alloying. Here, Bi2212/Ag round multifilamentary wire is manufactured using a metallic precursor powder-in-tube (MPIT) process. The metallic precursor powders were packed into a pure Ag tube in an Ar atmosphere and then sealed. After deformation, the multifilamentary round wires and rolled tapes were heat treated in flowing oxygen through three stages: oxidation, conversion and partial-melt processing (PMP). Processing-microstructure-property relationships on 20 mm-50 mm long multifilamentary round wires and rolled tapes were extensively studied. It is found that the first heat treatment stage, the oxidation stage, plays a crucial role in chemical homogeneity, phase transformation, microstructure evolution and conductor performance. Three pathways of MP oxidation are discussed in Ag-sheathed MPIT wires. Furthermore, it is found the Bi2212 grain alignment within an MPIT filament is significantly different from that found in OPIT filaments after partial-melt processing, indicating the formation of highly dense filaments containing Bi2212 fine grains and Ag particles before PMP aids the formation of large, c-axis textured Bi2212 filaments during PMP.

**Keywords:** Bi2212, superconductor, metallic precursor, oxidation, phase transformation, critical current density

## Introduction

A superconducting conductor capable of generating magnetic fields above 30 T is needed for future high field magnets for a high energy large hadron collider, a muon collider and high field nuclear magnetic resonance [1]. The upper critical fields of low temperature superconductors (LTS) such as NbTi and Nb<sub>3</sub>Sn limit the maximum magnetic fields that can be generated to about 10.5 T and 20 T [2-4]. High temperature superconductors, such as REBa<sub>2</sub>Cu<sub>3</sub>O<sub>7-x</sub> (REBCO) and Bi<sub>2</sub>Sr<sub>2</sub>CaCu<sub>2</sub>O<sub>x</sub> (Bi2212) with upper critical field greater than 100 T, are promising candidates [5-7]. As the only high field superconductor available as an isotropic round wire, Bi2212/Ag/Ag-alloy sheathed wires are of particular interest [8].

Currently, Bi2212/Ag wires are manufactured via the oxide-powder-in-tube (OPIT) route by filling Ag tubes with Bi2212 oxide precursor, deforming into wire, restacking (sometimes twice) into Ag or Ag-alloy tube and heat treating using partial-melt processing. During the partial-melt, Bi2212 powder melts incongruently, forming several non-superconducting crystalline phases and a liquid phase, which partially convert to Bi2212 during subsequent cooling [9, 10].

Although a variety of approaches are used to synthesize oxide precursors [11-19], the OPIT route has important shortcomings that limit the final Bi2212 wire performance. Bubbles and voids form and evolve during partial melt because of low tap density of the green wire and carbon residue in the Bi2212 oxide precursor [20-26]. Recently, over-pressure (OP) processing has effectively reduced gross microstructural porosity in Bi2212 wire, resulting in greatly increased  $J_c$  [1]. But, even with OP processing, 100% theoretical density is not obtained in the filaments, and further densification is likely to result in even great improvements in wire  $J_c$  [27]. It is also unclear how to translate increased wire  $J_c$  by OP into

improved wind-and-react magnets. Another challenge facing Bi2212 for high field superconducting magnets is poor electromechanical performance. High field superconducting magnets experience large Lorentz forces and thus strain tolerance is an important characteristic for high field conductors [28, 29]. There is evidence of an electrical “backbone” in Bi2212 round wires with significantly higher strain tolerance and reversible behavior, and improving the filament density by eliminating porosity and non-superconducting phases is may improve the strain tolerance by increasing the volume fraction of the strong backbone [30-32]. A recent study by Godeke et al. found that OP processing does not increase the linear reversible strain (0.3% strain) relative to more porous, conventionally processed Bi2212 wires. In fact, the irreversible reduction in  $J_c$  for wires densified by OP processing may be even larger than non-densified wires [33]. This may be a result of trapped gas within the filament during OP processing.

An alternative to the oxide precursor route, with the potential to address these issues, is metallic precursors (MP) that are oxidized after wire deformation. Previously, metallic precursors were studied for Ag-sheathed  $\text{Bi}_2\text{Sr}_2\text{Ca}_2\text{Cu}_3\text{O}_x$  (Bi2223) multifilamentary tapes and Bi2212 monofilamentary tapes [34-37]. Starting with ductile metallic precursors, a relatively smooth interface between the filaments and Ag sheath and fine filaments (as small as 5  $\mu\text{m}$ ) were achieved in multifilamentary Bi2223 tapes [34-36]. After heat treatment, the Bi2223 tapes were flexible and ductile with the high strain tolerance required for large-scale use [34]. In addition, a monofilamentary Bi2212/Ag tape was made via solid metal-bearing precursor route [37]. Mixed  $\text{Bi}_2\text{O}_3$ , Sr, Ca and Cu powders were synthesized by mechanical alloying and filled into a Ag tube. After deformation and rolling, the tapes were 150-500  $\mu\text{m}$  thick with a core thickness of 50-160  $\mu\text{m}$ . The Ag along the side edges of the tapes was

removed to facilitate oxidation. After oxidation and partial-melt in flowing oxygen, the resulting tapes exhibited average  $J_c$  of 320 A/mm<sup>2</sup> at 4.2 K, self-field. But the samples were only 10 mm-20 mm in length and with one side of the Ag sheath removed. This investigation did not study the influence of a closed Ag-sheath or long length oxidation [37].

The current work focuses on the processing-microstructure relationships on Ag-sheathed multifilamentary Bi2212 round wires and rolled tapes with sample lengths of 20 - 50 mm. A series of heat treatments, including oxidation, conversion to Bi2212 and partial-melt processing are performed. Elemental distribution, phase transformation and microstructure evolution are extensively studied along the length of round wires and rolled tapes. Factors that affect oxidation mechanisms, Bi2212 conversion and grain alignment are discussed.

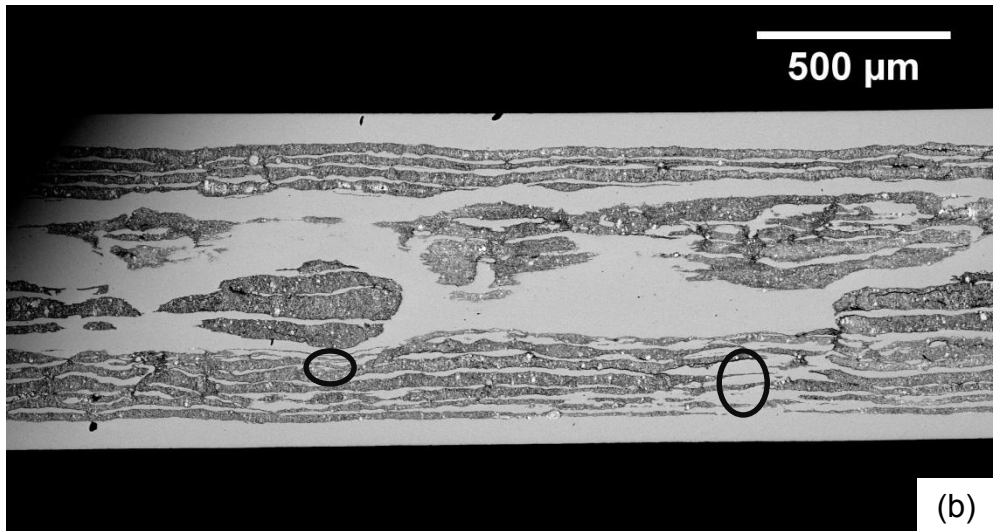
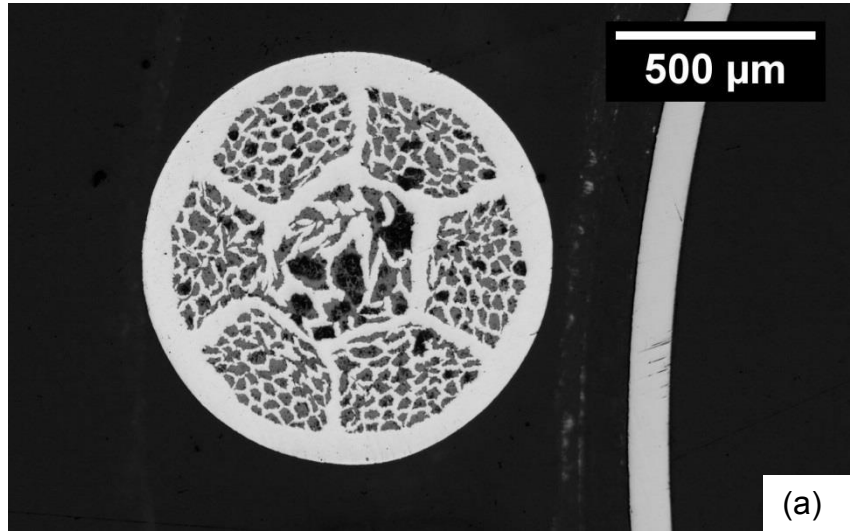
## **Experimental approach**

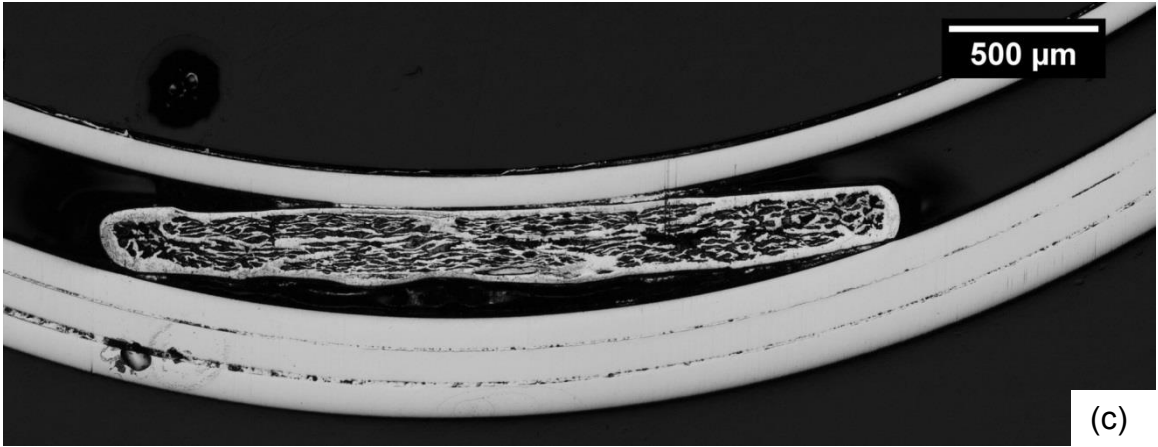
### Sample preparation

Metallic precursor powders were synthesized by mechanical alloying with intermittent scraping. Extensive details of this process were reported previously [38]. The cation stoichiometry of the MP powder is  $\text{Bi}_{2.19}\text{Sr}_{1.87}\text{Ca}_{1.13}\text{Cu}_{2.00}$  and it is mixed with 1.94 wt% of Ag powder. Around 100 gm of MP powders were packed into a pure Ag tube in an Ar atmosphere. The MP powder was tapped with a tungsten rod down the Ag tube on a vibration table and then sealed. The monofilamentary tube was converted to a double-rotate multifilamentary round wire by Supercon Inc. via the same procedures used for their oxide-powder-in-tube (OPIT) wires. The as-drawn multifilamentary wire is shown in Figure 4-1. The 1.05 mm diameter wire contains 7 bundles; the outer 6 bundles have 55 filaments ranging in size from 25  $\mu\text{m}$  to 40  $\mu\text{m}$ . The overall fill factor is 30%. The central bundle of filaments was damaged during deformation and macroscopically disconnected during

drawing. Furthermore, every filament in the outer bundles contains regions with severe necking along the wire as circled, which limits the effective filament area for transport. Thus, an effective fill factor is introduced by taking account the significant reduction in the mesoscopically in-tact filament cross-sectional area. By multiplying the necking thickness and filament counts in the outer bundles, an effective fill factor of 5% is calculated. Some of the round wire was subsequently cold-rolled into flat tapes to reduce the Ag sheath thickness and filament size, as shown in Figure 4-1c. The cross-sectional area of the rolled tape before heat treatment is  $0.5733 \text{ mm}^2$ .

Figure 4- 1 Images of green multifilamentary wire before heat treatment (a) round wire cross-sectional image, (b) round wire longitudinal image and (c) rolled tape cross-sectional image.

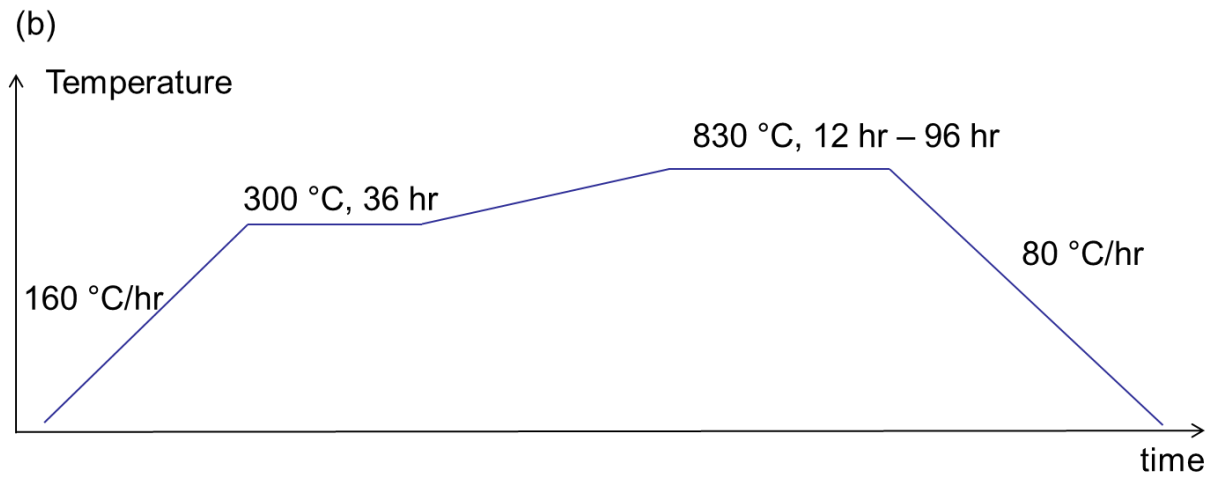
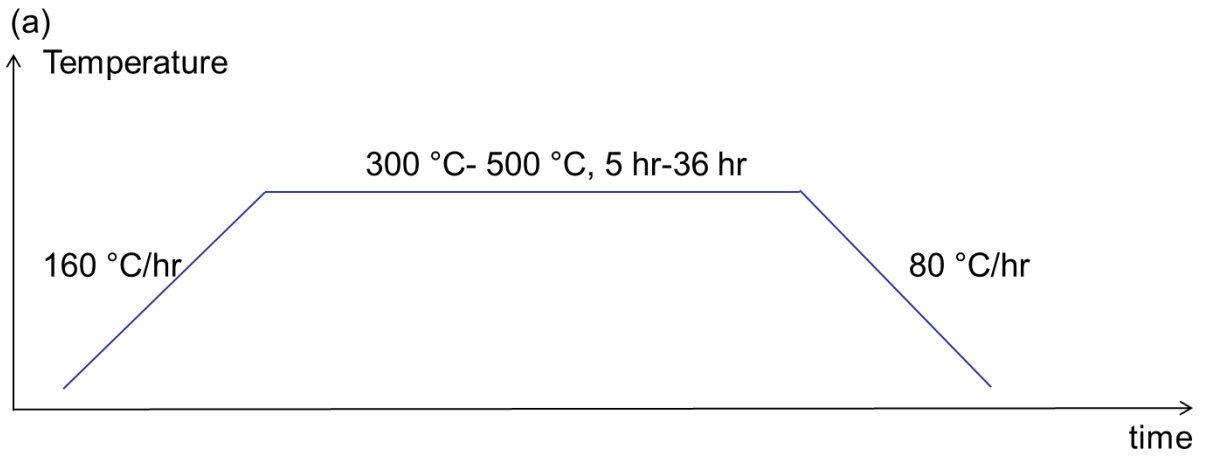


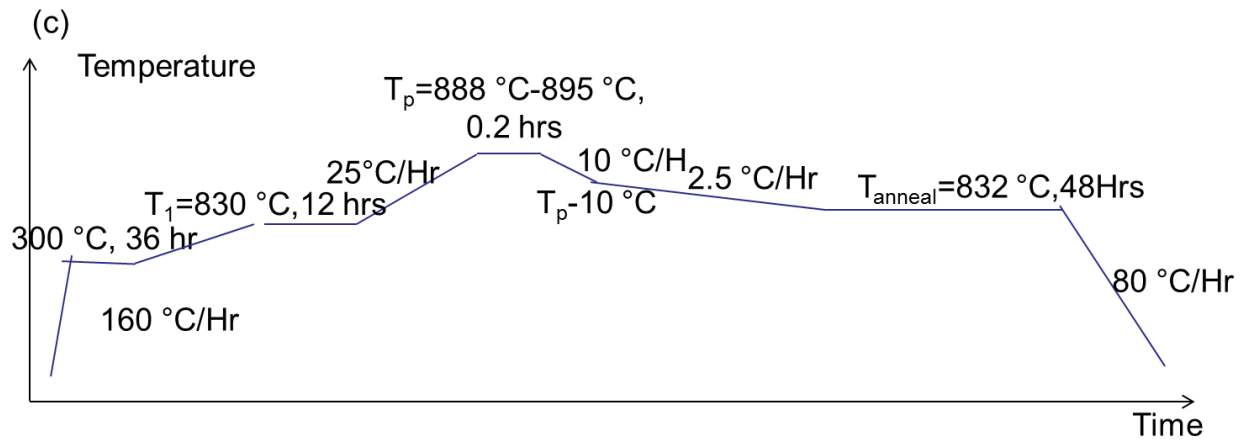


### Heat treatment

Three-stage heat treatments were performed on wires and tapes; the first stage oxidizes the metallic precursors to sub-oxides, the second stage converts the sub-oxides to the Bi2212 phase, and the third stage is partial-melt processing to increase grain connectivity and texture of the Bi2212 filaments. All heat treatments were performed in 1 atm flowing oxygen. Schematic heat treatment profiles are illustrated in Figure 4-2.

Figure 4-2 Heat treatment profiles for (a) stage 1: oxidation (b) stage 1+2: oxidation + conversion (c) complete heat treatment: oxidation, conversion and PMP.





To investigate the microstructural evolution, phase transformations and elemental homogeneity after oxidation and conversion stages, several 20 mm-long samples were used to undergo oxidation-only (Figure 4-2a) or oxidation+conversion (Figure 4-2b) heat treatments and analyzed. Oxidation heat treatments on wires were performed at 300 °C-500 °C for 5 hrs -36 hrs. After low temperature oxidation, conversion heat treatments were performed at 830 °C for 12-96 hrs to convert the sub-oxides into the Bi2212 phase. Finally, 50 mm-long samples were heat treated for all three stages, oxidation, conversion and partial-melt processing (Figure 4-2c). The peak temperature ranges from 888 °C - 895 °C.

#### Characterization

Inductively-coupled-plasma emission spectroscopy (ICP-ES, Perkin Elmer 2000 Dual View spectrometer) was used to determine the stoichiometry of MP powders. Samples were weighed on Teflon microwave digest sample holders to the nearest  $10^{-5}$  g. 5 mL of 4:1 ([conc. HCl]: [conc. HNO<sub>3</sub>]) was then added to each sample. The solution then sat for 48 hrs before measurements.

A Hitachi TM3000 and a JEOL 6010LA scanning electron microscopes (SEM) with energy dispersive spectrometry (EDS) were used to examine the microstructures and homogeneity of the elemental distribution of wires and tapes, before and after heat treatments. For outer surface analysis, the sample was taped with a carbon film on stage. For analysis of internal microstructures, samples were longitudinally or cross-sectionally mounted and polished.

Imaging and EDS mapping were performed along the different sections of the wires/tapes to reveal the microstructural differences.

Self-field critical current ( $I_c$ ) was measured using the four-point-probe method in liquid helium (4.2 K). For 50 mm-long samples, two sets of voltage taps were used to investigate the sample homogeneity: One set was in the middle section of the wire (VT-1) and the other 10 mm away from the end (VT-2); this is illustrated in Figure 4-3. A  $1 \mu\text{V}/\text{cm}$  electric-field criterion was used to determine  $I_c$ . Critical current density ( $J_c$ ) is calculated by dividing  $I_c$  by the multiplier of the cross-sectional area and fill factor of the green wire or tape.

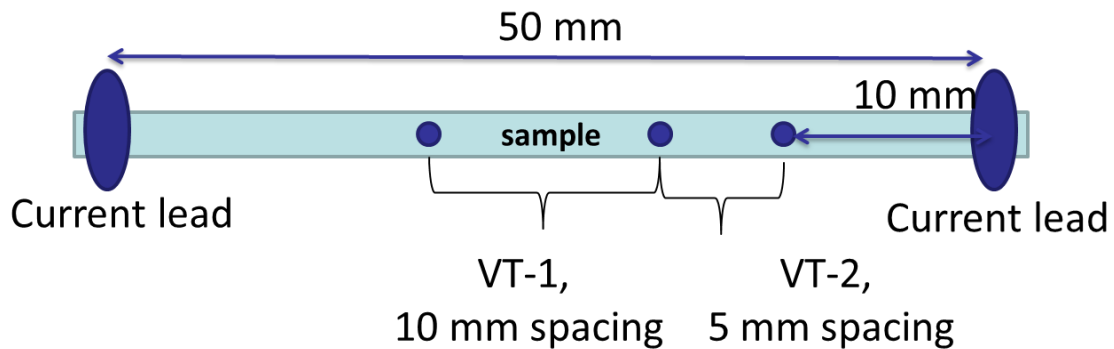


Figure 4-3 Schematic drawing of critical current measurements setup on 50 mm-long samples.

## Results

The cation stoichiometry of the metallic precursor, as measured by ICP-ES, is Bi:Sr:Ca:Cu = 2.19:1.87:1.13:2.00, with 1.94 wt% of Ag. Note that Zr contamination from the ZrO<sub>2</sub> milling media is not found in the milled MP powder. Figure 4-4 shows an SEM micrograph and corresponding EDS maps of the elemental distributions of Bi, Sr, Ca, Cu and Ag in a longitudinally polished round wire before heat treatment; a homogeneous distribution of elements is observed. No extensive agglomeration or welding of powder is found in the milled MP powders; note that the largest particles are Sr particles of 5 μm and less, and the other particles are less than 2 μm.

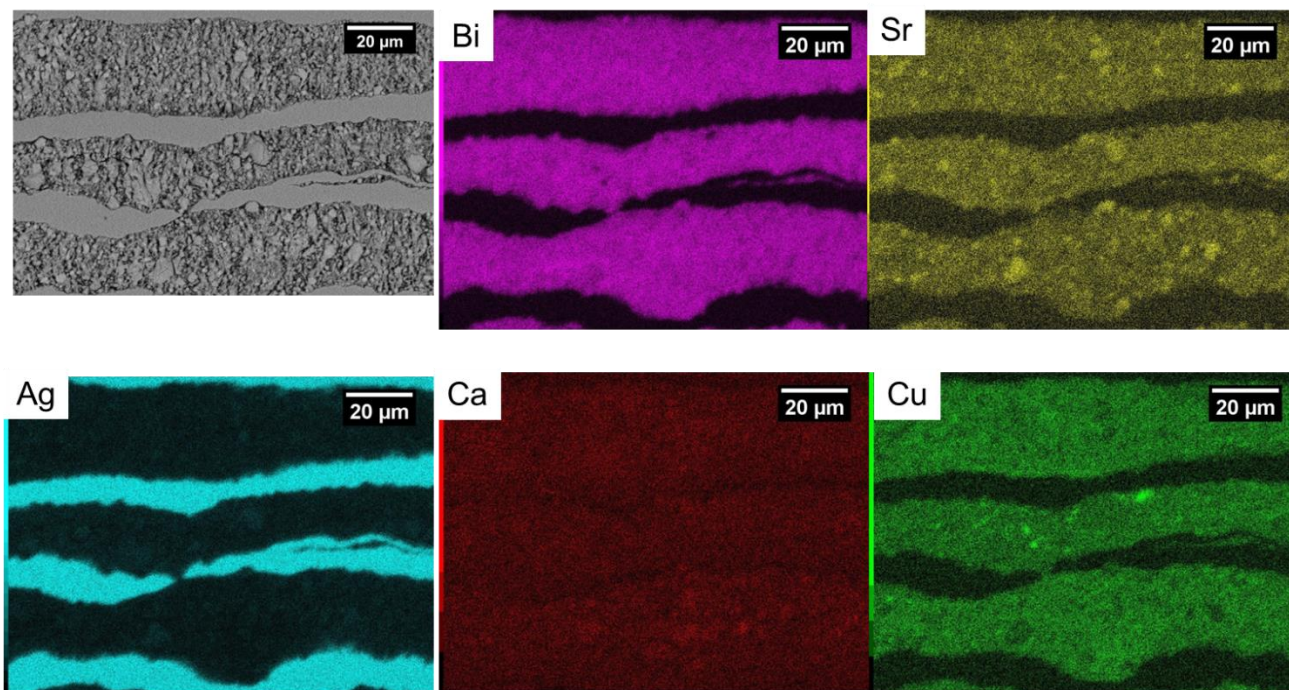


Figure 4-4 SEM image and EDS maps showing the MP elemental distribution after deformation and before heat treatment.

Figure 4-5 shows SEM images of the round wire surface after oxidation at 300 °C for 5 hrs. A crack is observed along the wire axis and is surrounded by a bright, rough area. EDS shows that the bright area is Bi, indicating Bi diffused from the filaments and concentrated on the wire/atmosphere free surface. With 500 °C oxidation for 5 hrs, the number of cracks increases, as does the amount of Bi on the surface.

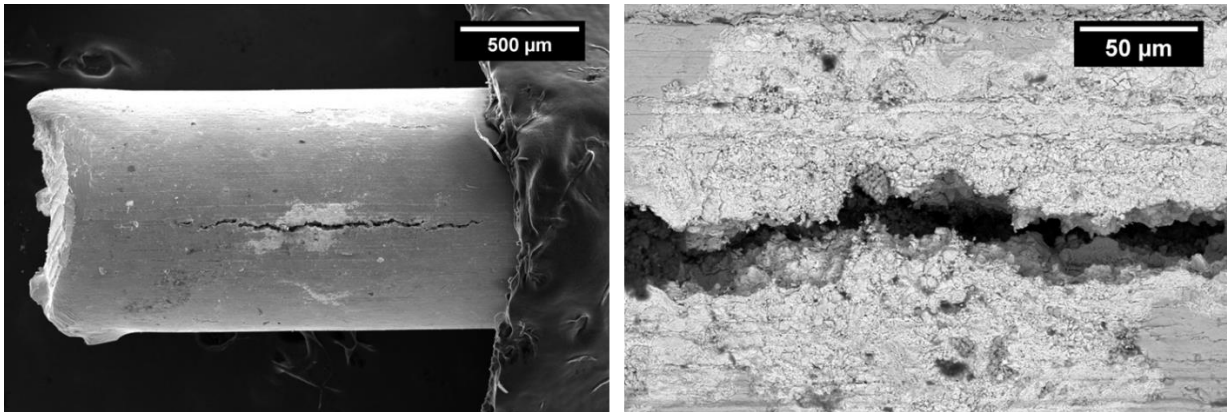


Figure 4-5 SEM images of round wire surface after oxidation. Note that a crack along the wire axis was found on the surface, along with a layer of Bi.

In Figure 4-6, SEM images of a longitudinally-polished round wire after 500 °C oxidation for 5 hrs are shown. The entire 20 mm length of wire is imaged. Two major cracks are observed in the middle, 5 mm-long section of the sample. Detailed filament microstructures and Bi distributions after oxidation are shown in Figure 4-7. At 1 mm from the left end of the wire,

the metallic precursors are oxidized completely, with no reaction between the Ag sheath and those filaments. The Bi concentration within the filament is 30.8 mol% by EDS (Bi mol% + Sr mol% + Ca mol% + Cu mol% = 100 mol%). At 5 mm from the left end, the Bi has migrated from the filament to the Ag sheath and segregated at Ag/filament interface. The Bi concentration in the square spot in Figure 4-7d is 37.0 mol%. At 9 mm from the left end and above crack 1, the Bi concentration within the filament decreased to 22.6 mol%, indicating significant Bi loss from the filament in the middle section of the wire.

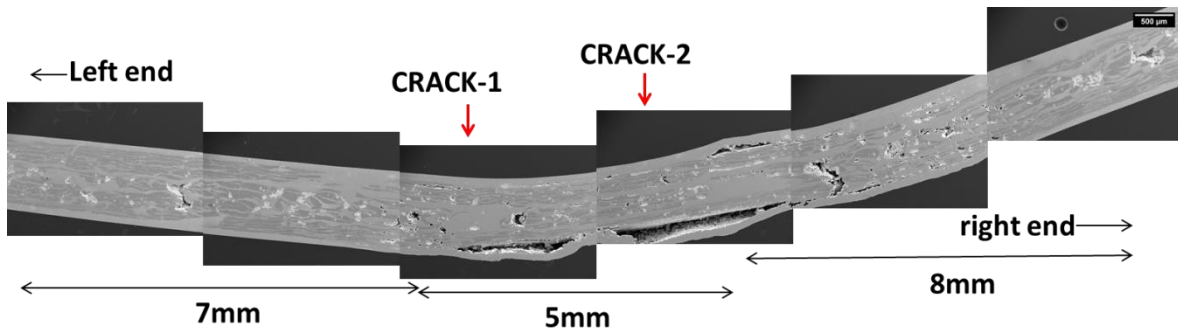


Figure 4-6 SEM images of a 20 mm long longitudinally polished wire after oxidation.

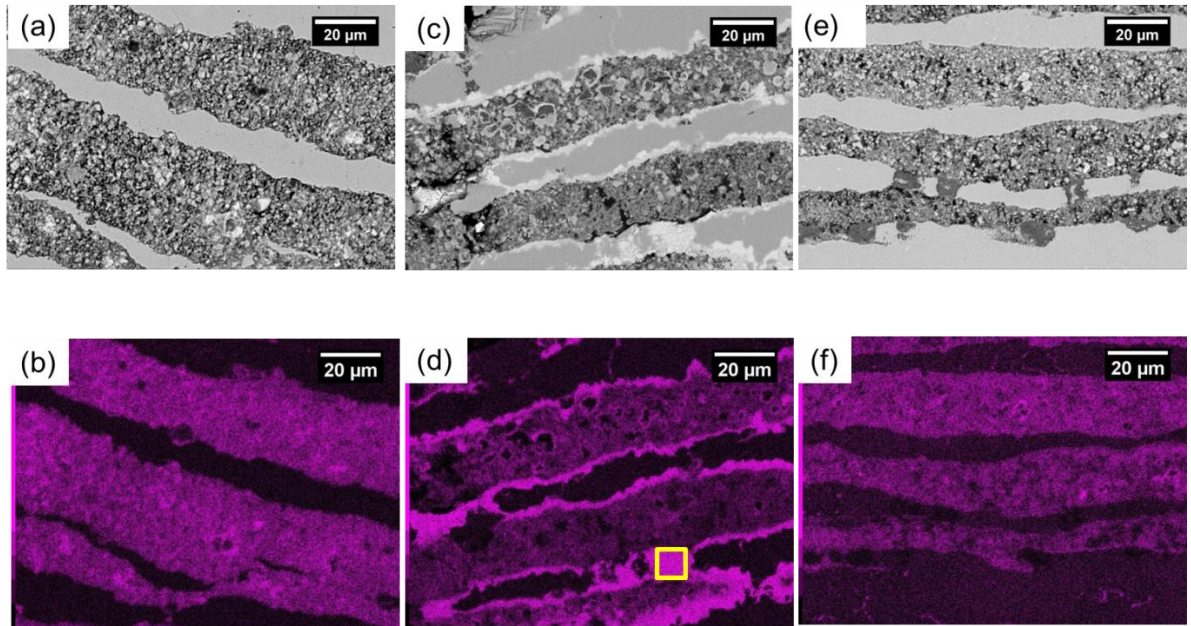


Figure 4-7 SEM images and corresponding EDS maps of the Bi distribution

(a,b) 1 mm from the left end, (c,d) 5 mm from the end and (e,f) 9 mm from the left end, after 500 °C – 5 hr oxidation.

SEM images in Figure 4-8 show that Bi from the filaments in the middle section migrates and concentrates at the wire/atmosphere free surface. The surface morphology indicates a Bi-rich liquid, resulting in an uneven Ag/filament interface and wire/atmosphere free surface. With an oxidation time of 5 hrs, which is insufficient for complete oxidation, the wire bent during cooling due to differences in the thermal expansion coefficients. With an oxidation

time of 36 hrs, the wire remains straight. The crack and rugged filament/Ag interface are still observed, indicating that the liquid formed is oxidized with increased oxidation time.

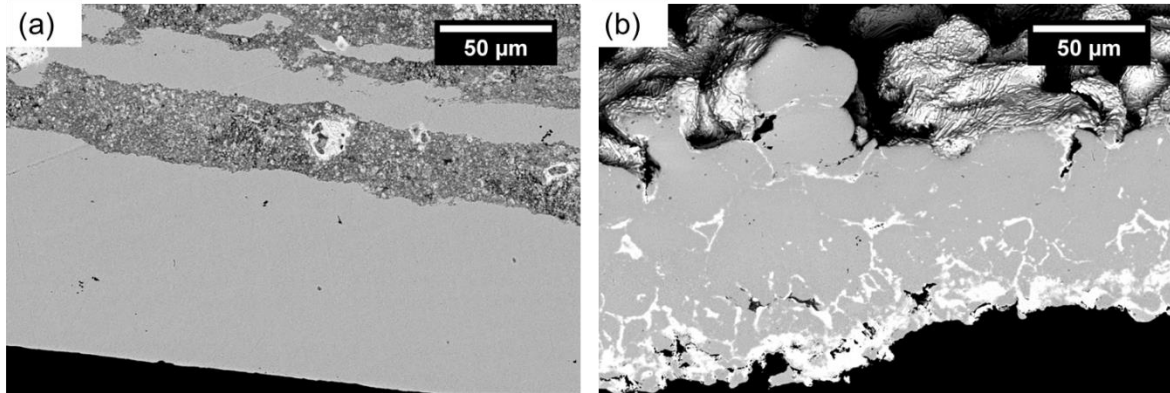


Figure 4-8 SEM images of the outer Ag surface at wire sections (a) 1 mm from the left end (b) 9 mm from the left end, below crack 1.

The SEM images and corresponding EDS maps shown in Figure 4-9 indicate the pathway of Bi migration from each filament to the wire/atmosphere free surface is through the Ag grain boundaries. Significant Bi is concentrated at the Ag grain boundaries and the grain boundary triple junctions, indicating that a Bi-rich liquid infiltrates these Ag grain boundaries, migrates towards the incoming oxygen and concentrates at the wire/atmosphere free surface.

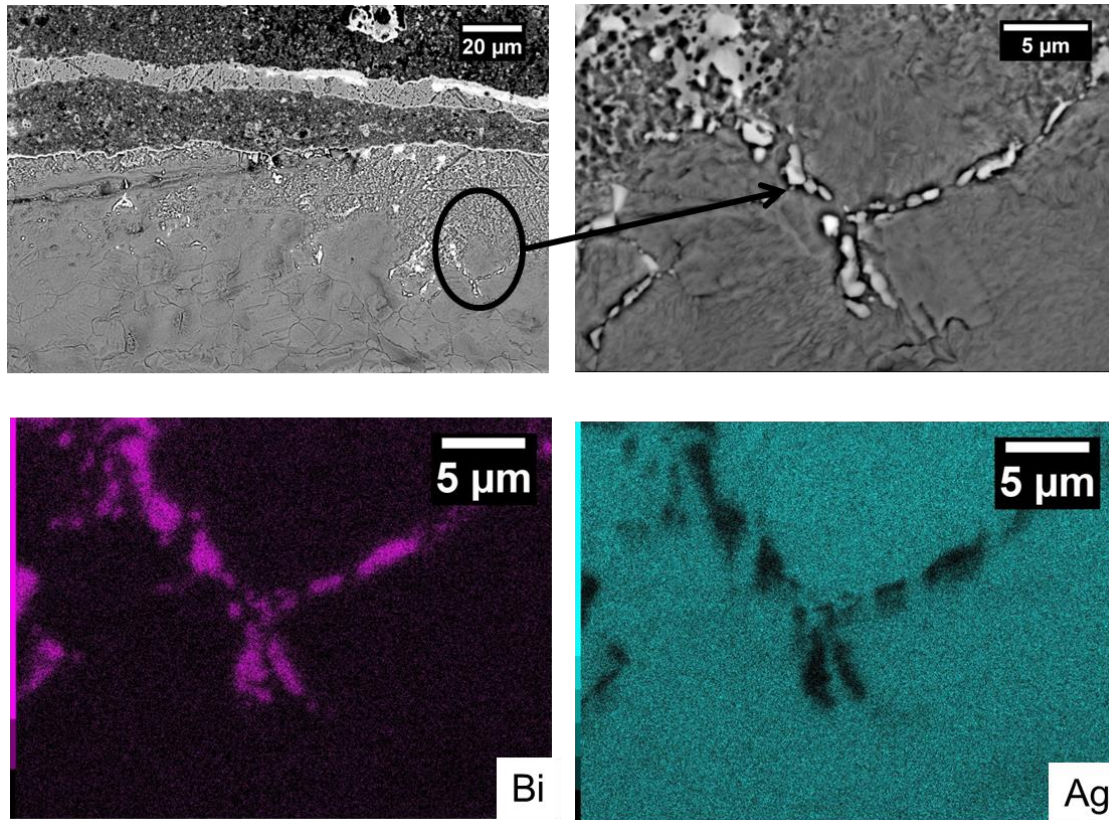


Figure 4-9 SEM images and corresponding EDS maps showing Bi concentration in Ag grain boundaries.

SEM images of longitudinally polished rolled tapes are shown in Figure 4-10. The total length of the rolled tape is 20 mm, same as the oxidized round wire seen in Figure 4-6. Bright areas seen on the Ag sheath indicate a Bi-rich liquid is observed 5 mm from the left end, and the amount of Bi increases at 12 mm from the left end (middle section of the tape). But the total amount of Bi in the Ag is significantly lower than in round wire, and even in the middle section of the wire, the Bi-rich liquid does not reach the wire/atmosphere free surface. These results indicate that with a thinner Ag thickness; 17 - 20  $\mu\text{m}$  for rolled tapes compared with

65 - 85  $\mu\text{m}$  for round wire, oxygen permeation through the Ag sheath requires less time and thus the MP powders is oxidized faster, suppressing Bi migration through Ag grain boundaries.

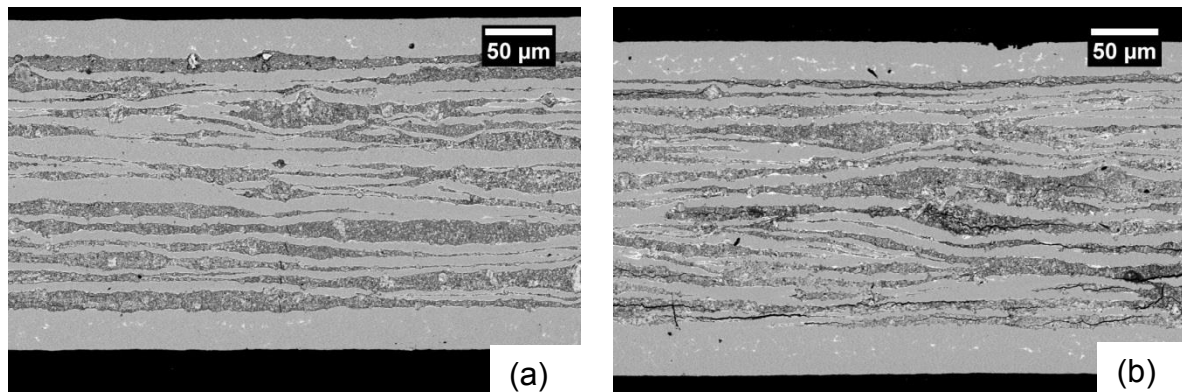


Figure 4-10 SEM images of longitudinally polished rolled tapes after oxidation: (a) 5 mm from the left end and (b) 12 mm from the left end.

Figure 4-11 shows the microstructure of a longitudinally polished round wire after oxidation and conversion heat treatment. Comparing the microstructures at different sections, i.e. near the left end of wire and in the middle section of the wire, shows that the phase transformations during the conversion heat treatment depend on the microstructure and elemental distribution after the oxidation stage. Near the end of the wire, dense filaments are formed containing Bi2212 grains along with  $(\text{Ca},\text{Sr})\text{O}_x$  and AEC phases at the Ag/filament interface. Small Ag particles are observed within the filament between the Bi2212 grains. No porosity is observed within the filament. This microstructure is significantly different from OPIT green wire before PMP, where 20 – 30% porosity remains. In the middle section of the

wire, however, the filaments have significant porosity and few Bi2212 grains are observed. With Bi depletion and porosity formed during the oxidation stage, Bi2212 formation in the middle section of the wire is limited. In addition, with increasing time at 830 °C, from 12 hrs to 96 hrs, no significant difference in microstructure or phase assemblage is observed, indicating that the conversion from sub-oxides to Bi2212 is fast where the oxidation is thorough and all cations are present.

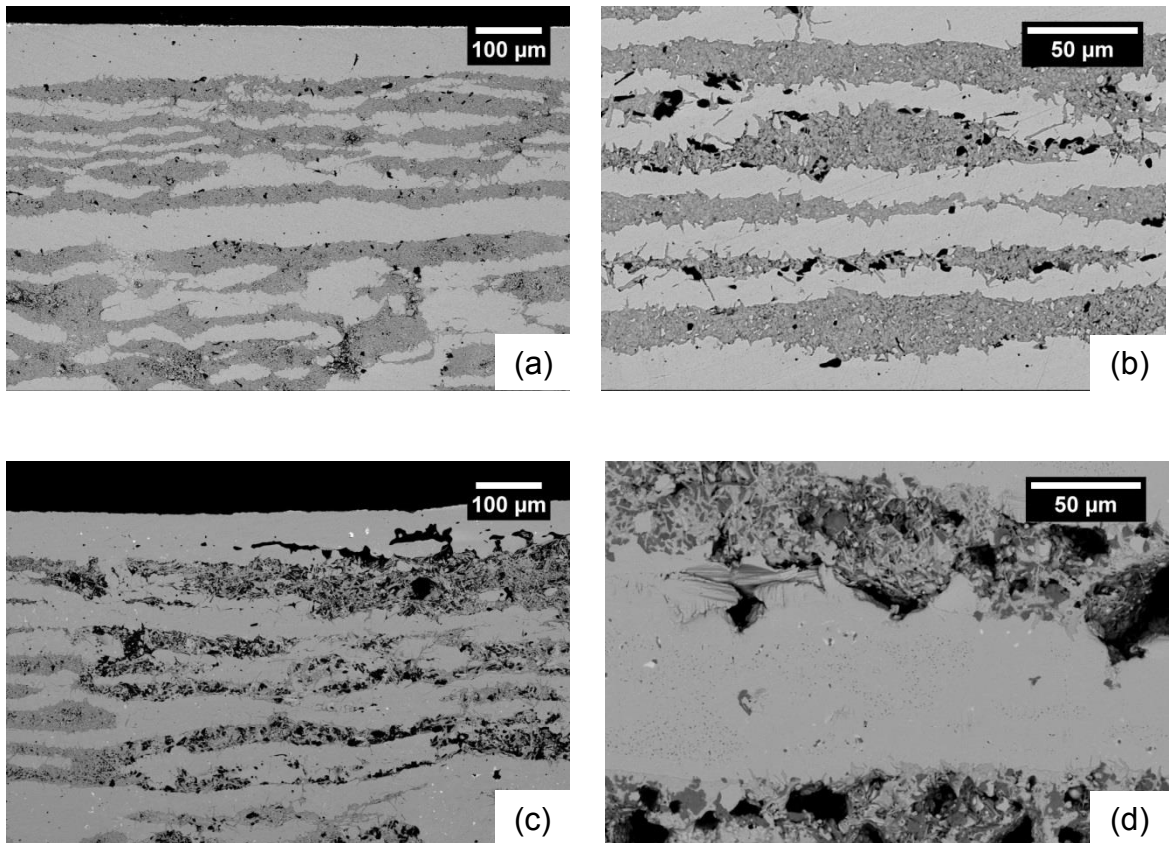


Figure 4-11 SEM images of a longitudinally polished round wire after oxidation and conversion heat treatment (a,b) near the left end, (c,d) in the middle section.

Figures 4-12 and 4-13 show SEM images of a wire after PMP. In Figure 4-12(a), near the end of the wire, dense, connected and textured Bi2212 filaments are observed, whereas in Figure 4-12(b), from the middle of the wire, large pores are observed. Thus, the porosity formed during oxidation, which remains after the conversion stage, remains and increases after PMP. It is thus crucial to control the microstructure during initial oxidation. Cross-sectional images of the wire after PMP near the end of the wire show highly dense and textured Bi2212 grains within a single filament. Instead of the circular distribution of Bi2212 grains found within a filament from an OPIT wire, here, the Bi2212 grains are uniaxially c-axis textured within each filament. The texture is not interrupted by the presence of small dark AEC phases.

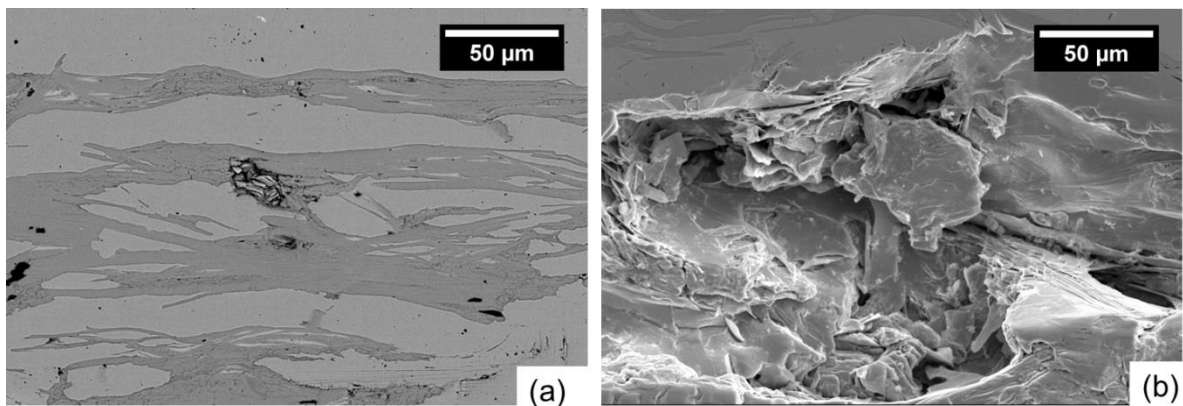


Figure 4-12 SEM images of a longitudinally polished round wire after PMP (a) near the wire end and (b) in the middle section of the wire.

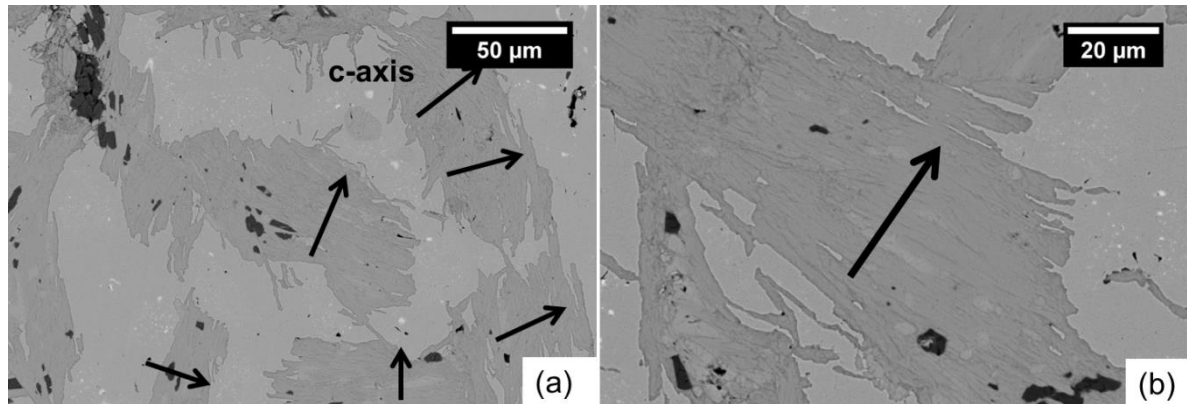


Figure 4-13 SEM images of filament microstructures near the end of the round wire after PMP.

Table 1 summarizes  $J_c$  of 50 mm long round wires and rolled tapes after PMP. Both overall and effective fill factors are used for  $J_c$  calculations.  $J_c$  measured 10 mm from the round wire end is 2-4 times higher than in the middle section of each wire, indicating significant inhomogeneity in performance. For rolled tapes, the difference in  $J_c$  along the sample length is within 3%, indicating a more homogeneous and instantaneous oxidation of MP powders in the tapes than in the round wires.

Table 4-1  $J_c$  (4.2 K, self-field) of MPIT round wires and rolled tapes.

Sample	$J_c^*$ (A/mm <sup>2</sup> ) middle section	$J_c^*$ (A/mm <sup>2</sup> ) wire end	$J_c^{**}$ (A/mm <sup>2</sup> ) middle section	$J_c^{**}$ (A/mm <sup>2</sup> ) wire end
Round wire-1	204	381	1177	2198
Round wire-2	104	365	600	2110
Round wire-3	104	415	600	2398
Rolled tape-1	297	308	1710	1778
Rolled tape-2	366	372	2113	2147

\* $J_c$  values calculated using an overall fill factor of 30%;

\*\* $J_c$  values calculate using effective fill factor of 5%, considering only in-tact filaments after wire deformation

## Discussion

### Green wire fabrication

Both cross-sectional and longitudinal images of green round wire show severe sausaging during wire deformation. The filament size varies along the wire length with a random distribution lacking periodicity. Some of the filaments smears and break, resulting in discontinued filaments which remain after heat treatment and are incapable of carrying long-range transport current macroscopically [39]. In particular, filaments in the central bundle undergo significantly more damage than in the outer bundles. On average, 3-5 filaments merge into a large filament, resulting in only 15-17 filaments in the central bundle instead of the original 55 filaments. The Ag sheath between the filaments also deforms severely and

penetrates the filaments. As a result, few filaments in the central bundle have a continuous length over 500  $\mu\text{m}$  and the filament size exceeds 70  $\mu\text{m}$ . Hence, the inhomogeneity in microstructure, enlarged filament size and filament breakage in the green wire significantly reduce wire performance after heat treatment.

The strain non-uniformity of the metallic precursor core and Ag sheath due to different deformation resistance is responsible for sausaging [39]. One of the causes of severe sausaging is the presence of brittle Bi particles and intermetallic Ca-Cu formed during milling, reducing the MP ductility [37, 40, 41]. Another cause may be the deformation parameters. Since the generation of sausaging in the multifilamentary wires is sensitive to the drawing conditions, additional efforts to address this issue include low-temperature annealing, a small approach angle and reduced reduction per pass during wire drawing [42]. One recent study on OPIT Bi2212 multifilamentary wires using groove-rolling showed large  $J_c$  improvements [43]; groove-rolling does not present the risk of filament sausaging and results in higher powder compaction in the green wire.

#### Oxidation stage

Thermodynamic data [44, 45] between 298.15 K to 1000 K indicates that the oxidation reactions to form  $\text{Bi}_2\text{O}_3$ , CaO, CuO, SrO and  $\text{Cu}_2\text{O}$  are favored in a sequence of  $\text{CaO} > \text{SrO} > \text{Bi}_2\text{O}_3 > \text{Cu}_2\text{O} > \text{CuO}$ . Hence, the oxidation of Ca and Sr is strongly favored as well as displacement reactions between Ca/Sr and  $\text{Bi}_2\text{O}_3$  [37]. Thus, Bi and Cu remain metallic until the surrounding Sr and Ca powders are oxidized. Subsequently, the Bi is oxidized and lastly, Cu is oxidized at the end of the oxidation stage and during heating to the conversion temperature. Because of the low melting temperature of Bi and a eutectic reaction with Ag [46], oxidation of Bi needs to be fast to suppress its melting, formation of a eutectic liquid

and migration toward incoming oxygen through Ag grain boundaries, which depends largely on oxygen availability to MP powders and the oxidation kinetics of Ca and Sr. In [37], Bi<sub>2</sub>O<sub>3</sub> was used instead of Bi, however, this approach did not solve the problem of slow Bi oxidation because Bi<sub>2</sub>O<sub>3</sub> was reduced to Bi by reactions with Sr and Ca.

Considering a long MPIT Ag-sheathed round wire, three oxidation pathways are expected. The first pathway is direct reaction between MP powders and gaseous oxygen in the atmosphere. At the ends of wire, oxygen diffuses through the wire open ends and oxidizes MP powders quickly. CaO and SrO form initially and then facilitate faster oxygen diffusion through their porous structures and along grain and phase boundaries [34]. Metallic Bi then oxidizes quickly into Bi<sub>2</sub>O<sub>3</sub>, limiting its melting and eutectic reaction with Ag. Furthermore, Bi<sub>2</sub>O<sub>3</sub>, together with the Ag sheath and Ag particles in MP powders, allows increased oxygen permeability due to the formation of a mixture of an oxide ion conductor (Bi<sub>2</sub>O<sub>3</sub>) and an electronic phase (Ag). A mixture of Bi<sub>2</sub>O<sub>3</sub> and Ag is reported to increase oxygen permeability by at least one order-of-magnitude compared to pure ceramic [47-49].

The second pathway is the reaction between MP powders and atomic oxygen permeated through the Ag sheathes. This pathway applies to the wire section where gaseous oxygen from the atmosphere is not available but a Bi-rich liquid has not formed. The position in round wire where a Bi-rich liquid starts to migrate out of the filament is at 4.4 mm from the wire end. Thus, between the wire end and 4.4 mm from the end, the oxidation rate is limited by oxygen diffusion kinetics. In the temperature range of 300 °C-500 °C during the oxidation stage, several steps are essential to the passage of oxygen through a Ag sheath: absorption of O<sub>2</sub> on the Ag surface, dissociation, into atomic oxygen, dissolution and bulk diffusion [50-54]. The oxygen flux passing through a Ag membrane can be described as:  $J = DS \frac{\sqrt{P_{hp}} - \sqrt{P_{lp}}}{d}$ ,

where  $J$  is the oxygen flux,  $D$  is the diffusion coefficient,  $S$  is the solubility of the oxygen atoms in the Ag,  $p_{hp}$  and  $p_{lp}$  are oxygen pressures on the high and low pressure sides, respectively, and  $d$  is the Ag thickness. Both  $D$  and  $S$  are temperature-dependent; both increase with temperature, increasing the oxygen flux permeating through the Ag. An increase in the Ag thickness decreases the oxygen flux. In our case, longitudinally, beyond 4.4 mm from the wire end, either the time for oxygen flux to reach the filaments increases, or the oxygen is consumed during passage by filaments before 4.4 mm. Thus, the MP oxidation rate in this wire section is suppressed compared to open wire ends and beyond this point, the third pathway is required.

The third pathway is the reaction between MP powders and the oxygen that permeated through the Ag sheath and Bi-rich liquid. Beyond 4.4 mm from the wire end, the oxygen flux that permeates through the outer and interfilamentary Ag sheathes is insufficient to oxidize Bi after first oxidizing the Sr and Ca. Due to an affinity to oxygen, metallic, liquid Bi diffuses towards the incoming oxygen and concentrates at the Ag/filament interface. Based on calculations at 300 °C, the solubility of oxygen in Ag is on the order of  $10^{-3}$  at% while that in the Bi-rich liquid is only about  $10^{-5}$  at%. With increasing temperature, the solubility of oxygen in Ag rapidly increases to about 1.86 at% at 750 °C, but the solubility of oxygen in the Bi-rich liquid only increases to 0.33 at%. Thus, the Bi-rich liquid layer at the Ag/filament interface acts as a barrier to oxygen diffusion into the filaments, further slowing and suppressing oxidation compared to the wire ends. Furthermore, as the Bi-rich liquid infiltrates the Ag grain boundaries and migrates to the incoming oxygen, it concentrates at the wire/atmosphere free surface. Since oxygen diffusion through Ag at temperatures between 300 °C -500 °C is mainly through grain boundary diffusion rather than lattice

diffusion [55, 56], a high concentration of Bi-rich liquid in Ag grain boundaries greatly decreases oxygen diffusion from the atmosphere towards the internal filaments. Hence, in the middle section of the round wire, since the only possible way to obtain oxygen is through permeation through the outer Ag-sheath, the Bi-rich liquid barrier limits the oxygen reaching the filament. This results in severe wire deformation, porosity and Bi loss, which remains in the subsequent conversion and PMP heat treatments.

At elevated temperature, the rate of oxygen permeating through Ag increases, as does the migration rate of the Bi-rich liquid due to an increased diffusion rate and decreased viscosity [57, 58]. Initial attempts to oxidize MPIT wire at temperatures above 500 °C were not successful due to increased Bi melting, migration and wire breakage. Hence, other methods to increase the oxygen availability to MP powders, including increasing the oxygen pressure, e.g. OP processing in the low temperature range during the oxidation stage, reducing the filament size and reducing the Ag sheath thickness, are needed. In this study, the latter two methods are employed by rolling the round wires into tapes, decreasing the outer and interfilamentary Ag sheath thicknesses as well as the filament size. A previous study on Bi2223 MPIT tapes indicated that if the filament size is reduced to about 5 µm, wire length and mass no longer impact the oxidation kinetics [34]. For the rolled tapes studied here, the top and bottom Ag thickness is reduced to 17-20 µm, and the filament size is reduced to 8-26 µm, which are half or one-third of the values for round wires. During oxidation at 300 °C, smaller filaments oxidize faster. Although a Bi-rich liquid still forms and migrates through Ag grain boundaries, it is oxidized into Bi<sub>2</sub>O<sub>3</sub> and its migration stops before reaching the wire/atmosphere free surface. The overall oxidation along the total 50 mm length of tape is

homogeneous and without severe deformation. This serves as a prerequisite for homogeneous phase transformation into Bi2212 and enhanced texture in the subsequent stages.

#### Conversion and PMP stages

Bi-loss, porosity and wire damage that are seen in the green wire and after the oxidation stage remain or become more severe after the conversion and PMP stages. Sub-oxides depleted with Bi react and convert to  $(Ca,Sr)O_x$  and AEC phases, pores agglomerate during the partial-melt and the cracked Ag sheath becomes softer and deforms further at elevated temperatures.

In the filaments in the outer bundles and in the section that is closest to the wire ends, however, dense and homogeneous sub-oxides are obtained. The sub-oxides are of similar size as the metallic powders, and thus the homogeneity of the elemental distribution is similar to the green wire. Discussions of sub-oxides  $\rightarrow$  Bi2212 in the conversion stage and PMP stage are focused on the wire sections where the oxidation is thorough and all cations are present.

During the conversion heat treatment, the transformation of sub-oxides into Bi2212 grains is not affected by increasing the holding time at 830 °C to a maximum of 96 hrs. Bi2212 grains, about 3-5  $\mu\text{m}$  in size, are densely packed in the filament with interspersed Ag particles. Highly dense filaments containing micrometer-size Bi2212 grains are obtained after the conversion stage but before PMP, which is significantly different from the 70%-80% dense OPIT green wire, indicating that starting with metallic precursors, over 95% dense Bi2212 filaments can be obtained.

After PMP, uniaxially c-axis textured Bi2212 grains are observed within individual filaments, as compared to the circular texture found in OPIT Bi2212 after PMP [59]. The basal-plane from a cross-sectional view of the wire nearly extends the entire filament width. Furthermore,

Bi2201 grains are not observable, consistent with the previous study of MP pellets [38]. A recent Bi2212 round wire study showed that filaments containing dense, highly textured Bi2212 grains [60, 61] are essential to high transport  $J_c$ , whereas filaments containing large Bi2201 grains are detrimental to transport  $J_c$ , even if the overall Bi2201 area fraction in those filaments is small. Hence, the microstructures found here, containing dense and highly c-axis textured Bi2212 grains and no large Bi2201 grains, are favorable for transport  $J_c$ .

Several factors contribute to the formation of this type of microstructure. One factor is related to the chemical homogeneity of MP powders. Since 3-5  $\mu\text{m}$  Bi2212 grains with Ag particles were homogeneously distributed in the filament, the melting onset, nucleation and phase assemblage during cooling were homogeneous as well. Previous studies indicated that Ag additions to precursor powders minimizes the melting onset difference between the Ag/filament interface and the filament center [62]. The peritectic liquid formed during partial-melt is homogeneous within the filament. Thus, no large secondary phase particles, such as AEC particles, are observed in the filament after PMP, which is commonly a result of impeded dissolution of secondary phases [63]. In addition, Bi2212 crystals nucleate on arbitrary-shaped, randomly-distributed secondary phase particles and align to their surfaces rather than to the Ag/filament interface. Hence, with only a small quantity of small-sized secondary phase particles, Bi2212 grain alignment with the c-axis perpendicular to the Ag/filament interface is enhanced. Nevertheless, Bi2212 colonies as large as a single filament are not formed only by Ag/filament texturing. Other factors also contribute.

The second factor is related to the density of the Bi2212 filaments after the conversion heat treatment. Aksenova et al. suggested that preferential alignment of Bi2212 grains in the filament is a consequence of geometric constraints by the Ag sheath and the large growth

anisotropy between the a-b plane and c-plane [64]. Buhl indicated that Bi2212 grains bend during growth when they reach a Ag surface and turn parallel to the Ag surface [65]. Since Bi2212 grains growing in the peritectic liquid are mobile [66], if 20-30% porosity is present in the filament, the geometric constraint of the Ag sheath only affects the Bi2212 grains in the vicinity of the Ag/filament interface, and the Bi2212 grains in filament center remain randomly oriented. With porosity, there is little opportunity for floating Bi2212 grains grown at the early stage to contact the Ag sheath and subsequently bend. Besides, although a Bi2212 grain with its c-axis parallel to the interface will be restrained from growing and is likely to be consumed by the grains with c-axes perpendicular to the Ag/filament interface [66], the presence of porosity is an obstacle for mass transport between crystals, hindering alignment. If the wire density increases to > 95 - 98%, however, the space for Bi2212 grains to float and rotate freely decreases, as does the mass transport distance. Bi2212 grains are then sufficiently close to each other within the filament and the contact between two grains are more energetically favored if the c-axes of both grains are parallel [66], resulting in a stacked growth of Bi2212 grains with c-axes perpendicular to the Ag/filament interface.

The third factor considers the wetting effect at the Ag particles/Bi2212 grains interfaces, which also contributes to c-axis alignment in a Bi2212 colony. Studies on tapes showed that Bi2212 grain alignment at the Ag/Bi2212 interface is much better than at the Bi2212 free surface [67]. By increasing the Ag/Bi2212 interfacial surface area, more nucleation sites become available, resulting in a high degree of alignment [66, 68]. Simply adding Ag to the precursor powders, however, did not influence the texture in the filament or the transport properties of OPIT wires [62]. This was previously explained as being too low a dopant level (2.9 - 5.8 wt%), but it may be the result of the low-density of green OPIT wires such that the

Ag particles are not in close contact with the Bi2212 grains. In MPIT wires after the conversion heat treatment, Ag particles are in close contact with Bi2212 grains. Since 2 wt% Ag addition in Bi2212 reduces the melting point by 20 °C in pure oxygen [69], a thin liquid layer between Bi2212 grains and Ag particles during solidification is expected. This thin liquid layer enhances mass transport between the two adjacent the Bi2212 grains, which either facilitates parallel c-axis orientation between the two grains to be c-axis parallel or the consumption of a misoriented grain. Therefore, large and high textured Bi2212 colonies within one filament are formed under the presence of Ag particles in the MP powder and the high filament density after oxidation and conversion heat treatment.

#### Influence of wire deformation on transport performance

Although highly dense and textured Bi2212 filaments are formed, the overall  $J_c$  ( $J_c^*$ ) are significantly lower than those of OPIT wires. This is primarily a result of the wire deformation and the macroscopic inhomogeneities in the resulting green wire.

One of the factors is the macroscopic wire structure homogeneity. Three round wire samples were heat treated under the same conditions, as were the two rolled tapes. The transport performance, however, depends strongly on the local microstructure before heat treatment. Due to sausaging and the damage to the filaments introduced during wire deformation, filament connectivities and microstructures vary significantly from section to section.

Additional damage occurred during rolling, resulting in further filament breakage in rolled tapes. Although faster and more homogeneous oxidation improves the homogeneity of transport in rolled tapes reference to round wires, the absolute  $J_E$  values are lower. During the rolling process, some regions that showed some necking and were capable of carrying some

transport current are damaged further, resulting in a disconnected filament and losing the ability to carry current.

In the aggregate, all of the deformation-related damage reduces the effective filament cross-sectional area that is capable of carrying transport current. Considering the significant necking, and the damaged central bundle, the remaining effective fill factor is only 5%, and the resulting  $J_c$  is comparable to OPIT round wires. This confirms that the macroscopic filament damage during deformation is the most significant current-limiting factor in this study and that MPIT wires require an alternative wire deformation approach, such as hot extrusion or groove-rolling.

## **Conclusions**

A study of Bi2212/Ag round multifilamentary wire manufactured via the metallic-powder-in-tube (MPIT) process and heat treated in 1 atm oxygen is presented. The metallic precursor powders are packed into a pure Ag tube in an Ar atmosphere and sealed. After deformation, the multifilamentary round wires and rolled tapes are heat treated in flowing oxygen through three stages: oxidation, conversion and partial-melt processing. Processing-microstructure-property relationships on 20 - 50 mm long multifilamentary round wires and rolled tapes are studied extensively. It is found that the first heat treatment stage, the oxidation stage, plays a crucial role in chemical homogeneity, phase transformation, microstructure evolution and conductor performance. Three MP oxidation pathways are discussed in Ag-sheathed MPIT wires. Furthermore, it is found that the Bi2212 grain alignment within an MPIT filament is different from that found in OPIT filaments after PMP. The influence of chemical homogeneity, Ag addition in MP powder and the dense microstructure from oxidation and conversion stages on the formation of highly textured and large Bi2212 colonies are

discussed. Future work may include enhancement in MP powder ductility, fabrication of multifilamentary wires with smaller Ag sheath thickness and filament size and over-pressure oxidation.

### **Acknowledgement**

The authors are grateful to Terrence Wong and William Nachtrab (Supercon, Inc.) for making multifilamentary wires and rolled tapes for this study. The authors also acknowledge the use of the Analytical Instrumentation Facility (AIF) at North Carolina State University, which is supported by the State of North Carolina and the National Science Foundation. The authors thank Jenna Pilato and Kyle Malone for assistance with this study. The authors are also grateful to Golsa Naderi, Wan Kan Chan and Federico Scurti for helpful discussion.

## REFERENCES

- [1] D. C. Larbalestier, *et al.*, "Isotropic round-wire multifilament cuprate superconductor for generation of magnetic fields above 30 T," *Nature Materials*, vol. 13, pp. 375-381, 2014.
- [2] A. Devred, *et al.*, "Future accelerator magnet needs," *IEEE Transactions on Applied Superconductivity*, vol. 15, pp. 1192-1199, Jun 2005.
- [3] L. Rossi, "Superconductivity: its role, its success and its setbacks in the Large Hadron Collider of CERN," *Superconductor Science & Technology*, vol. 23, Mar 2010.
- [4] S. A. Gourlay, *et al.*, "Magnet R&D for the US LHC Accelerator Research Program (LARP)," *IEEE Transactions on Applied Superconductivity*, vol. 16, pp. 324-327, Jun 2006.
- [5] A. S. Alexandrov, *et al.*, "Resistive Upper Critical Field of High-  $T_c$  Single Crystals of Bi2212," *Physical Review Letters*, vol. 76, pp. 983-986, 1996.
- [6] Y. Wang, *et al.*, "Dependence of Upper Critical Field and Pairing Strength on Doping in Cuprates," *Science*, vol. 299, pp. 86-89, January 3, 2003 2003.
- [7] Y. Ando and K. Segawa, "Magnetoresistance of Untwinned YBCO Single Crystals in a Wide Range of Doping: Anomalous Hole-Doping Dependence of the Coherence Length," *Physical Review Letters*, vol. 88, p. 167005, 2002.
- [8] J. Schwartz, *et al.*, "High Field Superconducting Solenoids Via High Temperature Superconductors," *IEEE Transactions on Applied Superconductivity*, vol. 18, pp. 70-81, 2008.
- [9] W. T. Nachtrab, *et al.*, "Effect of Solidification Conditions on Partial Melt Processed Bi2212/Ag Round Wire," *IEEE Transactions on Applied Superconductivity*, vol. 21, pp. 2795-2799, Jun 2011.
- [10] T. Hatano, *et al.*, "High-temperature X-ray study of melting and solidification of the  $\text{Bi}_2\text{Sr}_2\text{CaCu}_2\text{O}_{8+\delta}$  on silver," *Journal of Low Temperature Physics*, vol. 117, pp. 777-781, 1999.
- [11] A. Polasek, *et al.*, "Partial melt processing of high- $T_c$  bulk Bi-2212 starting from different precursor powders," in *8th European Conference on Applied Superconductivity*. vol. 97, S. Hoste and M. Ausloos, Eds., ed Bristol: Iop Publishing Ltd, 2008.
- [12] D. Sager, *et al.*, "Novel precursor reaction pathways to Bi-2212 bulk superconductors," *Physica C: Superconductivity*, vol. 417, pp. 85-97, 2005.

- [13] V. Garnier, *et al.*, "Relationship among synthesis, microstructure and properties in sinter-forged Bi-2212 ceramics," *Physica C: Superconductivity*, vol. 319, pp. 197-208, 1999.
- [14] P. Majewski, *et al.*, " Relationships between the chemical composition and properties of the high-temperature superconductor  $\text{Bi}_{2+x}\text{Sr}_{2-y}\text{Ca}_{1+y}\text{Cu}_2\text{O}_{8+d}$ ," *Journal of Materials Science*, vol. 32, pp. 5137-5141, 1997.
- [15] J. Fransaer, *et al.*, "Sol-gel preparation of high- $T_c$  Bi-Ca-Sr-Cu-O and Y-Ba-Ca-O superconductors," *Journal of Applied Physics*, vol. 65, pp. 3277-3279, 1989.
- [16] R. S. Feigelson, *et al.*, "Superconducting Bi-Ca-Sr-Cu-O fibers grown by the laser-heated pedestal growth method," *Science*, vol. 240, pp. 1642-1645, June 17, 1988 1988.
- [17] D. Sager, *et al.*, "Influence of precursor calcination parameters on the critical current density of Bi-2212 superconductors," *Physica C: Superconductivity*, vol. 434, pp. 125-134, 2006.
- [18] H. Miao, *et al.*, "Optimization of melt-processing temperature and period to improve critical current density of  $\text{Bi}_2\text{Sr}_2\text{CaCu}_2\text{O}_x/\text{Ag}$  multilayer tapes," *Physica C*, vol. 320, pp. 77-86, Jul 1999.
- [19] Y. Zhang, *et al.*, " $\text{Bi}_2\text{Sr}_2\text{CaCu}_2\text{O}_x$  oxide precursor synthesis from nano-oxides and its effects on multifilamentary wire transport properties," *Superconductor Science and Technology* (submitted), 2015.
- [20] E. E. Hellstrom and W. Zhang, "Formation and prevention of bubbles when melt processing Ag-sheathed  $\text{Bi}_2\text{Sr}_2\text{CaCu}_2\text{O}_x$  (2212) conductors," *Superconductor Science and Technology*, vol. 8, p. 317, 1995.
- [21] W. Zhang, *et al.*, "Formation of Porosity and Its Effects on the Uniformity of  $J_c$  in Bi-2212/Ag Tapes," in *Advances in Cryogenic Engineering Materials*. vol. 44, U. B. Balachandran, *et al.*, Eds., ed: Springer US, 1998, pp. 509-516.
- [22] M. O. Rikel, *et al.*, "Competitiveness of porosity and phase purity in melt processed Bi2212/Ag conductors," *Physica C: Superconductivity*, vol. 354, pp. 321-326, 2001.
- [23] J. Jiang, *et al.*, "Doubled critical current density in Bi-2212 round wires by reduction of the residual bubble density," *Superconductor Science and Technology*, vol. 24, p. 082001, 2011.
- [24] C. Scheuerlein, *et al.*, "Void and phase evolution during the processing of Bi-2212 superconducting wires monitored by combined fast synchrotron micro-tomography and x-ray diffraction," *Superconductor Science and Technology*, vol. 24, p. 115004, 2011.

- [25] T. Shen, *et al.*, "Role of internal gases and creep of Ag in controlling the critical current density of Ag-sheathed  $\text{Bi}_2\text{Sr}_2\text{CaCu}_2\text{O}_x$  wires," *Journal of Applied Physics*, vol. 113, pp. -, 2013.
- [26] W. Zhang and E. E. Hellstrom, "The influence of carbon on melt processing Ag sheathed  $\text{Bi}_2\text{Sr}_2\text{CaCu}_2\text{O}_8$  tape," *Physica C: Superconductivity*, vol. 234, pp. 137-145, 1994.
- [27] G. Naderi and J. Schwartz, "Multiscale studies of processing-microstructure-transport relationships in over- pressure processed  $\text{Bi}_2\text{Sr}_2\text{CaCu}_2\text{O}_x/\text{Ag}$  multifilamentary round wire," *Superconductor Science and Technology*, vol. 27, p. 115002, 2014.
- [28] M. Minami, *et al.*, "Research and development of superconducting magnetic energy storage system - Influence of mechanical properties of Bi-2212/Ag Rutherford cable to its critical current," *Physica C*, vol. 357, pp. 1323-1326, Aug 2001.
- [29] M. T. Malachevsky and C. A. D'Ovidio, "SEM investigation of the critical current degradation onset in BSCCO-2223 multifilamentary tapes submitted to bending," *Superconductor Science and Technology*, vol. 18, pp. 289-293, Mar 2005.
- [30] Q. V. Le, *et al.*, "Two-dimensional peridynamic simulation of the effect of defects on the mechanical behavior of  $\text{Bi}_2\text{Sr}_2\text{CaCu}_2\text{O}_x$  round wires," *Superconductor Science and Technology*, vol. 27, p. 115007, 2014.
- [31] A. L. Mbaruku and J. Schwartz, "Statistical analysis of the electromechanical behavior of AgMg sheathed  $\text{Bi}_2\text{Sr}_2\text{CaCu}_2\text{O}_{8+x}$  superconducting tapes using Weibull distributions," *Journal of Applied Physics*, vol. 101, p. 073913, Apr 2007.
- [32] X. F. Gou and J. Schwartz, "Fractal analysis of the role of the rough interface between  $\text{Bi}_2\text{Sr}_2\text{CaCu}_2\text{O}_x$  filaments and the Ag matrix in the mechanical behavior of composite round wires " *Journal of Applied Physics*, vol. 26, 2012.
- [33] A. Godeke, *et al.*, "Critical current of dense Bi-2212 round wires as a function of axial strain," *Superconductor Science and Technology*, vol. 28, p. 032001, 2015.
- [34] A. Otto, *et al.*, "Properties of high- $T_c$  wires made by the metallic precursor process," *Journal of the Minerals Metals & Materials Society*, vol. 45, pp. 48-52, Sep 1993.
- [35] A. Otto, *et al.*, "Multifilamentary Bi-2223 composite tapes made by a metallic precursor route," *IEEE Transactions on Applied Superconductivity*, Vol 3, No 1, March 1993 Pts 2-4, pp. 915-922, 1993.
- [36] A. Otto, *et al.*, "Progress towards a long length metallic precursor process for multifilament Bi-2223 composite superconductors," *IEEE Transactions on Applied Superconductivity*, vol. 5, pp. 1154-1157, Jun 1995.

- [37] T. J. Detrie and K. H. Sandhage, "Fabrication of  $\text{Ag/Bi}_2\text{Sr}_2\text{CaCu}_2\text{O}_{8-x}$  superconducting tapes by the oxidation and postoxidation (partial melt) annealing of malleable, metal-bearing precursors," *Journal of Materials Research*, vol. 15, pp. 306-316, 2000.
- [38] Y. Zhang, *et al.*, "Synthesis of  $\text{Bi}_2\text{Sr}_2\text{CaCu}_2\text{O}_x$  superconductors via direct oxidation of metallic precursors," *Superconductor Science and Technology*, vol. 27, p. 055016, 2014.
- [39] W. G. Wang, *et al.*, "The effect of mechanical deformation on silver - core interface and critical current density in Ag - Bi-2223 single- and multifilament tapes," *Superconductor Science and Technology*, vol. 9, p. 875, 1996.
- [40] D. J. Chakrabarti and D. E. Laughlin, "The Ca-Cu (Calcium-Copper) system," *Bulletin of Alloy Phase Diagrams*, vol. 5, pp. 570-576, 1984/12/01 1984.
- [41] V. A. Skudnov, *et al.*, "Mechanical properties of bismuth at different temperature and strain rates," *Metal Science and Heat Treatment*, vol. 11, pp. 981-984, 1969/12/01 1969.
- [42] H. Hong-Soo, *et al.*, "The effects of drawing parameters on sausaging and critical current density of Bi-2223/Ag HTS wires," *IEEE Transactions on Applied Superconductivity*, vol. 11, pp. 3748-3751, 2001.
- [43] A. Malagoli, *et al.*, "Large critical current density improvement in Bi-2212 wires through the groove-rolling process," *Superconductor Science and Technology*, vol. 26, p. 045004, 2013.
- [44] J. Malcolm.W. Chase, "NIST-JANAF Thermochemical tables, 4th edition," *Journal of Physical and Chemical Reference Data*, vol. Monograph 9, 1998.
- [45] I. Barin and F. Sauert, *Thermochemical Data of Pure Substance: VCH Verlagsgesellschaft*, 1993.
- [46] R. Elliott and F. Shunk, "The Ag-Bi (Silver-Bismuth) system," *Bulletin of Alloy Phase Diagrams*, vol. 1, pp. 62-64, 1980/09/01 1980.
- [47] K. Wu, *et al.*, "Oxygen permeation through  $(\text{Bi}_2\text{O}_3)_{0.74}(\text{SrO})_{0.26}$ -Ag (40% v/o) composite," *Journal of Membrane Science*, vol. 188, pp. 189-193, 2001.
- [48] E. Capoen, *et al.*, "Oxygen permeation in bismuth-based materials. Part II: Characterisation of oxygen transfer in bismuth erbium oxide and bismuth calcium oxide ceramic," *Solid State Ionics*, vol. 177, pp. 489-492, 2006.
- [49] E. Capoen, *et al.*, "Oxygen permeation in bismuth-based materials. Part I: Sintering and oxygen permeation fluxes," *Solid State Ionics*, vol. 177, pp. 483-488, 2006.

- [50] F. M. G. Johnson and P. Larose, "The diffusion of oxygen through silver," *Journal of the American Chemical Society*, vol. 46, pp. 1377-1389, 1924/06/01 1924.
- [51] V. I. Bukhtiyarov, *et al.*, "Oxygen adsorption on Ag(111): X-ray photoelectron spectroscopy (XPS), angular dependent x-ray photoelectron spectroscopy (ADXPS) and temperature-programmed desorption (TPD) studies," *The Journal of Chemical Physics*, vol. 111, pp. 2169-2175, 1999.
- [52] C. Backx, *et al.*, "Adsorption of oxygen on Ag(110) studied by high resolution ELS and TPD," *Surface Science*, vol. 104, pp. 300-317, 1981.
- [53] C. T. Campbell, "Atomic and molecular oxygen adsorption on Ag(111)," *Surface Science*, vol. 157, pp. 43-60, 1985.
- [54] G. y. S. Gryaznov VM, Kanizius S., "Diffusion of oxygen through a silver membrane," *Russian Journal of Physical Chemistry*, vol. 47, pp. 1517-1518, 1973.
- [55] R. E. Hoffman and D. Turnbull, "Lattice and Grain Boundary Self-Diffusion in Silver," *Journal of Applied Physics*, vol. 22, pp. 634-639, 1951.
- [56] R. A. Outlaw, *et al.*, "Oxygen transport through high-purity, large-grain Ag," *Journal of Materials Research*, vol. 3, pp. 1378-1384, 1988.
- [57] A. T. Aldred and J. N. Pratt, "Vapor Pressure of Liquid Bismuth," *The Journal of Chemical Physics*, vol. 38, pp. 1085-1087, 1963.
- [58] S. S. Mitra, "Relation between Vapor Pressure and Viscosity of Liquids," *The Journal of Chemical Physics*, vol. 22, pp. 349-350, 1954.
- [59] D. Bourgault, *et al.*, "Misalignment angles and the 2D–3D temperature crossover in Bi2212 multifilaments studied using transport critical current densities," *Superconductor Science and Technology*, vol. 17, p. 463, 2004.
- [60] G. Naderi, *et al.*, "Understanding processing–microstructure–properties relationships in Bi<sub>2</sub>Sr<sub>2</sub>CaCu<sub>2</sub>O<sub>x</sub>/Ag round wires and enhanced transport through saw-tooth processing," *Superconductor Science and Technology*, vol. 26, p. 105010, 2013.
- [61] B. Evan Callaway, *et al.*, "Statistical analysis of the relationship between electrical transport and filament microstructure in multifilamentary Bi<sub>2</sub>Sr<sub>2</sub>CaCu<sub>2</sub>O<sub>x</sub>/Ag/Ag–Mg round wires," *Superconductor Science and Technology*, vol. 27, p. 044020, 2014.
- [62] H. Miao, *et al.*, "Studies of Precursor Composition Effect on J<sub>c</sub> in Bi-2212/Ag Wires and Tapes," *AIP Conference Proceedings*, vol. 824, pp. 673-682, 2006.

- [63] D. Buhl, *et al.*, "Phase composition and grain alignment in partial melt processed Bi-2212 thick films," *IEEE transactions on Applied Superconductivity*, vol. 4, pp. 299-317, 1996.
- [64] T. D. Aksenova, *et al.*, "Texture Formation in Bi<sub>2</sub>Sr<sub>2</sub>Ca<sub>1</sub>Cu<sub>2</sub>O<sub>x</sub>/Ag Tapes Prepared By Thick Films," *Physica C*, vol. 205, pp. 271-279, Feb 1993.
- [65] D. Buhl, *et al.*, "Texture in Melt-Processed Bi-2212," *Journal of Electroceramics*, vol. 1, pp. 133-144, 1997/09/01 1997.
- [66] E. Cecchetti, *et al.*, "A model for texture development in BSCCO high- T<sub>c</sub> superconductors," *Superconductor Science and Technology*, vol. 13, p. 1270, 2000.
- [67] H. Kumakura, *et al.*, "Influence of Ag substrates on grain alignment and critical current density of Bi-2212 tape conductors," *IEEE Transactions on Applied Superconductivity*, vol. 9, pp. 1804-1807, 1999.
- [68] T. G. Holesinger, *et al.*, "Compositional and microstructural analysis of high I<sub>c</sub> and J<sub>c</sub> Bi-2212 conductors," *IEEE Transactions on Applied Superconductivity*, vol. 15, pp. 2562-2565, 2005.
- [69] T. Lang, *et al.*, "Melting of Bi-2212 under controlled oxygen partial pressures with silver," *Physica C: Superconductivity*, vol. 275, pp. 284-292, 1997.

## Chapter 5

### CONCLUSIONS AND SUGGESTED FUTURE WORK

This thesis investigates the process-microstructure-properties relationships between precursor powder and  $\text{Bi}_2\text{Sr}_2\text{CaCu}_2\text{O}_x$  (Bi2212) /Ag wire performance.

In Chapter 1, a new method combining NanoSpray Combustion<sup>TM</sup> processing and solid-state calcination is used to synthesize Bi2212 oxide precursor. In Chapter 2, an alternative approach with the potential to address the issues with oxide-powder-in-tube method, metallic-precursor-in-tube method (MPIT), is introduced and studied. The formation of metallic precursor powders via mechanical alloying is discussed. Several factors that impact the direct oxidation on metallic powders including formation and growth of Bi2212 grains are discussed. In Chapter 3, Bi2212/Ag multifilamentary round wires and rolled tapes are fabricated via MPIT method. Processing-microstructure-property relationships on wires and tapes that went through oxidation, conversion and partial-melt processing (PMP) stages are studied. The advantages over oxide-powder-in-tube method and current-limiting factors are discussed.

The main conclusions of this thesis are summarized as follows:

- By using nanosize oxides as starting materials, precursor powders with precisely controlled stoichiometry and chemical homogeneity containing over 99.1 vol% of Bi2212 single crystals are synthesized. Alkaline-earth cuprate (AEC) are found to be the only impurity phase in the precursor powders.
- Small particle size, high surface area and short diffusion length of the starting materials result in a rapid and homogeneous phase transformation to Bi2212, along

with an early and rapid carbon release. The residual carbon is between 50-90 ppm after calcination.

- The strong dependence of transport critical current densities on precursor stoichiometry indicates that compositional variations within precursor powders should be less than 1.51 mol%. Two Bi-rich and Ca-deficient stoichiometries give higher wire transport critical current density, with the highest being 2520 A/mm<sup>2</sup> (4.2 K, 5 T) with an optimal PMP peak temperature of 889 °C.
- AEC particles smaller than the wire filament size are not considered to be a negative factor on wire performance, but as potential additional nucleation sites during solidification. The absence of Bi2201 grains in the precursor powders is preferred.
- Through mechanical alloying, metallic precursor powder can have a controllable stoichiometry and homogeneous elemental distribution. With sufficient intermittent scraping and optimized milling time, an elementally homogeneous metallic precursor powder with the desired stoichiometry can be obtained, avoiding phase segregation and inhomogeneous oxidation after heat treatment.
- By using a direct oxidation approach to forming Bi2212 grains without a partial melt, Bi2201 is the only phase impurity formed, and the Bi2201 content is much lower than in tapes and wires.
- High density Bi2212 colonies are formed during the metallic precursor → Bi2212 transformation and that large, textured grains are aligned at the Ag interface. The microstructure at the metallic pellet/silver interface suggests larger size and preferred orientation of Bi2212 grains with the aid of a silver surface.

- Heat treatments on the multifilamentary round wires and rolled tapes via metallic-precursor-in-tube method including three stages: oxidation, conversion and PMP.
- It is found that the first heat treatment stage, oxidation stage, plays a crucial role in chemical homogeneity, phase transformation, microstructure evolution and conductor performance. Three pathways of metallic precursor oxidation are identified and studied in Ag-sheathed wires.
- It is found that the Bi2212 grain alignment within one filament from MPIT is different from OPIT after melt-processing, indicating the formation of highly dense filament containing Bi2212 fine grains and Ag particles before PMP stage helps formation of large, c-axis textured Bi2212 filament during PMP stage.

Suggested future work:

- To increase the melting uniformity for Bi2212/Ag wire during PMP, adding nanosize or micron size Ag particles to oxide precursor powders is suggested.
- Since nanosize defects are potential pinning sites in Bi2212/Ag conductors, adding dopants as MgO, ZrO<sub>2</sub> or Al<sub>2</sub>O<sub>3</sub> is suggested to enhance the transport at high field.
- Since brittle components in metallic precursor causes severe “sausaging” phenomenon during wire drawing. a method combining low-energy ball milling and mechanical alloying is suggested to synthesize metallic precursor with increased ductility and malleability.
- Since “sausaging” phenomenon during wire drawing significantly decreases the filament connectivity in MPIT wires, a study on optimizing drawing conditions is

suggested, which may include low-temperature annealing, small approach angle, small reduction per pass or using groove-rolling.

- To increase oxidation kinetics during MPIT wire oxidation, making wires with filaments and Ag sheath thickness  $\sim 5 - 10 \mu\text{m}$  is suggested. Also, oxidation in over 1 atm pure  $\text{O}_2$  is suggested.
- Local transport properties measurements on different sections of wire filaments to investigate the current flow mechanism from a microscopic perspective.